Photoemission microscopy and spectroscopy of cobalt-intercalated graphene on silicon carbide

Dissertation

zur Erlangung des
Doktorgrades der Naturwissenschaften
(Dr. rer. nat.)
der Fakultät Physik
der Technischen Universität Dortmund

vorgelegt von
Richard Hönig
geboren in Georgsmarienhütte

– 2019 –

Der Fakultät für Physik der Technischen Universität Dortmund zur Erlangung des akademischen Grades eines Doktors der Naturwissenschaften vorgelegte Dissertation.

Erstgutachter: Prof. Dr. Carsten Westphal
Zweitgutachter: Prof. Dr. Markus Betz
Vorsitzender der Prüfungskommission: Prof. Dr. Shaukat Khan
Vertretung der wiss. Mitarbeiter: Priv.-Doz. Dr. Johannes Erdmann

Datum des Einreichens der Arbeit: 27. August 2019
Datum der mündlichen Prüfung: 21. Oktober 2019

Abstract

Graphene-ferromagnet interfaces possess remarkable properties like induced magnetism in the graphene film, increased magnetic anisotropy in the ferromagnetic film, and chiral magnetism. Previously, the graphene-ferromagnet interface was investigated mainly on metallic substrates. Yet, silicon carbide (SiC) is a promising graphene substrate due to its semi-insulating properties and its industrial relevance. This thesis investigates for the first time the intercalation of thin cobalt films underneath graphene on SiC with emphasis on the structural, chemical, and magnetic properties of the intercalated cobalt films. The 6H-SiC(0001) samples were prepared in an argon atmosphere in order to achieve a homogeneous, large-area growth of the $\left(6\sqrt{3} \times 6\sqrt{3}\right)$-R30° (hereafter $6\sqrt{3}$) surface reconstruction. The $6\sqrt{3}$ structure can be regarded as a graphene layer that is partly covalently bonded to the SiC substrate. It is expected that the $6\sqrt{3}$ structure converts into a graphene film upon intercalation. Cobalt films with thicknesses t_{Co} in a range of 0.4–12 nm were deposited at room temperature, at which no reaction with the $6\sqrt{3}$ reconstructed SiC surface was observed.

During a controlled annealing procedure, the temperature and film thickness dependence of the intercalation process was investigated in real time by ultraviolet photoemission electron microscopy (UV-PEEM). The intercalation temperature strongly depends on the film thickness with a minimum of 340 °C for $t_{\mathrm{Co}} = 1.4\,\mathrm{nm}$. Structural and chemical information are provided by low-energy electron diffraction (LEED) and x-ray photoelectron spectroscopy (XPS), respectively. A partial conversion of the $6\sqrt{3}$ reconstruction into a graphene film is found for low t_{Co}, whereas a full conversion is observed for high t_{Co}. The partial conversion is associated with an agglomeration of the cobalt film, as found by x-ray photoemission electron microscopy (X-PEEM) images with chemical contrast recorded at the Co L_3-edge. Furthermore, using Si 2p XPS spectra and x-ray absorption spectra (XAS) of the Co L-edge extracted from the X-PEEM images, a self-limited cobalt silicide formation that is independent of t_{Co} is found at the Co-SiC interface. The magnetic properties of the cobalt film are investigated by X-PEEM images with magnetic contrast recorded at the Co L_3-edge. A self-assembled nanowire formation at the SiC step edges is observed for low t_{Co}, while for intermediate t_{Co} a step anisotropy dominates the magnetic domain structure, and a bulk-like magnetic domain structure is present for high t_{Co}.

Kurzfassung

Grenzschichten zwischen Graphen und ferromagnetischen Materialien besitzen bemerkenswerte Eigenschaften, wie zum Beispiel induzierter Magnetismus innerhalb des Graphen-Films, verstärkte magnetische Anisotropie innerhalb des ferromagnetischen Films und chirale magnetische Strukturen. Bislang wurde die Graphen-Ferromagnet-Grenzschicht hauptsächlich auf metallischen Substraten untersucht. Jedoch ist Siliziumkarbid (SiC) aufgrund seiner halb-isolierenden Eigenschaften und seiner industriellen Relevanz ebenfalls ein vielversprechendes Graphen-Substrat. Diese Arbeit befasst sich erstmalig mit der Interkalation von dünnen Kobalt-Filmen unter Graphen auf SiC, insbesondere mit den strukturellen, chemischen und magnetischen Eigenschaften der interkalierten Proben. Die 6H-SiC(0001) Proben wurden in einer Argon-Atmosphäre präpariert, um ein homogenes, großflächiges Wachstum der $\left(6\sqrt{3} \times 6\sqrt{3}\right)$-R30° (hiernach $6\sqrt{3}$) Oberflächen-Rekonstruktion zu erreichen. Die $6\sqrt{3}$ -Rekonstruktion kann als teilweise kovalent an das SiC gebundene Graphen-Schicht betrachtet werden. Es wird erwartet, dass die $6\sqrt{3}$-Struktur durch die Interkalation in einen Graphen-Film umgewandelt wird. Kobalt-Filme mit einer Schichtdicke t_{Co} von 0.4–12 nm wurden bei Raumtemperatur aufgedampft, bei welcher keine Reaktion des Kobalts mit der $6\sqrt{3}$-Oberfläche beobachtet wurde.

Während einer kontrollierten Erwärmung wurde die Temperatur- und Schichtdicken-Abhängigkeit des Interkalationsprozesses mittels Ultraviolett-Photoemissions-Elektronen-Mikroskopie (UV-PEEM) in Echtzeit untersucht. Die Interkalations-Temperatur hängt stark von der Kobalt-Schichtdicke ab, wobei das Minimum bei 340 °C für $t_{\mathrm{Co}} = 1.4\,\mathrm{nm}$ liegt. Die strukturellen und chemischen Eigenschaften werden mittels niederenergetischer Elektronenbeugung (LEED) und Röntgen-Photoelektronenspektroskopie (XPS) untersucht. Hierbei wird für geringe Kobalt-Schichtdicken eine partielle Umwandlung der $6\sqrt{3}$-Struktur in eine Graphen-Schicht beobachtet, wobei eine vollständige Umwandlung erst bei höherer Schichtdicke erreicht wird. Die unvollständige Umwandlung hängt mit einem Zerfall der Kobalt-Schicht in Inseln zusammen, welcher mittels durch Synchrotronstrahlung angeregter Photoemissions-Elektronenmikroskopie (X-PEEM) nachgewiesen wurde. Hierbei wurden Aufnahmen mit chemischem Kontrast an der Co L$_3$-Kante angefertigt. Weiterhin wird mittels XPS-Spektren des Si 2p-Signals und Röntgen-Absorptionsspektren (XAS) der Co L-Kante eine von t_{Co} unabhängige, selbst-limitierte Bildung von Kobalt-Silizid an der Co-SiC-Grenzschicht festgestellt. Die magnetischen Eigenschaften der Kobalt-Filme werden mittels an der Co L$_3$-Kante aufgenommenen X-PEEM-Aufnahmen mit magnetischem Kontrast untersucht. Für geringe t_{Co} zeigt sich eine selbst-assemblierte Bildung von Nanodrähten an den SiC-Stufenkanten, für mittleres t_{Co} eine durch Stufen-Anisotropie dominierte Domänenstruktur und für hohes t_{Co} eine dem Volumenkristall entsprechende Domänenstruktur.

Contents

1 Introduction

The successful isolation of graphene in 2004 [1] opened up the new scientific field of two-dimensional (2D) materials. Graphene consists of sp^2-hybridized carbon atoms arranged in an atomically thin honeycomb lattice and it is the prototype 2D material. Its experimental isolation was believed to be impossible for a long time, basically because it was considered too thin to be stable [2]. Following its first isolation, several extraordinary electronic and mechanical properties, such as a very high carrier mobility, mechanical strength, and thermal conductivity, were revealed [3–5]. Importantly, graphene was found to be a significant candidate for electronic [6, 7] and spintronic devices [8]. Furthermore, graphene can also serve as a non-magnetic spacer layer in magnetic tunnel junctions [9] or synthetic antiferromagnets [10]. The significance of graphene was underscored by the award of the Nobel prize in physics to Geim and Novoselov in 2010 [11, 12].

The pioneering experiments with graphene were carried out with flakes that were manually exfoliated from graphite by using adhesive tape [1]. While this method produces graphene layers of highest quality, it is not suitable for technological applications due to the involvement of significant manual work during the exfoliation and characterization of the obtained samples. Consequently, the feasibility of other graphene growth methods was elaborated in the past decade, for instance the chemical vapor deposition on transition metal substrates. This is an effective route for reproducible monolayer fabrication, but the graphene has to be transferred to a non-metallic substrate if usage in technological applications is intended [13]. Since any transfer of the graphene layer may be detrimental to its properties due to possible contamination, it is more desirable to grow it directly on a non-metallic substrate in order to avoid the transfer procedure.

A promising candidate for this purpose is the growth of graphene on silicon carbide (SiC). Silicon carbide is a wide-bandgap semiconductor that can be considered semi-insulating in its pure form. Therefore, it is ideally suited as a non-conducting graphene substrate. Furthermore, due to its established use in semiconductor industry, potential applications can make use of the existing infrastructure. The growth mechanism of graphene on the hexagonal SiC surfaces is based on high-temperature graphitization mediated by the relatively high vapor pressure of silicon compared to carbon [14]. Despite being known for a long time, this feature witnessed revived interest in the past decade as the graphene-like properties of graphite monolayers on SiC were revealed [15]. The quality of graphene on SiC was initially impeded by inhomogeneous growth due to the high graphene growth rate in ultra-high vacuum (UHV), which drastically reduces the achievable carrier mobility. This issue was successfully overcome by improved growth protocols that use an inert gas atmosphere instead of UHV [16–18]. At the same time, research on graphene on SiC revealed promising results, both for electronics and spintronics [6, 19].

The interest in fabricating interfaces of graphene on SiC with foreign elements is growing continuously. For instance, this roots in the desire to manipulate the electronic properties of the graphene layer [20]. Moreover, technological relevant multilayer structures inherently consist of several interfaces of graphene and other materials. A frequently used routine to generate interfaces between graphene and another material is the so-called intercalation. The term intercalation was coined for the insertion of so-called guest atoms into a host lattice that is usually a layered material like graphite, with strong bonding inside each plane and loose bonding between the individual planes [21]. In the case of graphene, intercalation describes the insertion of foreign atoms between graphene and its substrate. Intercalated materials enable the tailoring of the strength of the graphene-substrate interaction.

Intercalating foreign materials instead of simply depositing them on top of the graphene layer leads to multiple benefits. For instance, it was observed that metals form smooth intercalated films underneath graphene, whereas they showed unwanted clustering behavior if deposited on top of the graphene film [22]. Furthermore, due to the impermeability to gases [23], graphene effectively protects intercalated base metals from oxidation. A common observation during the intercalation of graphene on the SiC(0001) surface is the lifting of the $\left(6\sqrt{3}\times 6\sqrt{3}\right)$-R30° (hereafter $6\sqrt{3}$) surface reconstruction that inevitable forms during graphene growth on the SiC(0001) surface. The $6\sqrt{3}$ structure is a hexagonal carbon layer that is covalently bonded to the topmost silicon atoms and acts as a buffer layer between the substrate and the graphene film. The bonds between the $6\sqrt{3}$ structure and the silicon atoms can be substituted by intercalation of hydrogen atoms, which transforms the $6\sqrt{3}$ structure into a quasi-freestanding graphene film [24]. Further examples include the intercalation of gold and germanium that have been used for electron or hole doping of the graphene film [25, 26].

While many more materials have been successfully intercalated underneath graphene on SiC, not much is known about ferromagnetic thin films in this context. The graphene-ferromagnet interfaces are of special interest for spintronic applications, as they are part of spin injection or detection devices. An important result from previous research is that the hybridization of the electronic orbitals of graphene and the ferromagnet leads to induced magnetism in the graphene film [27–29]. In particular, cobalt is a promising candidate for graphene-ferromagnet interfaces due to the similar lattice constants of graphene and the Co(0001) surface [9].

Previously the graphene-cobalt interface has been investigated on metallic substrates in several studies [30–33]. Therein, it has been revealed that the magnetic anisotropy of the ferromagnet is affected by adsorbed graphene. In particular, the perpendicular magnetic anisotropy (PMA) of cobalt has been strongly enhanced by graphene on top of it. Furthermore, chiral magnetization textures resulting from the Dzyaloshinskii-Moriya interaction were surprisingly observed at the graphene-cobalt interface [34].

Yet, until now, the graphene-cobalt intercalation system on an SiC substrate was investigated only with sub-monolayer cobalt amounts intercalated underneath monolayer graphene grown in UHV [35, 36]. However, the intercalation of film thicknesses beyond one monolayer ($\approx 0.2\,\mathrm{nm}$) was not reported so far. The present thesis aims to reveal the feasibility of cobalt intercalation underneath graphene on the SiC substrate in a higher film thickness regime in order to produce films that are ferromagnetic at room temperature. For this purpose, the preparation of the silicon-terminated 6H-SiC(0001) samples was optimized to produce large areas of the $6\sqrt{3}$ surface reconstruction that is an appropriate starting point for graphene intercalation on SiC [25, 26]. Subsequently, cobalt films with film thicknesses in the range of 0.4–12 nm were deposited and the intercalation mechanism and the magnetic properties were investigated.

The activation temperature of the reaction with the $6\sqrt{3}$ reconstruction depends on the adsorbate and can reach from room temperature for lithium [37] up to 800 °C for gold [25]. By using ultraviolet photoemission electron microscopy (UV-PEEM), insights into the temperature and film thickness dependent cobalt intercalation mechanism will be given, as it is an excellent tool for the real-time imaging of chemical reactions. X-ray photoemission electron microscopy (X-PEEM) with chemical and magnetic contrast will provide information about the morphology of the cobalt film as well as its magnetic domain structure. The investigation of the magnetic domain structure will reveal the so-called easy-axes of the cobalt films. The easy-axes denote the directions along which the magnetic moments preferably align as a result of a combination of all sources of magnetic anisotropy. Since the substrate is a key source of anisotropy in thin film magnets [38], different easy-axes than those previously reported for graphene-cobalt systems on metallic substrates are expected. X-ray photoelectron spectroscopy (XPS) and low-energy electron diffraction (LEED) measurements will provide further information about the chemical and structural changes during the different preparation stages. Especially, it will be revealed whether the $6\sqrt{3}$ reconstructed surface transforms into a graphene covered surface and whether silicide compounds form at the interface to the SiC bulk. Complementary to the XPS measurements, x-ray absorption spectra (XAS) will be extracted from the X-PEEM images to gain insight into the chemical state of the cobalt atoms.

Following this introduction, the fundamental properties of SiC and the preparation of graphene will be outlined in chapter 2. In addition, some concepts of ferromagnetism are briefly summarized in order to provide a basis for the interpretation of the magnetic measurements. The theoretical foundations of the experimental methods will be discussed in chapter 3, whereas the instrumental realization and the sample preparation apparatus are described in chapter 4.

The results of the experiments are presented in chapters 5–7. In chapter 5, the $6\sqrt{3}$ reconstructed SiC samples will be thoroughly characterized in terms of their structural and chemical properties. In chapter 6, the changes to this properties after cobalt deposition at room temperature, as well as the magnetic properties in the as-deposited state are discussed. After this preparation, the temperature and film thickness dependent intercalation mechanism will be investigated in chapter 7. Moreover, the chemical changes at the cobalt-SiC interface due to the annealing procedure are revealed. Finally, the magnetic properties of the intercalated samples are analyzed in detail. Concluding remarks and an outlook containing suggestions for further studies will be given in chapter 8.

2 Background

In this chapter, background information is given, which is beneficial for the understanding of the results presented in this thesis. In the first section, the atomic structure of graphene as well as its growth and intercalation on a silicon carbide substrate are introduced. The second section briefly summarizes a few concepts of ferromagnetism, which are helpful for the understanding of the PEEM measurements with magnetic contrast.

2.1 Graphene on silicon carbide

2.1.1 Graphene

Graphene is a two-dimensional crystal that can be regarded as a single sheet of a graphite crystal. Its atomic structure is composed of a hexagonal honeycomb lattice with next-neighbor distances of 1.42 Å and a lattice constant of 2.46 Å. Figure 2.1 displays the atomic structure of graphene with indicated lattice vectors. The unit cell consists of two atoms of which those at the corners and those inside the cell belong to two different sublattices. The carbon atoms inside the graphene lattice are sp^2-hybridized. Consequently, each carbon atom forms three in-plane σ-bonds and one out-of-plane π-bond with the adjacent carbon atoms. One of the key properties of graphene directly results from its the honeycomb structure. That is, its electronic band structure exposes a linear dispersion relation in the vicinity of the $\bar{K}$-point of the Brillouin zone [39].

The experimental isolation of graphene came as a surprise because a strictly two-dimensional crystal cannot exist in theory, since thermal fluctuations would destroy it at any finite temperature. Yet, the experimental evidence of the existence of graphene is not in contradiction with theory. Most experiments with graphene are not carried out with free-standing graphene, but with graphene deposited on a substrate, which makes it part of a three-dimensional system. The restrictions for two-dimensional crystals therefore do not apply anymore. Moreover, experiments with suspended graphene sheets that were free-standing over hundreds of nanometers in both lateral dimensions have shown that the graphene film conserves its crystallinity, but exhibits

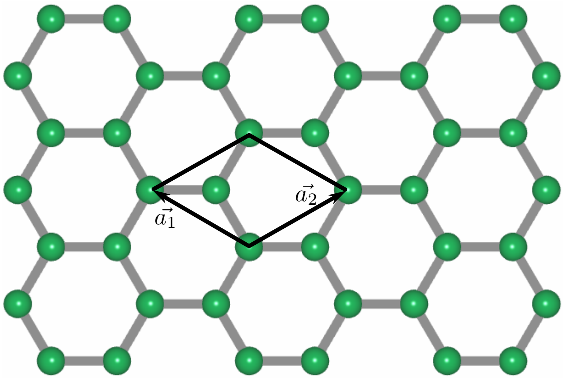

Figure 2.1: The atomic structure of a graphene monolayer. The lattice vectors $\vec{a}_1$ and $\vec{a}_2$ and the resulting unit cell are indicated.

out-of-plane deformations [40]. These deformations into the third dimension ensure the stability of the film.

The first dedicated graphene experiments were carried out with graphene flakes mechanically exfoliated from graphite crystals and deposited on silicon wafers [1]. This approach leads to high-quality flakes and is very valuable for basic research, but it requires significant manual work to prepare the samples, as graphene monolayers have to be identified among multilayers deposited during the exfoliation process. In order to facilitate practical applications, various graphene growth methods were explored [41]. One of them is epitaxial growth on silicon carbide that has been proposed to be one of the most promising candidates for electronic applications [16, 18, 20].

2.1.2 Silicon carbide

Being a stoichiometric compound of silicon and carbon, silicon carbide (SiC) is a wide-bandgap semiconductor with applications in high-frequency, high-power, and high-temperature environments [42]. The crystal structure consists of stacked Si-C double layers that are connected either congruently or rotated at an angle of 60°. These different possibilities result from the tetrahedral Si-C bond geometry. An SiC double layer is depicted in figure 2.2 and the two possible stacking sequences are illustrated in figure 2.3.

The two sorts of connection between the double layers lead to a wealth of potential crystal structures [43]. Each of them is called a polytype and is characterized by the number of double layers in the unit cell and by the crystal symmetry. The most common polytypes are the cubic 3C-SiC, and the hexagonal 4H-SiC and 6H-SiC.

Depending on the polytype, the band gap of SiC amounts to 2.4–3.3 eV. In this work, the 6H-SiC polytype is exclusively used. Its lattice constants are $a = 3.08\,\text{Å}$ and $c = 15.12\,\text{Å}$ [44]. The (0001) and $(000\bar{1})$ surfaces of hexagonal SiC are exclusively terminated either by silicon or carbon atoms. Therefore, these surfaces are called polar. Conventionally, the silicon-terminated and carbon-terminated surfaces are referred to as (0001) and $(000\bar{1})$, respectively.

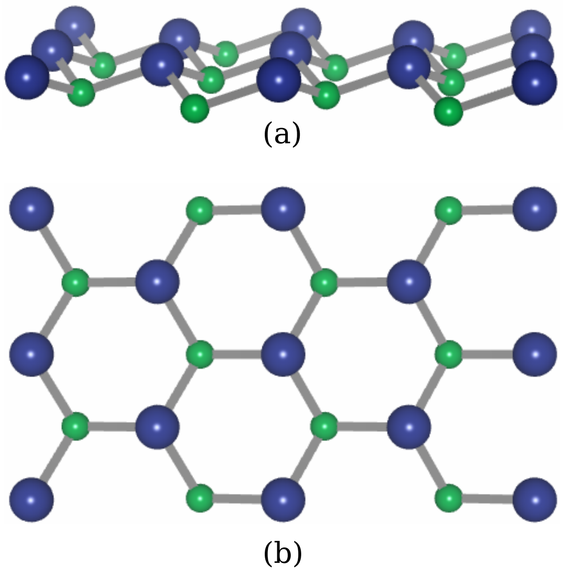
(a)

(b)

Figure 2.2: (a) Side-view and (b) top-view of an SiC double layer, which is the basic constituent of any SiC crystal structure. The silicon and carbon atoms are depicted as large blue and small green circles, respectively.

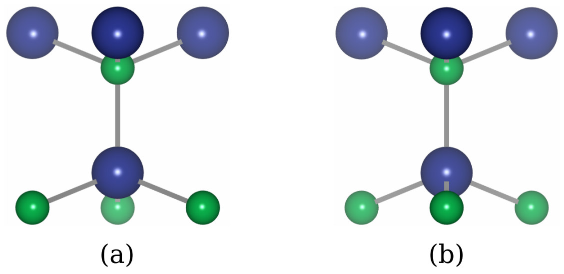
(a)

(b)

Figure 2.3: Illustration of the two possible sixty-degree-rotated SiC double layer stacking sequences, which result from the tetragonal Si-C bond geometry. The silicon and carbon atoms are depicted as large blue and small green circles, respectively.

2.1.3 Graphene growth on silicon carbide

Principle

The growth of graphene on SiC surfaces is based on high temperature annealing of the crystal in vacuum or inert gas atmosphere. Since the vapor pressure of silicon is orders of magnitude higher than that of carbon, significantly more silicon atoms evaporate, which causes a carbon-enrichment at the surface. Graphene growth is feasible on both the SiC(0001) and the SiC($000\bar{1}$) surfaces of which the former is silicon-terminated and the latter is carbon-terminated. On the carbon-terminated surface, each new graphene layer grows in a random orientation with respect the layer underneath [14]. This random orientation is sometimes considered beneficial because it decreases the interaction of the individual graphene layers [18]. However, the graphene growth rate on the carbon-face is much higher than on the silicon-face, which complicates the reproducible growth of monolayers. In the following, carbon-face growth will not be considered anymore.

At the silicon-terminated SiC(0001) surface, the carbon-enrichment during the annealing process induces two distinct surface reconstructions. The $\left(\sqrt{3} \times \sqrt{3}\right)$-R30° reconstruction occurs above 1000 °C, and the $\left(6\sqrt{3} \times 6\sqrt{3}\right)$-R30° reconstruction occurs above 1100 °C [42]. Once the transformation into the $6\sqrt{3}$ reconstruction is complete, further silicon evaporation leads to the formation of a new $6\sqrt{3}$ structure underneath. Simultaneously, the covalent bonds of the upper $6\sqrt{3}$ structure and the substrate are lifted and the topmost carbon layer transforms into a monolayer of graphene [20]. Prolonged annealing will eventually lead to the completion of the first monolayer of graphene and subsequently the formation of additional graphene layers will occur due to the same mechanism. The $6\sqrt{3}$ structure serves as a buffer layer to adjust the lattice constants $a_{\mathrm{g}} = 2.46\,\text{Å}$ and $a_{\mathrm{S}} = 3.08\,\text{Å}$ of graphene and SiC, respectively. Further, the $6\sqrt{3}$ interface layer causes a charge transfer from the SiC bulk to the first graphene layers which results in an electron doping of these layers [45]. The $6\sqrt{3}$ structure and each subsequent graphene layer have the same 30° rotated orientation with respect to the substrate. In figures 2.4 (a) and (b), the atomic structures of the bare $6\sqrt{3}$ reconstruction and of monolayer graphene are displayed in a side view. Note that in figure 2.4 (b) the graphene monolayer is supported by an otherwise unchanged $6\sqrt{3}$ structure.

The atomic structure of the $6\sqrt{3}$ reconstruction was subject of a long debate. Now, it is considered to be a hexagonal carbon layer with the same lattice constant as graphene [46]. The $6\sqrt{3}$ periodicity is due to corrugations resulting from the covalent bonds with the substrate of about one-third of the carbon atoms in the $6\sqrt{3}$ structure. Since the atomic structure of the $6\sqrt{3}$ layer differs from graphene,

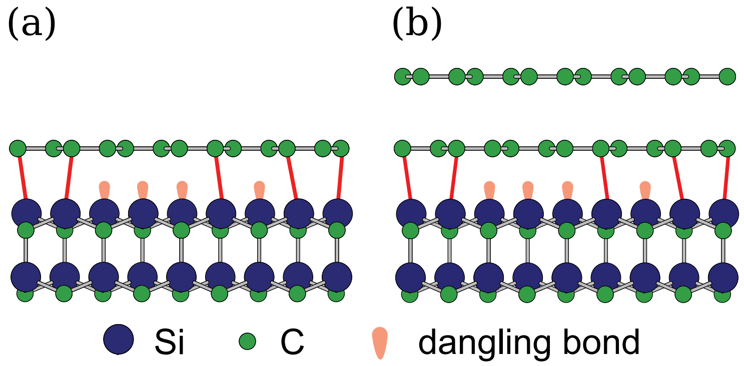

Figure 2.4: The atomic structure of graphene on SiC [20]: (a) bare $6\sqrt{3}$ reconstruction, (b) monolayer graphene. Note the preservation of the $6\sqrt{3}$ reconstruction underneath the graphene monolayer in (b).

the same applies to its electronic properties. Most notably, the electronic band structure of the $6\sqrt{3}$ layer does not contain a linear dispersion relation.

Practical aspects

The growth of graphene on SiC by vacuum annealing as described in the previous section has one disadvantage. Namely, the size of the individual graphene single crystals is limited to about 100 nm [16]. This is due to the low mobility of the carbon atoms at the usual growth temperature of about 1100 °C. An increase of the mobility by a higher growth temperature is not feasible, due to the resulting higher growth rate leading to graphene multilayers. Ideally, an increase of the carbon mobility and a low graphene growth rate have to be maintained simultaneously.

A solution to this problem is to anneal the SiC crystal in an inert gas atmosphere instead of ultra-high vacuum [16]. Due to collisions with the inert gas atoms, the evaporation rate of the silicon atoms is reduced. Consequently, the growth can be performed at temperatures of 1500 °C or even higher. Another method for the reduction of the graphene growth rate is the so-called confinement controlled sublimation in ultra-high vacuum [18]. Here, a small crucible confines the sample and allows the silicon vapor to escape only by a small leak. Therefore, the partial pressure of silicon above the sample is locally increased, which provides a similar growth rate reduction as the inert gas method. Finally, the confinement controlled sublimation method can be combined with an inert-gas atmosphere as a further route for growth rate reduction.

2.1.4 Intercalation of graphene on silicon carbide

The insertion of a foreign material between graphene and its substrate is called intercalation, in analogy to graphite intercalation compounds. Here, the foreign material is adsorbed on the graphene and thermal annealing triggers a process in that graphene and the adsorbate change their places. The driving force for the intercalation process depends on the particular substrate and adsorbate that are used. In the case of monolayer graphene on SiC(0001), some studies found that the intercalant moves in between the graphene layer and the $6\sqrt{3}$ reconstructed layer upon thermal annealing [35, 36]. Consequently, the $6\sqrt{3}$ structure remains intact. Conversely, it has also been observed that intercalants can penetrate the $6\sqrt{3}$ reconstructed carbon layer and substitute the covalent bonds of the $6\sqrt{3}$ layer with the topmost silicon layer [25, 26, 47]. During this process, the $6\sqrt{3}$ reconstruction is lifted, and the atoms of the reconstructed carbon layer rearrange into an additional graphene layer.

As an illustration, figure 2.5 (b) displays the atomic structure of hydrogen-intercalated bilayer graphene that results from the hydrogen intercalation of the monolayer graphene depicted in figure 2.4 (b) and the associated decoupling of the underlying $6\sqrt{3}$ reconstruction. The hydrogen intercalation can be achieved by annealing of the sample at temperatures in the range of 600–1000 °C in molecular hydrogen at atmospheric pressure [24]. As a consequence of the decoupling of the $6\sqrt{3}$ structure, it is also possible to start an intercalation experiment with the bare $6\sqrt{3}$ reconstruction without any further graphene layer on top. In this case, the atomic structure displayed in figure 2.4 (a) would be transformed into the structure displayed in figure 2.5 (a). This work focuses on the intercalation starting with the $6\sqrt{3}$ reconstruction.

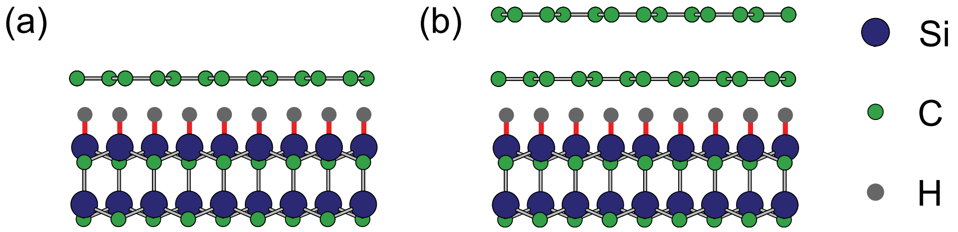

Figure 2.5: The atomic structure of hydrogen-intercalated graphene on SiC [20]: (a) hydrogen-intercalated monolayer graphene, and (b) hydrogen-intercalated bilayer graphene.

Two characteristic intercalation mechanism can be distinguished depending on the intercalant [48]. First, the intercalation occurs in all areas of a graphene layer at once. In this case, the intercalant atoms migrate through pre-existing or induced defects in the graphene layer. This mechanism results from a high reactivity of the intercalant towards carbon. In the second mechanism that was observed for weakly interacting intercalants, the intercalation starts at the edges of the graphene layer. Both mechanisms were observed previously for the intercalation underneath the bare $6\sqrt{3}$ reconstruction on SiC [26, 49].

2.2 Ferromagnetism

2.2.1 Spontaneous magnetization

Ferromagnetism is characterized by a spontaneous magnetization, that is, a net magnetization even in the absence of an external magnetic field. This distinguishes it from paramagnetism, diamagnetism, and other forms of magnetic order. Similar to paramagnetism but contrary to diamagnetism, ferromagnetism involves permanent magnetic moments that result from the spin of the electron. Note that the magnetic moment of the nucleus is smaller by orders of magnitude and thus do not contribute to the magnetization. The driving force for the spontaneous magnetization is the exchange interaction, whose energy scale is orders of magnitude higher than that of the dipole-dipole interaction. Therefore, the latter does not contribute to the parallel alignment of the spins [50].

The exchange interaction roots in the Pauli principle that prevents two electrons with the same spin from approaching each other too closely. As a result, the mean distance between electrons with parallel spin is higher than that with anti-parallel spin, which leads to a reduced density of electrons with the same spin direction in the vicinity of a particular electron. This leads to a reduction of the associated charge density, which is commonly referred to as exchange hole [51]. In consequence, the Coulomb repulsion is reduced for electrons surrounded by like-spin electrons, which leads to a energetic preference of parallel-aligned spins. This mechanism can lead to spontaneous magnetization because the electrons exchange until large areas with equally aligned spin emerge. However, in many cases, thermal fluctuations will prevent the emergence of permanent magnetic order and the material behaves paramagnetic. Permanent order is only possible below a material-specific critical temperature T_C, which is called Curie temperature. Iron, nickel, and cobalt are the only elements with T_C significantly above room temperature, while the T_C of gadolinium is about room temperature [52]. As T_C depends on the coordination number of the atoms in a system, it is reduced for thin films and surfaces [51].

2.2.2 The band model of ferromagnetism

The ferromagnetism of iron, nickel, and cobalt is caused by their 3d electrons. They are de-localized and their energy levels are smeared out to energy bands, which is why the magnetism of these systems cannot be explained by interacting atomic moments. Instead, the band structure of the 3d electrons must be regarded, which leads to the so-called Stoner model [52]. The Stoner model can be derived by the Hartree-Fock approximation of the Hubbard model [53]. Figure 2.6 schematically depicts the electronic band structure of a ferromagnetic 3d metal. Therein, the density of states $\rho(E)$ near the Fermi energy E_F is displayed separately for spin-up and spin-down electrons, which are also called majority and minority spins, respectively.

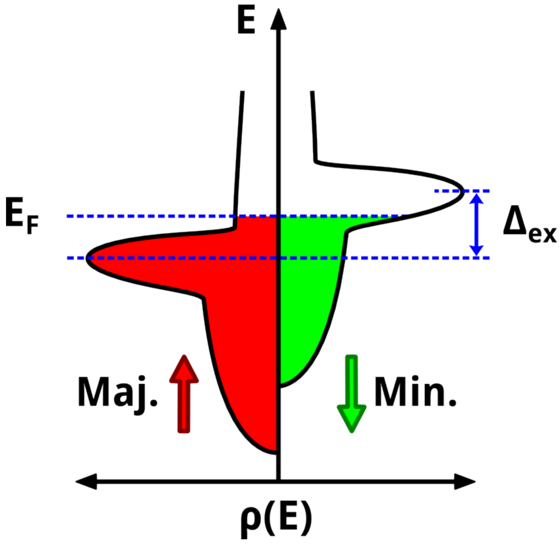

Figure 2.6: Sketch of the spin-dependent electronic density of states of a ferromagnet as an illustration of the band model of ferromagnetism [54].

As can be seen in figure 2.6, the energy bands of the majority and minority spins are energetically separated by Δ_ex due to the exchange interaction. Since the Fermi level remains the same for both spin channels, the majority band is occupied by more electrons than the minority band. As a result, a net magnetic moment evolves. The magnetic moment per atom can be calculated from the excess of the majority over the minority spins.

Within the band model, the so-called Stoner criterion for the occurrence of ferromagnetism can be derived [55]:

$$I\rho\left(E_\mathrm{F}\right) > 1. \tag{2.1}$$

Here, I denotes the so-called Stoner parameter. The parameter I is the exchange-correlation integral and therefore a measure for the energy reduction due to the exchange interaction. The Stoner criterion shows that ferromagnetism occurs in the case that the exchange interaction and the density of state at E_F are large. It was shown that this criterion correctly predicts ferromagnetism only for the elements iron, nickel, and cobalt [56].

2.2.3 Magnetic anisotropy

The exchange interaction can explain the parallel alignment of spin moments, but it does not define a preferred magnetization direction with respect to the crystal lattice. This is because the spin is not directly coupled to any crystal direction [52]. Yet, experimentally, it is observed that the magnetic field necessary to saturate the magnetization depends on the field direction with respect to the crystal axes. Those axes along which a relatively low field is required are called easy axes, while those for which a relatively high field is necessary are called hard axes. Depending on the crystal symmetry, one or multiple easy axes exist. The microscopic origin for the preference of the easy over the hard axes is the magnetic anisotropy. Fundamentally, two sources of anisotropies are distinguished.

First, the magneto-crystalline anisotropy reflects the crystal symmetry. It results from the spin-orbit interaction since the electrons also possess an orbital momentum besides the magnetic moment associated with their spin. The orbital momentum is locked to the crystal lattice due to the bonding. The interaction of the spin and orbital momenta then leads to the alignment of the magnetization with a crystal axis [52]. Second, the reduction of the energy associated with the magnetic stray field outside the crystal leads to the so-called shape anisotropy. Microscopically, it results from dipole-dipole-interaction. It is particularly important in thin films since it leads to an in-plane magnetization as the magnetic stray field is lower if all magnetic moments are aligned in the film plane as if they were aligned perpendicular to the plane [57].

As the magneto-crystalline anisotropy reflects the symmetry of the crystal, any structural change to a magnetic material may have an effect on the resulting easy axis. For instance, for very thin films the symmetry at the surface is lowered, which leads to a change of the magneto-crystalline anisotropy. While an in-plane magnetization due to the shape anisotropy is routinely observed for thin films, the magneto-crystalline anisotropy can overcome the shape anisotropy in special cases. This typically happens for film thicknesses about 1 nm and results in an out-of-plane easy axis [58]. This effect is known as perpendicular magnetic anisotropy.

Several further anisotropies were observed for special cases, which ultimately can be traced back to the two aforementioned interactions. Especially, for thin magnetic films, the interface of the film with its substrate is becoming important. Here, any interdiffusion, roughness, or steps affect the magnetic anisotropy [59]. Generally, the actual magnetic easy axis depends on the competition of all sources of anisotropy. However, the small energy values associated with the magnetic anisotropy complicates a prediction of the easy-axes for a given system [52]. Therefore, the experimental determination of the easy-axes for a new system is indispensable.

2.2.4 Magnetic domains

When a ferromagnetic sample is heated above the Curie temperature and cooled down again, the spontaneous magnetization sets in. Now, the exchange interaction and the magnetic anisotropy allow a uniform magnetization without the application of an external field [52]. However, the magnetization causes a stray field with an associated energy. In order to minimize this stray field energy, the magnetization will break up into several areas, which are called magnetic domains. Inside the individual domains, the magnetization is aligned along one of the easy axes. Thus, the observation of magnetic domains with microscopic techniques directly allows the determination of the magnetic easy axes.

In each domain the magnetization is saturated but the adjacent domains are differently oriented, therefore the average magnetization is minimized [60]. The transition zone between different magnetic domains in that the magnetization must rotate from one to another direction is called a domain wall. The width of the domain walls is determined by a competition between the exchange and the anisotropy energies [57]. The minimization of the exchange energy would favor a gradual rotation over an extended length while an abrupt change from one easy direction to another would minimize the anisotropy energy. Since the magnetization inside a domain wall is not aligned with the easy axis, the domain wall increases the total energy. Especially for ultra-thin films or very small particles, the stray field energy associated with a single domain state may be lower than the domain wall energy [60]. Therefore, single domain states may exist even in a spontaneously magnetized sample.

3 Experimental methods

The analysis of graphene intercalation processes requires surface sensitive methods. All techniques used in this thesis are based on electron detection, whose surface sensitivity results from the low inelastic mean free path (IMFP) of low-energy electrons in solids. In the first section of this chapter, the IMFP and the photoelectric effect as the primary electron excitation mechanism used in this work are discussed. Based on these fundamentals, the principles of the experimental techniques photoelectron spectroscopy, photoemission electron microscopy, and low-energy electron diffraction are outlined in the following sections.

3.1 Fundamentals

3.1.1 Inelastic mean free path of electrons in solids

The mean distance that an electron with the kinetic energy E_{kin} propagates through a solid without being inelastically scattered is quantified by the inelastic mean free path λ. This holds regardless of the process in that the electron was excited. The intensity I of unscattered electrons with a given kinetic energy traveling through the solid decays exponentially over the distance d:

$$I(d) = I_0 \exp(-d/\lambda) \,. \tag{3.1}$$

During propagation through the solid, an electron may be scattered inelastically by electron-electron and by electron-phonon interaction [57]. Though, the energy loss due to electron-phonon scattering is negligibly small. The nature of the electron-electron interaction depends on whether E_{kin} is lesser or greater than the plasmon energy E_{p} [61]. Below E_{p} and above E_{p} the dominating processes are single-electron scattering and plasmon excitations, respectively.

The dependence of the IMFP on E_{kin} is often described by a universal curve since it is roughly the same regardless of the material under consideration. More precisely, the values obtained in the same experiment for different elements scatter to the same extent as values obtained in different experiments for the same element [62]. However, while the independence of the material is approximately valid for high E_{kin}, the IMFP is strongly material-dependent for the lowest E_{kin} [62]. In 1979, Seah and Dench carried out an analysis of the available experimental data to that date and found universal curves

$$\lambda\left(E_{\mathrm{kin}}\right)=\frac{A}{E_{kin}^{2}}+B\sqrt{E_{kin}} \tag{3.2}$$

that fit the IMFP with different parameters A and B for metals, inorganic, and organic compounds [63]. Figure 3.1 displays the universal curve for elemental solids with $A = 143\,\mathrm{nm}\cdot\mathrm{eV}^2$ and $B = 0.054\,\mathrm{nm}\cdot\mathrm{eV}^{-0.5}$. Here, the minimal $\lambda_{\mathrm{min}} \approx 0.4\,\mathrm{nm}$ is achieved for $E_{\mathrm{kin}} \approx 40\,\mathrm{eV}$. For $E_{\mathrm{kin}} > 150\,\mathrm{eV}$ the first term in equation 3.2 can be neglected. Furthermore, a comprehensive database of the IMFP for $E_{\mathrm{kin}} > 50\,\mathrm{eV}$, based on theory and experiment, can be found in reference [64].

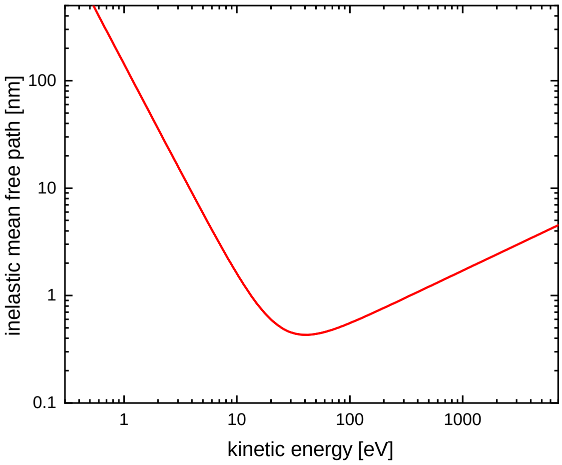

Figure 3.1: Inelastic mean free path of electrons in elemental solids according to equation 3.2.

According to equation 3.1, on average 63 % of all electrons are inelastically scattered after the path length of 1 λ. Hence, the information depth of electron detection based methods is limited to the first atomic layers of the solid, if E_{kin} is chosen near the minimum of the IMFP. After having discussed the IMFP, in the next section the primary electron excitation mechanism used in this thesis, the photoelectric effect, is presented.

3.1.2 The photoelectric effect

The observation that irradiation with light of sufficient frequency ν results in the ejection of electrons out of solids is called the photoelectric effect. This effect cannot be understood in terms of classical physics, which motivated Einstein to propose a quantized nature of the light-matter interaction [65]. During the photoelectric effect, a photon is absorbed by the solid and its energy is transferred to an electron. The kinetic energy of the electron

$$E_{\text{kin}} = h\nu - E_{\text{bin}} - \phi \tag{3.3}$$

depends on the photon energy hν, the binding energy E_{bin} of the electron with respect to the Fermi level, and the work function of the sample ϕ. The work function ϕ of a solid is defined as $\phi = E_{\text{vac}} - E_{\text{F}}$ with the vacuum level E_{vac} and the Fermi level E_{F}. In principle, it can be calculated by the energy difference of the n and $(n-1)$ electron system. The ϕ-values of the elements span the range of 2–6 eV.

After ejection of the electron, the solid is left in an excited state. Subsequently, an electron with lower E_{bin} fills up the unoccupied state in order to lower the total energy of the solid. The released energy is either transferred to a third electron in the so-called Auger-Meitner process, or to a fluorescence photon. In both the Auger-Meitner and the fluorescence processes, the released energy depends solely on the involved core-levels. Consequently, the energies of the emitted fluorescence radiation as well as the Auger electrons are element-specific. The photoemission from core-levels and the associated relaxation processes as well as the photoemission from the valence band are illustrated in figure 3.2.

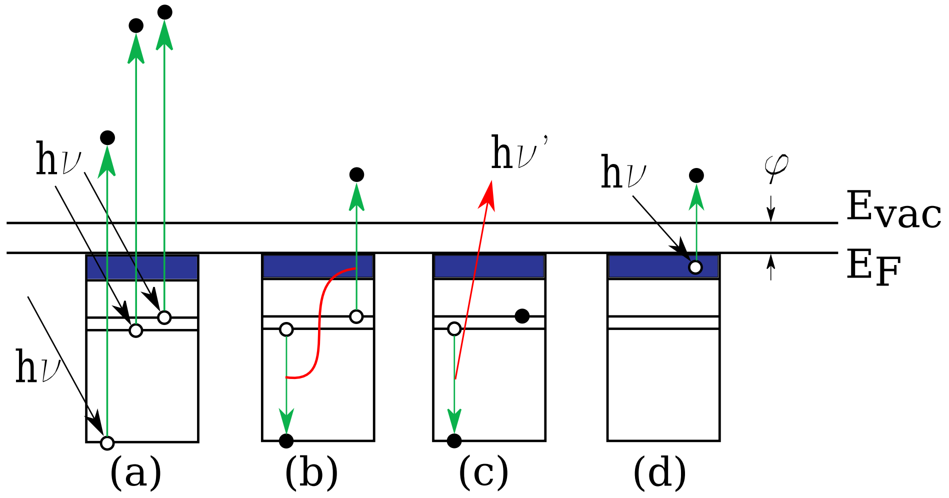

Figure 3.2: Illustration of the photoelectric effect and the associated relaxation processes: (a) photoelectric effect, (b) relaxation by emission of an Auger electron, (c) relaxation by emission of characteristic x-rays, and (d) photoemission from the valence band.

Depending on the atomic number Z of the element under consideration either the Auger-Meitner or fluorescence effect occur preferably. The Auger-Meitner effect dominates for low Z and the fluorescence effect for high Z. While unscattered Auger electrons appear as additional peaks in photoelectron spectra, cascades of inelastically scattered Auger electrons contribute to the secondary electron peak. The fluorescence effect is not further considered in this work since all experimental methods are based on electron detection.

The applicability of the photoelectric effect in core-level spectroscopy is due to the fact that a photon is completely absorbed during the excitation of an electron. Therefore, a simple relationship between $h\nu$ and E_{kin} exists. In contrast, an incident electron would transfer its E_{kin} in multiple scattering events, hence producing a broad energy distribution rather than a sharp peak. The application of the photoelectric effect for photoelectron spectroscopy and photoemission electron microscopy is addressed in the next sections.

3.2 Photoelectron spectroscopy

In photoelectron spectroscopy (PES) the number of electrons emitted from an irradiated solid is measured as a function of their kinetic energy that is determined by equation 3.3. Since the photon energy and the work function are constants, PES therefore enables the determination of the binding energy spectrum of the solid. Depending on whether the focus of the experiment are the core-levels or the valence band, PES is called x-ray photoelectron spectroscopy (XPS) or ultra-violet photoelectron spectroscopy (UPS), respectively. This distinction results from the usage of x-ray tubes or ultraviolet lamps as light sources. With the widespread availability of synchrotron radiation, it is now of minor importance. In this thesis, the focus is solely on core-level spectroscopy.

The information depth of PES is determined by the IMFP that was discussed in section 3.1.1. This results from the fact that electrons that suffered an undefined energy loss due to inelastic collisions no longer bear the information of the binding energy. The information depth can be varied by tuning the angle between the spectrometer and the sample surface, which is called the polar angle θ. While the surface sensitivity is already high in the case of normal emission, it can be further enhanced in the case of grazing emission. For grazing emission at the angle θ, the path length for electrons emitted from a depth d below the surface is increased to $d/\cos\theta$. Consequently, for grazing emission, the probability for inelastic collisions is enhanced, which increases the surface sensitivity.

Figure 3.3 illustrates the principle of PES. Therein, the relationship of the density of states (DOS) of a solid and the resulting PES spectrum is depicted. Green arrows indicate the excitation of electrons from different energy levels by photons of the same energy. The depicted spectrum is a so-called survey spectrum with a usual width of some 100 eV. Therein, excitation from the core-levels results in sharp peaks, whereas the valence band translate to a broad feature. Since the binding energies of the core-levels depend on the chemical element, the appearance of peaks at certain energies indicate the presence of a specific element. Survey spectra therefore yield information about the elemental composition of the sample. Importantly, the high surface sensitivity of PES allows a quick check for the cleanliness of a surface by means of a survey spectrum.

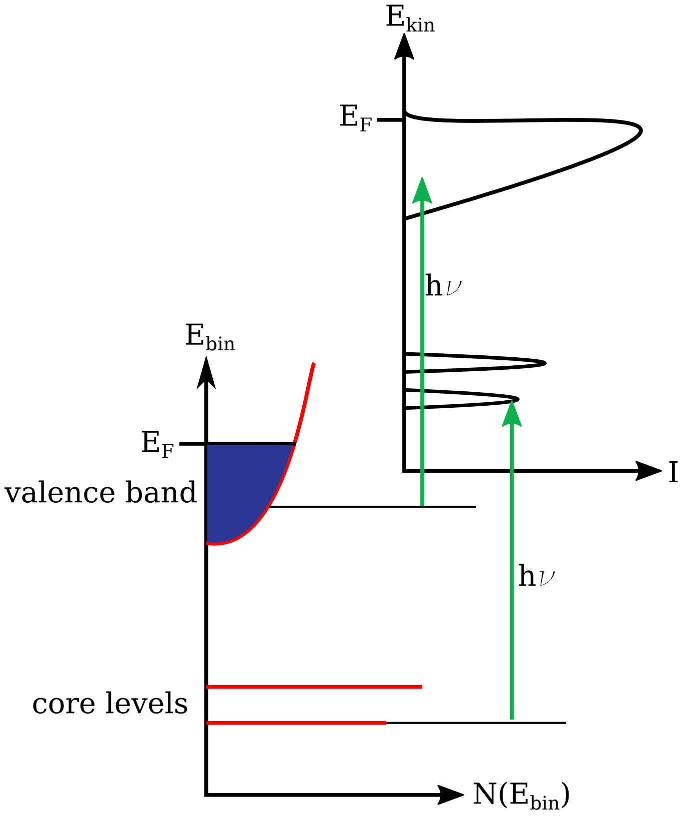

Figure 3.3: The relation of the density of states, displayed in the lower left and the photoelectron spectrum, displayed in the upper right.

Along with the core-level peaks, several further lines such as Auger or energy-loss peaks are observable in a photoelectron spectrum. The Auger peaks are generated due to the relaxation process following the photoemission, as described in the previous section. Their kinetic energy may overlap with that of a core-level peak of interest. Yet, since the kinetic energy of the Auger electron does not depend on the photon energy, shifting of the photon energy would separate the Auger and core-level peak. An example for energy-loss peaks are plasmon peaks that are due to quantized excitations of the charge carrier density by photoelectrons traveling to the surface of the solid. They usually appear associated with strong photoelectron lines. The photoelectrons also lose energy by un-quantized processes. These lead to a continuous background increasing for lower kinetic energy.

A detailed inspection of core-levels in high-resolution spectra of a narrow energy region yields information about the chemical environment of the atoms. This results from the so-called chemical shift that occurs due to a binding energy difference proportional to the relative electronegativity of the bonding partners of a certain atom. As an illustration of the effect, in figure 3.4 the C 1s core-level spectrum of ethyl-trifluoroacetate is depicted. Therein, four chemical shifted components resulting from different chemical environments of the carbon atoms are clearly visible.

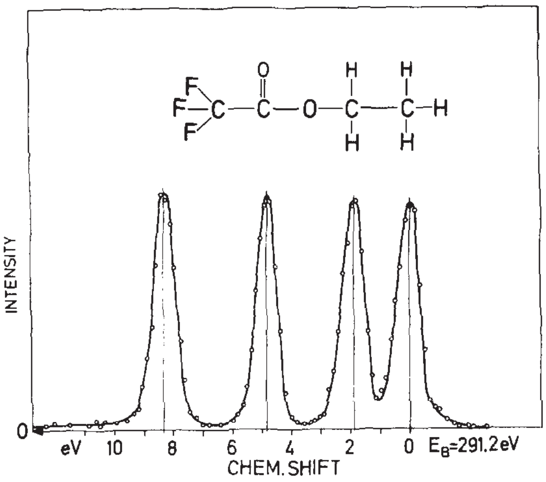

Figure 3.4: C 1s photoelectron spectrum of etyhl-trifluoracetat [66]. Four chemically-shifted components resulting from the different chemical environments of the carbon atoms in the molecule are clearly visible.

Concerning the chemical elements present in this particular molecule, the fluorine atoms possess the highest electronegativity and the hydrogen atoms possess the lowest. Consequently, the chemical shift is strongest for the carbon atoms bound to fluorine atoms and weakest for the carbon atoms bound to hydrogen atoms. While the chemically shifted components are well separated in this example, more often, the chemical shifts are less pronounced. Rather they are of the order of 1 eV, which is of the same magnitude as the width of a core-level peak. Hence, the individual chemically shifted components are frequently not directly resolved by inspection of the raw data.

Core-level lines with non-vanishing angular momentum quantum number l are splitted into doublet components due to the spin-orbit coupling. The spin-orbit coupling of the electron results from the interaction of the magnetic moments associated with its orbital and spin angular momenta. Due to this interaction, the orbital $\vec{l}$ and spin $\vec{s}$ momenta are no constants of motion. Instead, the total angular momentum $\vec{j} = \vec{l} + \vec{s}$ is defined. The interaction energy depends on parallel or anti-parallel alignment of the projections of the spin and the orbital momenta. The total angular momentum quantum number j takes the values $j = l \pm 1/2$ depending on parallel or anti-parallel alignment [67].

Consequently, a p-orbital splits into the $\mathrm{p}_{1/2}$ and $\mathrm{p}_{3/2}$ states. The total angular momentum takes all half-integer values between $-j$ and j. Therefore, the levels are $2j + 1$ times degenerate, which determines the occupation number of the individual levels. The intensity ratio of spin-orbit splitted core-levels is given by the ratio of their degeneracy. Again, for a p-orbital the intensity ratio of $\mathrm{p}_{3/2}$ and $\mathrm{p}_{1/2}$ is a factor of 2. Since a higher total angular momentum is associated with lower binding energy, the kinetic energy of the photoelectrons increases with the total angular momentum. The spin-orbit splitting is illustrated in figure 3.5 on the example of the Si 2p core-level. Here, the two spin orbit split components of the Si $2\mathrm{p}_{3/2}$ and $2\mathrm{p}_{1/2}$ levels are clearly resolved with an energy difference of 0.608 eV. As expected, the intensity ratio of both components is 2/1.

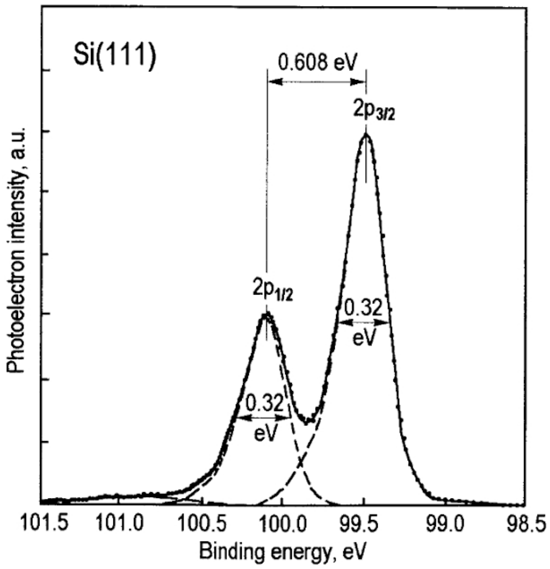

Figure 3.5: High-resolution Si 2p core-level spectrum, clearly resolving the two spin-orbit split components [68] after [69].

As already indicated, the core-level spectra may consist of several components, therefore a peak fitting procedure must be applied in order to reveal the full information of the spectrum. For this purpose, mathematical models for the peak shape are necessary. Hypothetically, for a strictly monochromatic light source and an infinite lifetime of the core hole, the photoemission peak would be a δ-function [70]. To understand the realistic peak shapes, it is useful to rewrite equation 3.3 as

$$E_{\mathrm{kin}} = h\nu - \left(E_f - E_i\right) - \phi. \tag{3.4}$$

Here, the binding energy E_{bin} has been replaced by the difference between the total energies of the final and initial states E_f and E_i. Consequently, the measured kinetic energy spectrum depends on the final state. In the final state, the solid relaxes in order to neutralize the core hole. The finite lifetime of the core hole then leads to a broadening of the photoemission line due to the uncertainty principle. The lifetime broadening leads to a convolution of the ideal δ-peak with a Lorentzian [71], the result of which is a Lorentzian peak shape since the δ-function is the neutral element of the convolution. The actual lifetime of the core hole is determined by the relaxation processes that were discussed in section 3.1.2.

The Lorentzian peak shape is only valid for non-metals, since in the case of a metal, the core hole is rapidly screened by conduction band electrons. This screening involves the formation of electron-hole pairs with a probability increasing like $1/\mathit{\Delta} E$. Here, $\mathit{\Delta} E$ is the binding energy of the electron-hole pair [62]. Due to the many possible electron-hole pair binding energies, the final state is smeared out. Hence, the photoemission peak gains a tail towards lower kinetic energy. More precisely, the δ-peak is replaced by a power law diverging at the threshold, taking into account the higher probability for low-binding-energy pairs. Convoluting the power law with the Lorentzian due to the core hole lifetime, leads to the so-called Doniach-Sunjic profile [70]. The Doniach-Sunjic profile is asymmetric with a tail to lower kinetic energy. The asymmetry is quantified by an asymmetry parameter α.

Finally, all experimental influences such as linewidth of the light source or the resolution of the spectrometer contribute to a Gaussian broadening. The convolution of a Gaussian and a Lorentzian function is called Voigt profile.

Along with the peak fitting procedure of core-level spectra, the inelastic background must be removed. Several methods for background correction exist, of which the simplest approach is the subtraction of a straight line or a polynomial of low order. This method can only be applied if the background contribution to the spectrum is small, for instance for peaks resulting from mainly unscattered photoelectrons of near-surface species. More generally, the background can be written as

$$B\left(E\right) = \int_{E}^{\infty} K\left(E' - E\right) j'\left(E'\right) dE', \tag{3.5}$$

where $j'(E)$ is the spectrum at energy E and K is the inelastic energy-loss function [72]. If a constant loss function is assumed, equation 3.5 yields the so-called Shirley background, whereas an energy dependent loss function is implemented in the Tougaard background. In most cases, the Shirley background is sufficient even for buried species [73].

3.3 Photoemission electron microscopy

In photoemission electron microscopy (PEEM), the electrons with the lowest energy that were emitted in the photoemission process are imaged using an electron optical lens system. In contrast to a scanning electron microscope, in that an electron beam is scanned over the sample surface, in PEEM the whole field of view is imaged at once. Therefore, PEEM allows for real-time image acquisition. To the same extent as for any microscopic technique, for the interpretation of the images the knowledge of the contrast mechanisms is crucial. The contrast in PEEM images results from relative differences in the electron yield in a certain field of view. That is, areas from which more electrons are emitted than from another, appear brighter in the resulting gray scale image. A basic contrast mechanism is of topographic origin. It results from a distortion of the electric field between the sample and the first lens due to topographic features. Consequently, the electron trajectories are altered, which leads to different detected intensities. An illustration of some topographic features and the resulting PEEM images is given in figure 3.6.

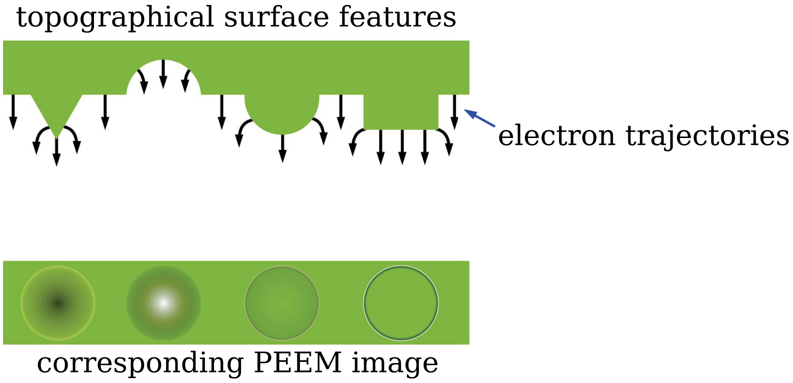

Figure 3.6: Illustration of the topographic contrast formation due to electric field inhomogeneities in photoemission electron microscopy [54].

As an electron excitation source either ultraviolet lamps or synchrotron radiation sources are employed. Sometimes the former mode is called threshold PEEM and the latter high-energy PEEM. The topographic contrast appears in both operation modes. Depending on the light source, various additional contrast mechanisms and different degrees of surface sensitivity are provided. Ultraviolet PEEM primarily provides work function contrast. Further, when applied with circularly polarized synchrotron radiation, PEEM provides a unique combination of surface sensitivity and chemical and magnetic contrast. In the following, the available contrast mechanisms in PEEM dependent on the light sources will be described in more detail.

3.3.1 Excitation with ultraviolet light

In ultraviolet photoemission electron microscopy (UV-PEEM), the photon energies are of the order of $h\nu \approx 5\,\mathrm{eV}$, which is comparable to the work function ϕ of typical samples. Due to the high IMFP at low kinetic energies, in UV-PEEM mode mostly unscattered photoelectrons are observed [74]. Therefore, in principle, only modest surface sensitivity should be achieved in UV-PEEM. Though, the dominant contrast mechanism in UV-PEEM is the work function contrast resulting from a dependence of the number of photoelectrons emitted from a certain area on the local work function. The work function is highly sensitive to the properties of the surface, as outlined below. Thus, the high surface sensitivity of UV-PEEM is resulting from the work function contrast rather than the IMFP.

To quantify the work function contrast, the number of photoelectrons, or photocurrent j for $h\nu > \phi$ can be expressed as

$$j \propto (h\nu - \phi)^x \, . \tag{3.6}$$

The exponent x is 2 for a simple metal and in the range of 1 to 5/2 for semiconductors [71]. It should be mentioned that for semiconductors the work function is in the middle of the band gap, so in fact the photoelectric threshold E_T is probed by UV-PEEM. Frequently, E_T is also referred to as work function for simplicity. Since the relative differences of the photocurrent resulting from equation 3.6 are proportional to $1/(h\nu - \phi)$, a light source whose photon energy is close to the average work function of the sample yields the highest work function contrast. An illustration of the work function contrast is given in figure 3.7. Clearly, areas with lower work function appear brighter in the UV-PEEM image.

The work function depends on the chemical and structural properties of the surface. First of all, the work function depends on the chemical element and is proportional to the electronegativity [71], at least for metals. Furthermore, the work function depends on the surface orientation, for instance the (111)-surface of an fcc-crystal has a higher work function than the (110)-surface, while for a bcc-crystal the contrary is true. Further, the work function is highly sensitive to changes in the chemical composition of a surface. For instance, carbon monoxide adsorption and surface diffusion on catalyst surfaces was intensively studied using PEEM [76]. In this work,

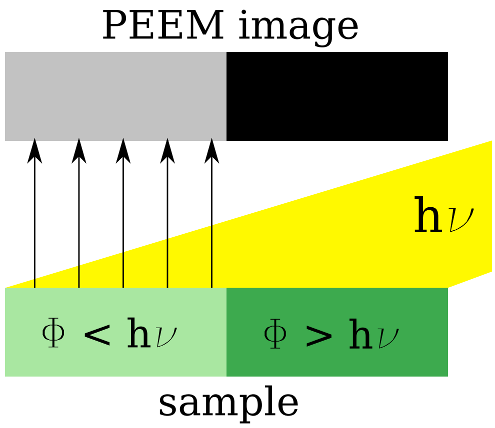

Figure 3.7: Illustration of the formation of work function contrast. Adapted from [75].

the dependence of the work function for different surface reconstructions is utilized. This allows for a precise control of the silicon carbide surface preparation process.

In summary, the work function contrast leads to a high surface sensitivity of UV-PEEM combined with chemical and structural sensitivity. Additionally, the range of applications of PEEM can be greatly enhanced with the combination with a synchrotron radiation source with tunable circular polarization as will be shown in the next section.

3.3.2 Excitation with synchrotron radiation

In x-ray photoemission electron microscopy (X-PEEM), the secondary electron yield emitted upon excitation with monochromatic synchrotron radiation is used as an electron source. The main contribution to the electron yield consists of inelastically scattered Auger electrons produced in the x-ray absorption process. The energy spread of the secondary electron peak is usually less than 5 eV in most materials [77]. To provide a good lateral resolution, chromatic aberrations must be avoided, which is achieved by a reduction of the energy width. In conventional PEEM setups, this energy selection results from the low-pass property of the electron optics that is ensured by a small aperture. Moreover, in some instruments the energy width can be controlled by the application of energy filters. As an illustration, figure 3.8 shows the part of the electron spectrum that is used for image formation. The IMFP of the electrons that are used for imaging is usually about 2–10 nm depending on the density of states at the Fermi level of the particular sample [77]. In the following, it is shown how chemical and magnetic sensitivity is enabled by the ability to tune the energy and polarization of the synchrotron radiation.

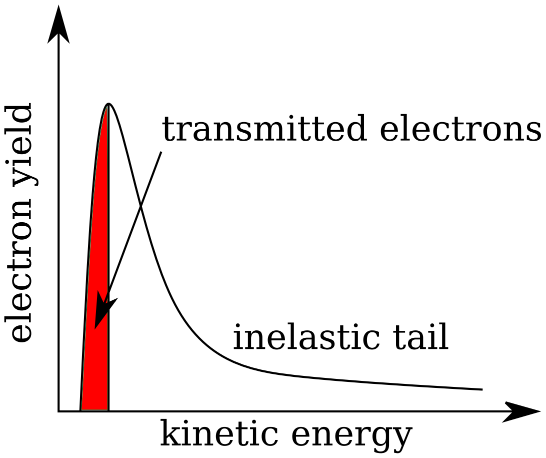

Figure 3.8: Illustration of the secondary electron yield resulting from excitation with synchrotron radiation. Only the electrons with the lowest energy are transmitted due to the low-pass property of the PEEM optics.

Chemical sensitivity

The Auger relaxation processes that follow the absorption of soft x-rays lead to a cascade of inelastic collisions and the emission of secondary electrons. This secondary electron yield is proportional to the x-ray absorption cross section [78]. The measurement of the electron yield is thus one of the possible ways to record x-ray absorption spectra (XAS), among the direct measurement of the x-ray transmission through a thin sample, or the measurement of the fluorescence yield. Consequently, photon energy-scanned X-PEEM is in fact spatially-resolved x-ray absorption spectroscopy [79]. In an XAS spectrum, the transitions of core-level electrons into unoccupied valence states give rise to characteristic absorption edges [80]. Since the core-level binding energies are element-specific, energy-scanned PEEM provides elemental sensitivity.

To record a spatially-resolved XAS spectrum, an individual PEEM image is recorded for every point in the spectrum. By choosing a region of interest in the resulting images and integration of the pixels inside, XAS spectra from distinct sample features can be acquired [81]. This acquisition of spatially-resolved XAS spectra of a sample of squares of an iron-nickel alloy (Permalloy) deposited on a silicon substrate is illustrated in figure 3.9. Therein, a single PEEM image, taken at a photon energy corresponding to the peak of the Fe L_3-edge is shown along with the spectra extracted from the areas marked in the PEEM image.

The spectra that are displayed in figure 3.9 correspond to the integrated intensity of the areas that are marked by the white and black squares in the PEEM image,

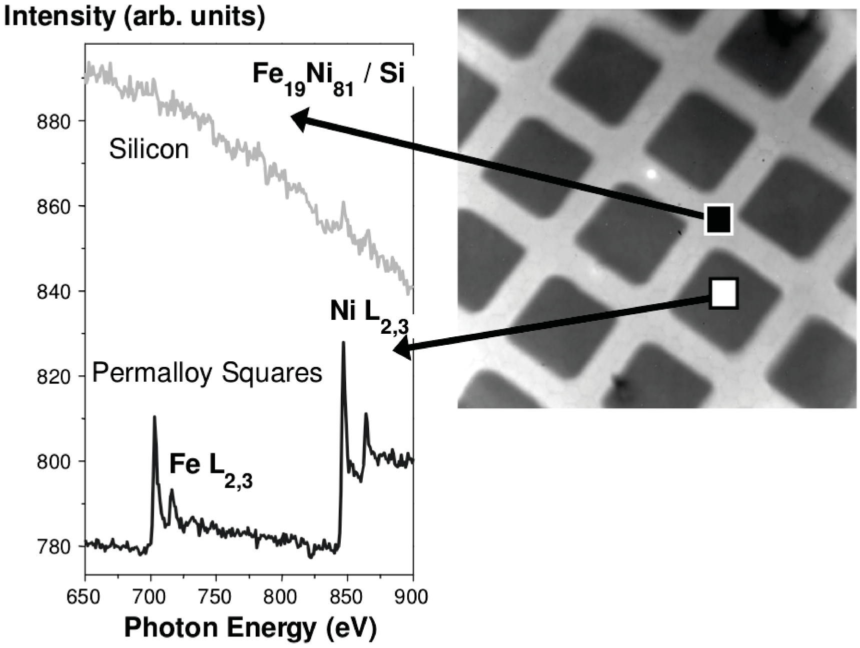

Figure 3.9: Illustration of the acquisition of spatially-resolved XAS spectra in the energy range of the L-edges of iron and nickel by means of energy-scanned PEEM [81]. The sample consists of squares of an iron-nickel alloy on a silicon substrate. The plotted spectra correspond to the areas marked by white and black squares in the PEEM image. The PEEM image was recorded at the Fe L_3-edge and its dimensions are 100 µm × 100 µm. From the spectra, the presence of iron and nickel in the dark areas in the PEEM image and their absence in the bright areas can be deduced.

respectively. The spectra recorded at the Permalloy squares clearly reveal absorption edges of iron and nickel. Conversely, the spectrum extracted from the area outside the Permalloy squares does not reveal distinct absorption edges. This is of course expected since the respective areas expose the bare silicon substrate. Note that due to the higher absolute x-ray absorption of the silicon areas, these areas appear brighter in the PEEM image though the image was recorded at the Fe L_3-edge.

To enhance the chemical contrast resulting from a single element, pairs of images recorded at the peak and a few eV below a certain absorption edge can be subtracted or divided. Since the resulting image contains only information due to the absorption peak of the specific element, it is a map of this element on the sample surface. All other contrast mechanisms are thus removed from the resulting image. Figure 3.10 displays an X-PEEM image recorded at the Ni L_3-edge and the difference image resulting from the subtraction of a background image recorded 5 eV before the Ni L_3-edge. The sample is identical to that shown in figure 3.9. Clearly, the bright areas in figure 3.10 (b) correspond to the Permalloy-covered areas whereas the uncovered areas appear dark.

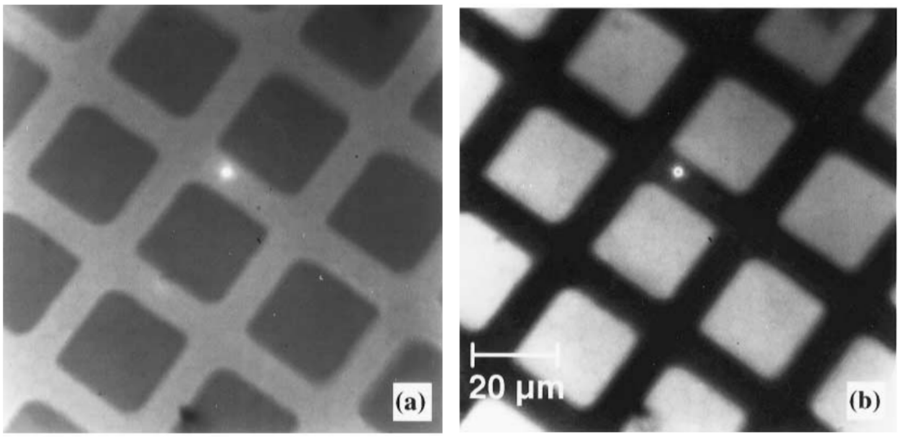

Figure 3.10: (a) X-PEEM image recorded at the Ni L_3-edge. (b) Difference image of that shown in (a) and an X-PEEM image recorded 5 eV before the Ni L_3-edge [81].

Magnetic sensitivity

The X-PEEM technique further provides magnetic sensitivity due to the application of the x-ray magnetic circular dichroism (XMCD) effect [82]. The XMCD effect is a consequence of the dependence of the x-ray absorption cross-section on the polarization of the x-rays. In particular, the relative orientation of the photon polarization of circularly polarized x-rays and the magnetization of the sample determines the absorption strength [83]. The effect is greatest in the vicinity of the x-ray absorption edges. Due to the element-specificity of the absorption edges, XMCD enables element-specific magnetic imaging within the X-PEEM method, which is unique among the surface sensitive microscopic techniques. As an illustration of the effect, figure 3.11 (b) shows XAS spectra of the Fe L_3-edge in iron metal for parallel, anti-parallel, and perpendicular alignment of the photon polarization vector and the magnetization of the sample. In essence, for parallel alignment, the x-ray absorption is higher than for anti-parallel alignment. Consequently, the magnetization direction can be determined by the difference of spectra taken with opposite polarization.

The XMCD effect can be understood in the framework of the band model of ferromagnetism. As stated in section 2.2.2, the net magnetic moment in a ferromagnetic material arises from an imbalance in occupation of the valence state depending on the spin. For simplicity, one may assume that one spin channel is fully filled and

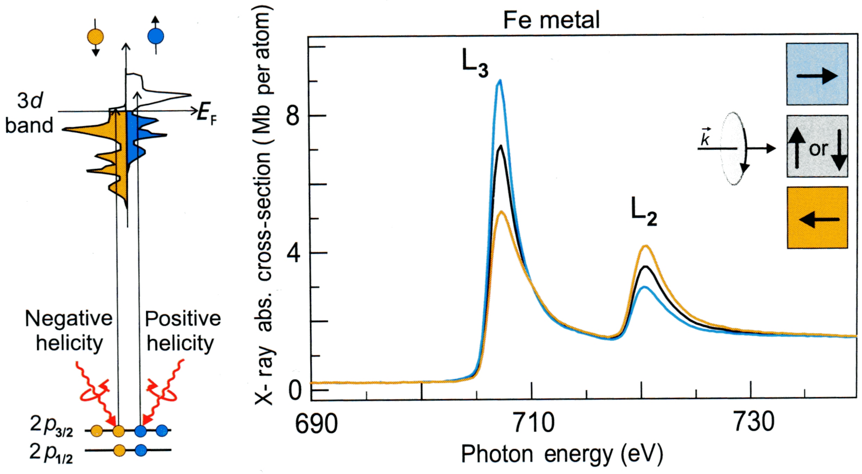

(a) (b)

Figure 3.11: The x-ray magnetic circular dichroism effect. (a) Polarization-dependent absorption process due to the spin-split band structure of 3d ferromagnets (b) Fe L-edge spectra of an iron sample recorded with left and right circular and un-polarized light [52].

therefore only electrons of the other spin can be added, as sketched in figure 3.11 (a). Thus, the unoccupied states are completely spin-polarized. On the other hand, the XAS intensity near the absorption edge is proportional to the number of unoccupied states above the Fermi level. Consequently, the spin-polarized unoccupied states can be probed by excitation of core-level electrons with circularly polarized light, as illustrated in figure 3.11 (a). During the x-ray absorption process, the angular momentum of the photon is transferred to the core electron, due to the conservation of the angular momentum [52]. As a result, the electron gains orbital momentum that gives rise to a spin-polarization due to the spin-orbit coupling. Since final states are only available for one specific spin orientation, the transition probability of this absorption process ultimately depends on the polarization of the light.

The strength of the effect is described by the XMCD intensity

$$I_{\text{XMCD}} \propto P_{\text{circ}} \langle \vec{m} \rangle \cos\theta, \tag{3.7}$$

which depends on the degree of circular polarization P_{circ}, the magnetization $\langle \vec{m} \rangle$ of the sample, and the angle between the incidence of the light and the magnetization θ. For the room-temperature ferromagnets iron, cobalt, and nickel, the largest XMCD intensity is expected at the L-edges, since they involve transitions from the 2p to the 3d states, which are responsible for the net magnetic moment.

As a result of the XMCD effect, those sample areas with different magnetization directions result in a different electron yield for a given photon polarization. This is the origin of magnetic contrast in PEEM images. Figure 3.12 displays two PEEM images of a magnetic sample taken with opposite photon helicity and a calculated imaged with enhanced contrast. The contrast enhancement is achieved by calculation of the asymmetry image that is defined by

$$A = \frac{I(\sigma^+) - I(\sigma^-)}{I(\sigma^+) + I(\sigma^-)}, \tag{3.8}$$

with the intensities $I(\sigma^+)$ and $I(\sigma^-)$ corresponding to images taken with positive and negative circular polarization, respectively. Another method is the calculation of the ratio image $R = I(\sigma^+)/I(\sigma^-)$, which is an approximation of the asymmetry image for small dichroism [84]. For each image calculation operation, a correction for the inevitably occurring thermal sample drift must be applied. Consequently, in practice, the ratio image is often preferred since it involves only one operation instead of three. It is completely sufficient to observe the shape of the magnetic domains and to determine the number of magnetic easy-axes.

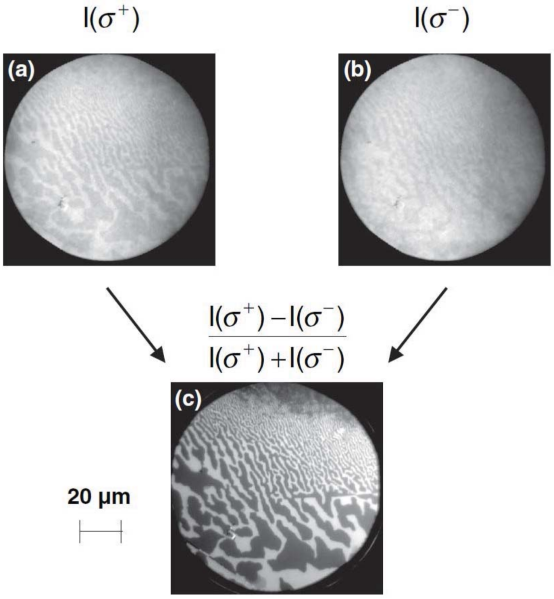

Figure 3.12: Enhancement of the magnetic contrast by calculation of the asymmetry image (c) from images acquired with opposite photon helicity (a) and (b) [85].

3.4 Low-energy electron diffraction

Low-energy electron diffraction (LEED) is an immediate probe of the reciprocal lattice of the surface, therefore it provides one of the most important techniques in surface science. Different to the methods discussed in the previous sections, LEED is an "electron in – electron out" technique, instead of "photon in – electron out". The diffraction pattern is solely formed by elastically scattered electrons [51], hence the information depth is determined by the IMFP of the electrons. One of the main applications of LEED is the evaluation of successful surface preparation, due to its high surface sensitivity to only a few atomic layers. Moreover, a frequent application is the determination of the periodicity of reconstructions and adsorbate structures. Historically, electron diffraction at surfaces was the first proof for the wave-like nature of matter [86]. De Broglie predicted the wavelength associated with a particle flux

$$\lambda = h/mv, \tag{3.9}$$

with the Planck constant h, the particle mass m, and the particle velocity v. Consequently, the wavelength of electrons with the kinetic energy E_{kin} is

$$\lambda = \frac{h}{\sqrt{2mE_{\text{kin}}}}. \tag{3.10}$$

With typical values of $\lambda \approx 1$–$3\,\text{Å}$ for $E_{\text{kin}} = 20$–$150\,\text{eV}$, low-energy electrons are well-suited to resolve the periodicities of clean surfaces and superstructures.

Constructive interference is predicted by the two-dimensional Laue condition

$$\vec{k}_{||} - \vec{k}_{0||} = \vec{G}_{||}, \tag{3.11}$$

with the diffracted electron wave vector $\vec{k}_{||}$, the incident electron wave vector $\vec{k}_{0||}$, and a vector $\vec{G}_{||}$ of the reciprocal lattice. Similar to the three-dimensional case, the Ewald construction illustrates the Laue conditions [57]. Figure 3.13 depicts the Ewald construction along a line in the two-dimensional reciprocal lattice.

A sphere with radius k is drawn intersecting the origin of the reciprocal lattice (00). Due to the broken symmetry at the surface in z-direction, the reciprocal lattice points are degenerate into rods. Constructive interference occurs for each intersection of the sphere with a reciprocal lattice rod. The vector $\vec{k}$ then defines the direction of the diffracted beam. Since $\lambda = 2\pi/k$, the radius of the sphere depends on the wavelength. Therefore, for the same $\vec{G}_{||}$ the angle between incident and diffracted beam is proportional to λ. The (00) spot is the direct reflection of the electron beam therefore its position is fixed and in a LEED experiment the remaining spots move towards the (00) spot upon increase of E_{kin}.

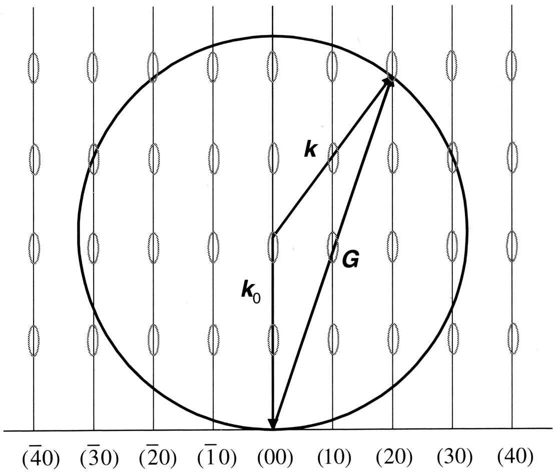

Figure 3.13: Ewald construction along a line in the reciprocal lattice for the two-dimensional case [57]. $\boldsymbol{k}$, $\boldsymbol{k}_0$, and $\boldsymbol{G}$ denote the diffracted electron wave vector, the incident electron wave vector, and a vector of the reciprocal lattice, respectively.

The diffraction pattern of reconstructions or superstructures offers direct access to the Brillouin zone of the reciprocal lattice, allowing a direct determination of the real space periodicity of the unit cell. Superstructures are most often classified by means of the Wood notation. An example for a superstructure in Wood notation is $\left(\sqrt{3} \times \sqrt{3}\right)$-R30°. In this example, the real space vectors of the reconstructed surface posses a length of $\sqrt{3}$ of that of the unreconstructed surface. Moreover, the unit cell of the superstructure is rotated by an angle of 30° to the substrate.

It remains to mention that the relative positions of the superstructure atoms with respect to the substrate remain undetermined. This information is contained in the intensities of the diffraction spots that can be predicted by scattering theory [86].

4 Experimental setup

This chapter focuses on the instrumentation that was used for the acquisition of the data that are presented in this thesis. First, the necessity of ultra-high vacuum (UHV) is motivated. In the subsequent sections, the preparation of the silicon carbide samples and the cobalt films is discussed. Afterwards, the different light sources that were used for the photoemission experiments are described. The analytical equipment at the different experimental stations is introduced in the final section.

4.1 The need for ultra-high vacuum

The measurements carried out in this work are surface sensitive, therefore the quality of the sample surface must be preserved during the analysis process. To ensure that the surface is not contaminated by foreign atoms, the cobalt film preparation and all measurements are performed in UHV chambers. As an exception, the SiC sample preparation is carried out in inert gas atmosphere. Besides the preservation of the sample surface, good vacuum conditions are also a prerequisite for electron-based measurements. This results from the fact that low-energy electrons possess only a negligible mean free path at atmospheric pressures. The same applies for synchrotron radiation in the soft x-ray regime. Conventionally, UHV is defined as a pressure below 1×10^{-8} mbar.

In the following, the necessity of UHV for the preservation of the sample quality is exemplified. According to the kinetic gas theory, the rate of gas molecules impinging on a surface per time and unit area is

$$I = \frac{p}{\sqrt{2\pi m k_{\mathrm{B}} T}}, \tag{4.1}$$

with the pressure p, the molecular mass m, the Boltzmann constant k_{B}, and the absolute temperature T. Assuming a molecular density in a monolayer of nitrogen of $10^{19}\ \mathrm{m}^{-2}$, at room temperature and $p = 1 \times 10^{-9}$ mbar, one nitrogen monolayer is formed in approximately one hour if every molecule that impinges the surface is adsorbed [68]. Since this is a typical time required for one measurement, it therefore becomes clear that $p \approx 1 \times 10^{-9}$ mbar is required in order to preserve the sample surface during the measurement process.

Note that the so-called sticking coefficient that is a measure for the adsorption probability, might be well below 1 in the case of inert substrates and can be further reduced by an increased sample temperature. Further, it should be mentioned that the relevant physical quantity is the partial pressure of reactive species. At absolute pressures in the 10^{-9} mbar regime, the residual gas usually mainly consists of hydrogen molecules, due to the different pumping characteristics depending on the molecular mass. The partial pressure of possible contaminants like oxygen is then orders of magnitude lower.

To minimize the pumping time after exposure of the vacuum system to the atmosphere, the whole vacuum chamber is heated up to temperatures of about 180 °C during the evacuation process. This so-called bake-out process is maintained for at least several hours. As a consequence, the vapor pressure of adsorbates on the walls of the vacuum chamber greatly increases, so they desorb and can be captured by the vacuum pumps. The particular maximum temperature depends on the thermal resilience of the components attached to the vacuum chamber and must be carefully chosen to avoid potential damages to the equipment.

4.2 Sample preparation

4.2.1 Silicon carbide

The silicon carbide sample preparation was carried out in a high vacuum chamber equipped with an induction heating system that allows annealing up to a temperature of $T \approx 1500\,^\circ\mathrm{C}$ in vacuum or inert gas. Figure 4.1 displays a photograph of the setup. The vacuum system consists of a turbo-molecular pump backed by a membrane pump, providing a base pressure of 2×10^{-8} mbar after 16 h pumping without bake-out. Automatic gate and leak valves as well as the remote-controlled power supply allow the automation of the whole preparation procedure. It is operated by a micro-controller system (Arduino) that is described in detail in reference [87]. The sample is inserted in a graphite crucible (CTG GmbH) that is surrounded by a water-cooled copper coil through which an alternating current flows. The diameter, height, and wall thickness of the crucible are $d_\mathrm{C} = 20\,\mathrm{mm}$, $h = 18\,\mathrm{mm}$, and $t = 4\,\mathrm{mm}$, respectively. Inside the crucible walls, eddy currents are induced that lead to heat production due to the electrical resistance of the graphite. An illustration of the crucible and the surrounding area of the setup is shown in figure 4.2.

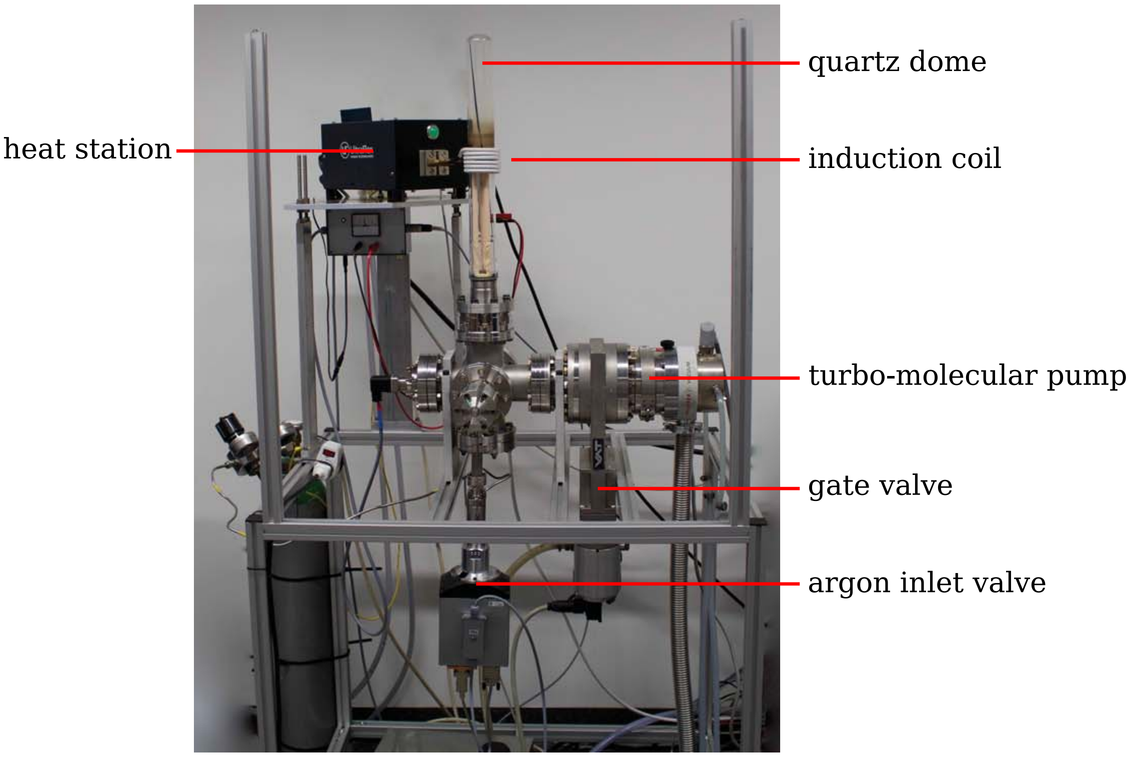

Figure 4.1: Photograph of the vacuum chamber that was used for the induction heating of the silicon carbide samples.

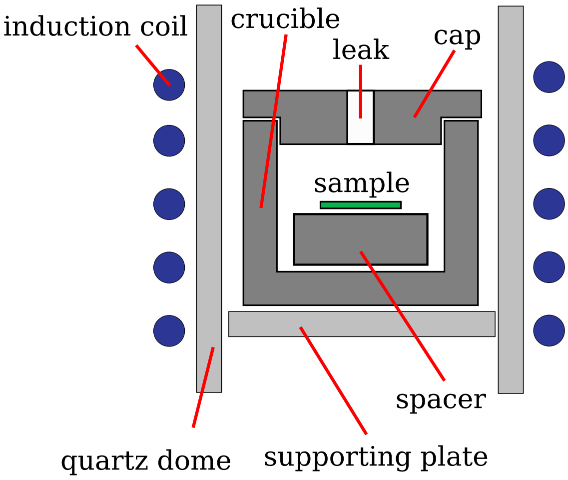

Figure 4.2: Sketch of the crucible and the surrounding area within the induction coil.

In order to ensure that only the crucible is heated by induction, every other material used for supporting structures and the vacuum chamber must be electrically insulating. Furthermore, the materials used must withstand the high temperature of the heated crucible. The vacuum chamber around the crucible is therefore made of a quartz dome. Only a limited amount of the heat radiated off the crucible is absorbed by the quartz and no direct contact of the crucible and the quartz dome occurs. Thus, the temperature of the crucible can exceed the recommended maximum operating temperature of quartz which amounts to about 1000–1200 °C.

The crucible is supported by a construction made from aluminum oxide, which is insulating and endures temperatures up to 1700 °C. Briefly, the construction consists of three aluminum oxide rods with a circular support plate on which the crucible is positioned. By means of these rods it is ensured that the crucible is positioned approximately in the center of the quartz dome. The whole construction is described in detail in reference [88]. As depicted in figure 4.2, the supporting plate and the crucible are in direct physical contact. After several preparation cycles at high temperature, a chemical reaction of the crucible and the supporting plate resulting in the release of small amounts of free aluminum was observed. This effect is enhanced if the annealing is carried out in vacuum instead of inert gas. While some samples contained trace amounts of aluminum, no effect on the measurements could be recognized. However, a substitute for the crucible supporting plate made from binder-free hexagonal boron nitride (P100, Henze BNP) was tested and proven appropriate.

To control the silicon flux, the crucible is equipped with a cap possessing a defined bore with the diameter $d_\mathrm{B} = 1\,\mathrm{mm}$. Since the evaporated silicon atoms can only escape the crucible through this small leak, the silicon partial pressure surrounding the sample is increased, which significantly reduces the graphene growth rate [18]. Notably, the growth rate reduces to a steady state during the first growth cycles carried out with a new crucible, since evaporated silicon atoms adsorb on the fresh graphite surfaces. Therefore, during the initial growth cycles the partial silicon pressure surrounding the sample is reduced and conversely the silicon desorption rate at the sample is effectively increased. Thus, new graphite crucibles must be passivated in order to provide a reproducible sample preparation. Typically, passivisation is naturally achieved after about 10 preparation cycles.

Another parameter that influences the graphene growth rate is the temperature gradient at the sample surface. It has been revealed that the growth rate is significantly higher at the edges than at the center of samples that were positioned directly on the bottom of the crucible. This results from a lower temperature at the bottom which is only indirectly heated by thermal conduction from the walls. Therefore, to reduce the temperature gradient at the sample surface, the sample is positioned on top of a graphite spacer that increases the distance from the bottom, as displayed in figure 4.2. A spacer with diameter $d_\mathrm{S} = 11.5\,\mathrm{mm}$ and height $h_\mathrm{S} = 4.6\,\mathrm{mm}$ was chosen in order to position the sample in the center of the crucible.

The electronics of the induction heating system consist of a so-called heat station and a power supply. The heat station (HS-4, Ultraflex), which is visible in figure 4.1, is a resonant circuit consisting of the induction coil as inductivity L, the so-called tank capacitor C, and the crucible as the resistance R. Furthermore, the heat station contains a transformer with a changeable transformation ratio, whose optimal value depends on the actual load used. The power supply (UPT-S2, Ultraflex) provides an alternating current at a variable frequency f, determined by the values of L and C, to the heat station. The power supply is regulated in percents of the maximum output power that amounts to 2 kW. In this particular setup, the maximum output power leads to a maximum temperature of $\approx 1500\,^\circ\mathrm{C}$. Due to the enclosure of the sample inside the crucible, a direct measurement of the sample temperature is not possible. Rather, the temperature of the outer crucible wall is used as a reference. It was checked by an optical pyrometer (PV 11, Keller) with the emissivity set to 83 %. The particular temperature values that were used for the sample preparation process are discussed in section 5.1.

The setup described here operates at the frequency $f = 77\,\mathrm{kHz}$. The choice of the frequency determines the efficiency that is defined as the power absorbed in the crucible compared with that absorbed in the coil. This relation results from the skin effect that allows the magnetic field H of the coil to penetrate the crucible only to a limited extent. The characteristic length scale is the skin depth $\delta = \sqrt{\rho/\mu f}$, which denotes the depth after which H decreased to $1/e$ of its original value. For a given f, the load must exceed a minimum diameter d, otherwise the net eddy currents are reduced due to cancellation effects. The actual efficiency depends of the ratio d/δ that is optimal for $d/\delta \geq 4.5$ in the case of a solid rod [89]. Below this value the efficiency reduces rapidly, whereas it saturates for higher values. Assuming a specific resistivity of graphite of $\rho = 7.5 \times 10^{-6}\,\Omega\,\mathrm{m}$ [90], $d/\delta = 2.3$ for $f = 77\,\mathrm{kHz}$ and $d = 20\,\mathrm{mm}$. It should be mentioned that the precise value of the resistivity of the crucible used here is unknown as it depends strongly on the microscopic structure since graphite is highly anisotropic. The precise value of the optimal d/δ value depends on the shape of the load and in the case of a crucible, the wall thickness becomes a further important parameter.

4.2.2 Cobalt films

The cobalt films were deposited on the silicon carbide samples by means of electron beam evaporators. This type of evaporator heats the evaporant by electron impact up to a material-specific temperature leading to a sufficient vapor pressure. A collimator focuses the evaporated atoms such that a spot with a typical diameter of about 10 mm is achieved at the sample position. In this work, single and triple evaporators (EFM 3 / EFM 3T, Focus GmbH) were used. Both models utilize the same principle but the latter additionally allows the simultaneous usage of three different evaporants.

Figure 4.3 displays a photograph of a single evaporator together with a sketch of the interior of the cooling shroud that contains the evaporant. During evaporation, the cooling shroud is permanently provided with a water flow to minimize the pressure rise in the vacuum chamber due to heat-induced desorption from the surrounding surfaces. The evaporator is based on a CF35 flange that contains all necessary feedthroughs for the filament voltage, the high voltage, the cooling water and the shutter actuator. At the central feedthrough that is to be connected to a high-voltage power supply, a rod is mounted that is inserted in the copper cylinder by means of a insulated slide bearing. The evaporant material is attached to this rod using a barrel connector, as displayed in the sketch in figure 4.3.

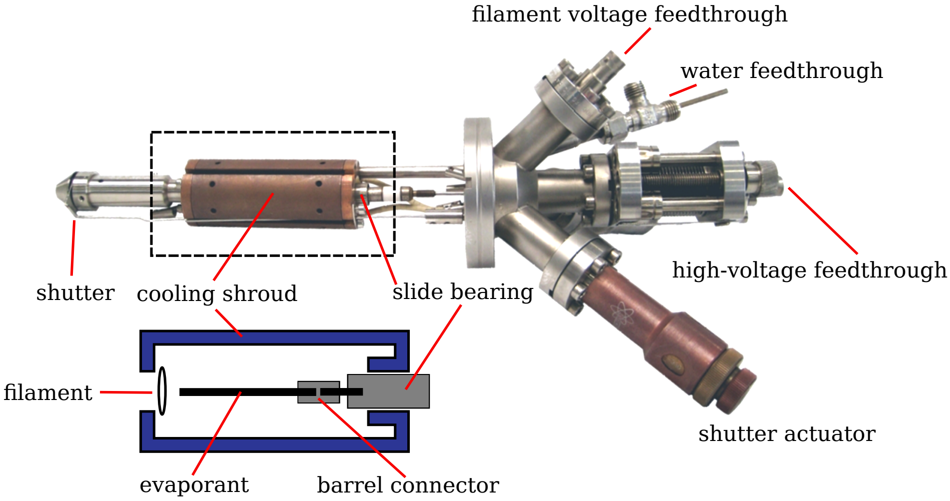

Figure 4.3: Photograph of an electron beam evaporator identical to that used in this thesis and illustration of the interior of the copper cooling shroud. Photograph taken from [91].

The heating is enabled by electrons emitted from a heated filament that are accelerated towards the evaporant as a result of the high-voltage U_{HV} applied between the filament and the evaporant. The electron impact leads to an increase of the temperature of the evaporant, with an estimated heating power of $P = U_{\mathrm{HV}} \times I_{\mathrm{em}}$, where I_{em} denotes the emission current provided by the high-voltage power supply. The shutter allows a pre-heating and degassing of the evaporant with the sample already in front of the evaporator before the actual deposition is started by opening the shutter.

The evaporant material can be either made from a solid rod that is directly attached to the high-voltage carrying rod, or it can be inserted into a crucible. The choice is made depending on the mechanical stability of the evaporant material at the necessary temperature for a sufficient vapor pressure. When appropriate, evaporation from rods is favorable because it leads to a lower radiative heat losses due to a small heated surface and the absence of the risk of crucible-induced impurities. Since cobalt possesses a sufficient vapor pressure below its melting point and it remains mechanically stable at elevated temperature, the evaporant can be made from a thin rod in this case.

4.3 Light sources

Three different light sources were used for the experiments described in this thesis. A mercury short-arc lamp was employed in order to perform UV-PEEM experiments independent of the availability of beam time at a synchrotron radiation source. For the XPS and X-PEEM experiments, the synchrotron radiation sources DELTA and SPring-8 were used, which are located in Dortmund, Germany and Hyōgo Prefecture, Japan, respectively.

4.3.1 Mercury short-arc lamp

For the UV-PEEM experiment at the TU Dortmund, a mercury short arc lamp (HBO 100 W/2, Osram) was used. The lamp bulb is filled with a mixture of argon and xenon gas and a small amount of liquid mercury. High-voltage pulses start a gas discharge between two tungsten electrodes, whose small distance of some mm accounts for the term short-arc lamp. Due to the discharge that is maintained by a direct current, the temperature of gas increases leading to the evaporation of the mercury. Shortly after ignition, the spectrum consists only of the lines of the inert gas, while upon warming the mercury lines emerge as well. They totally suppress the inert gas lines after warm up is completed within a few minutes. The resulting light is unpolarized and consists of several lines with photon energies up to $h\nu = 4.9\,\mathrm{eV}$ [92], which is a value close to the photoelectric work function of most samples. The pressure inside the bulb increases up to several atmospheres due to the evaporated mercury, which makes an appropriate lamp housing mandatory. The housing used here (PTI, Inc.) additionally allows for the focusing of the ultraviolet beam to a spot size of 3–4 mm.

4.3.2 Synchrotron radiation sources

Synchrotron radiation sources make use of the radiation emitted by accelerated electric charges. In an electron storage ring, synchrotron radiation is generated whenever the electron beam is deflected from its straight path. The radiation is generated as a by-product in the bending magnets that are necessary to keep the electron beam inside the storage ring, as well as in dedicated so-called insertion devices, such as undulators or wigglers. After generation, the synchrotron radiation is monochromatized and focused in beamlines that are adapted for the particular requirements of the individual experimental end-stations. Two separate beamlines have been used for the experiments described in this work.

For the XPS experiment, the plane-grating-monochromator beamline 11 located at DELTA was used. The radiation source is the permanent magnet undulator U55. It consists of an alternating pattern of magnetic north and south poles that force the electrons on a sinusoidal path, leading to a linear polarization in the beam plane. The beamline provides photon energies of $h\nu = 55$–$1500\,\mathrm{eV}$ and an energy resolution of $E/\mathit{\Delta}E = 10000$ that can be achieved throughout the energy range. The spot size at the sample is $70\,\mu\mathrm{m} \times 30\,\mu\mathrm{m}$ and a typical flux at $h\nu = 400\,\mathrm{eV}$ and $E/\mathit{\Delta}E = 2000$ is 4×10^{12} photons/s [93].

The beamline BL17SU at SPring-8, Japan was used for the X-PEEM experiment. The electromagnetic circular undulator forces the electrons on an elliptical trajectory and therefore provides circular polarization, which enables the exploitation of the x-ray magnetic circular dichroism. The degree of circular polarization depends on the photon energy [94]. The beamline provides photon energies of the range of 200–1800 eV with a typical flux of 2×10^{11} photons/s [95]. Throughout the range 400–1000 eV the energy resolution is $E\ /\ \mathit{\Delta}E = 10000$. The spot size at the sample is $14\,\mu\mathrm{m} \times 3\,\mu\mathrm{m}$ [96], which is beneficial for PEEM imaging with a small field of view and high brightness.

4.4 Analytical equipment

Three distinct experimental setups were used for sample analysis. These are a laboratory-based UV-PEEM located at the TU Dortmund, the XPS end-station at beamline 11, DELTA, and the SPELEEM experiment at beamline BL17SU, SPring-8.

4.4.1 PEEM at TU Dortmund

For the UV-PEEM experiments, an electrostatic PEEM optics was used (PEEM 350-20, STAIB Instrumente GmbH). This setup provides work function and topographic contrast with a lateral resolution of 0.2 µm [97]. The lens system depicted in figure 4.4 consists of the objective lens, the intermediate lens, and two projective lenses. They are responsible for the focusing, the magnification, and for the diameter of the projected image, respectively. Between the sample at ground potential and the first lens, the transfer voltage $U_\mathrm{T} \leq 15\,\mathrm{kV}$ is applied. All lenses consist of three electrodes whose potentials are fixed at U_T for the outer two. The central potential can be adjusted in the range from ground up to U_T in order to modify the focal point of the individual lens. After passing the lens column, the electron optical image is intensified by means of a micro-channel plate and converted into a light optical image by a phosphorous screen. Finally, a CCD camera (pixelfly QE, PCO) connected with a personal computer is used for digitization of the images. The microscope is operated with the mercury short arc lamp described in section 4.3.1, whose light incidences the sample at an angle of 30°.

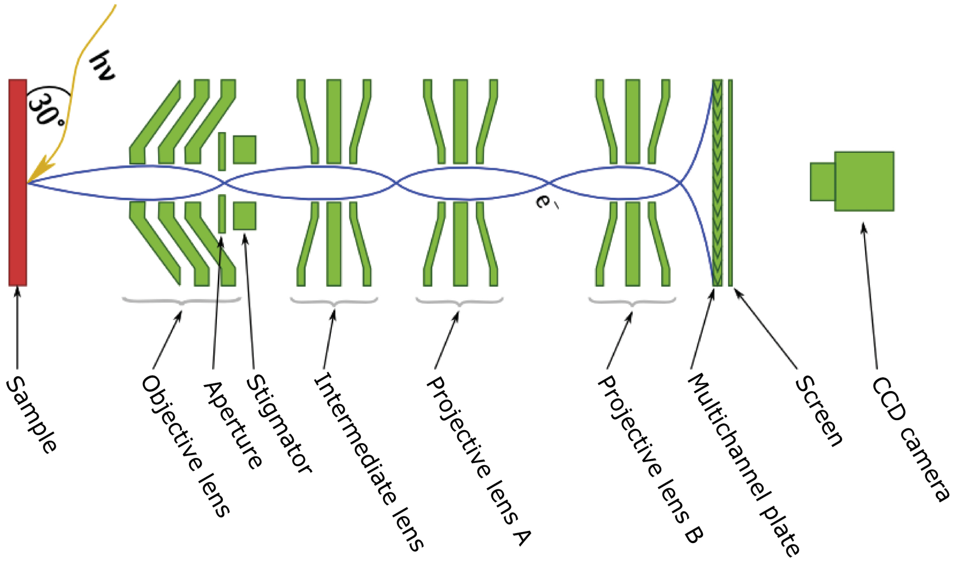

Figure 4.4: The electrostatic lens system of the PEEM 350-20. Figure extracted from [97].

The vacuum system of the PEEM apparatus, which is depicted in figure 4.5, consists of the analysis chamber, a preparation chamber, and a load-lock. The analysis chamber is pumped by an ion pump and a turbo molecular pump backed by a scroll pump. Together with a newly constructed titanium sublimation pump, the pumping system provides a base pressure of 1×10^{-10} mbar. During imaging, all

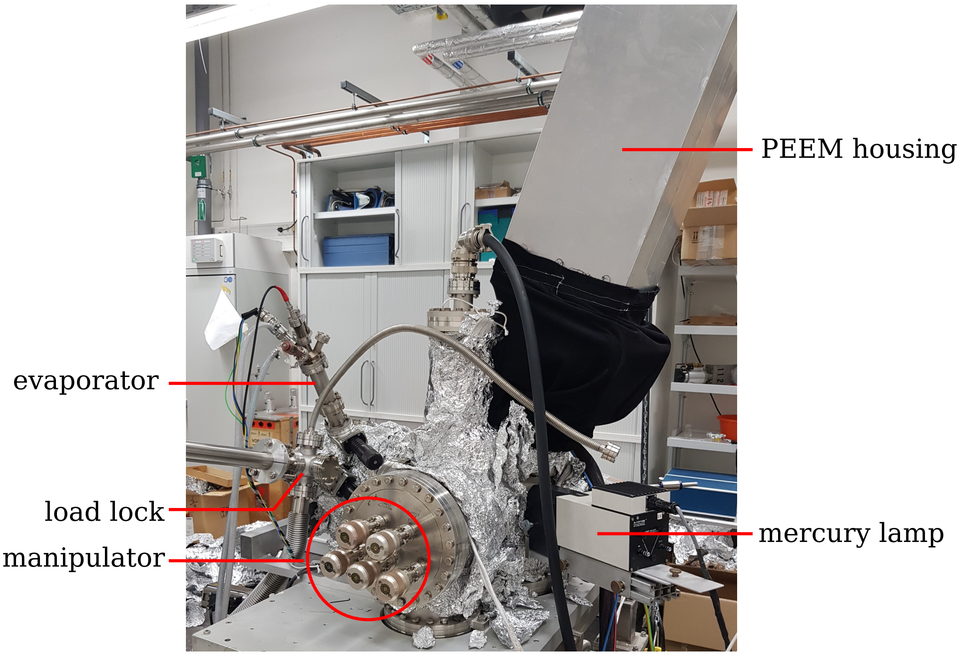

Figure 4.5: Photograph of the vacuum chamber containing the photoemission electron microscopy and the sample preparation chamber.

mechanical pumps are shut down in order to improve the lateral resolution by minimizing vibrations. To minimize stray light, the whole microscope column and the camera are enclosed by an aluminum housing. The system is equipped with a five axis manipulator allowing for the rotation of the sample around its normal, tilting the sample towards the microscope column, and translation in the three spatial directions. Sample annealing is carried out by means of thermal radiation or electron bombardment enabled by a filament mounted inside the sample holder. The electrical contact of the sample holder and the manipulator head is achieved by a screw joint that can be tightened and released in-situ by means of a magnetically coupled rotary/linear feedthrough. A photograph of the sample holder is displayed in figure 4.6.

The construction of the sample holder and the heating is explained in detail in reference [98]. The sample temperature was checked by means of an optical pyrometer (IGA 6/23 Lumasense), calibrated by a type K thermocouple clamped on the top of the sample holder.

The preparation chamber is pumped by a turbo molecular pump leading to a base pressure of 2×10^{-9} mbar. In this chamber, the deposition of the cobalt films was carried out by means of the electron beam evaporator described in section 4.2.2. Since in the original setup, the preparation chamber had to be vented and subsequently

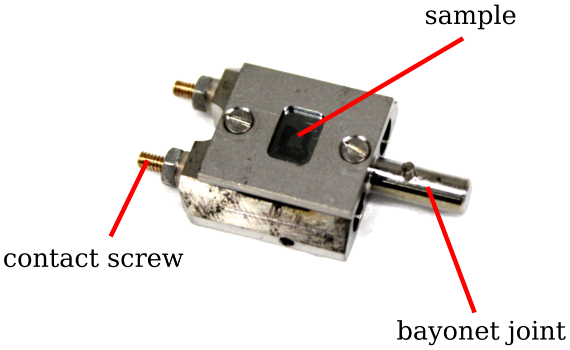

Figure 4.6: The sample holder used for the UV-PEEM experiment.

baked-out for each sample exchange, a separately pumped load-lock was constructed and attached to the preparation chamber in order to accelerate the sample exchange process. The sample transfer between the three individual chambers is carried out by means of two magnetically-coupled transfer rods mounted at the preparation chamber. The connection of the transfer-rod heads and the sample holder is carried out by the bayonet joint depicted in figure 4.6.

4.4.2 XPS at DELTA

The XPS experiments were carried out at the beamline BL11 at the synchrotron radiation source DELTA using an electron spectrometer with spherical sector analyzer (CLAM IV, VG Microtech). Spherical sector analyzers with sector angles $\alpha < 180°$ are the generalized form of hemispherical analyzers with $\alpha = 180°$[99, 100], which are typically referred to in the literature as an introductory example [62, 101]. Figure 4.7 schematically displays the internal structure of the electron spectrometer consisting of the lens system, the spherical sector analyzer, and the detector. The figure displays a cut through the symmetry axis of the analyzer. Besides a moderate magnification or demagnification, the main purpose of the lens system is to provide enough space in front of the sample. After the lens system and prior to entering the analyzer, the electrons are decelerated by a retarding potential. It is scanned over the desired energy range and therefore provides the energy selection of the spectrometer. After traversing the lens, the electron beam enters the analyzer.

The analyzer is a part of a spherical condenser consisting of two spherical sectors with a gap in between. The sector angle is $\alpha = 165°$, the mean radius $R_0 = 150\,\text{mm}$, and the gap between inner and outer spherical sector is 74 mm. Inside the analyzer, the trajectories for electrons with normal incidence angle but slightly deviating kinetic energies are shown. It should be mentioned that the analyzer in addition

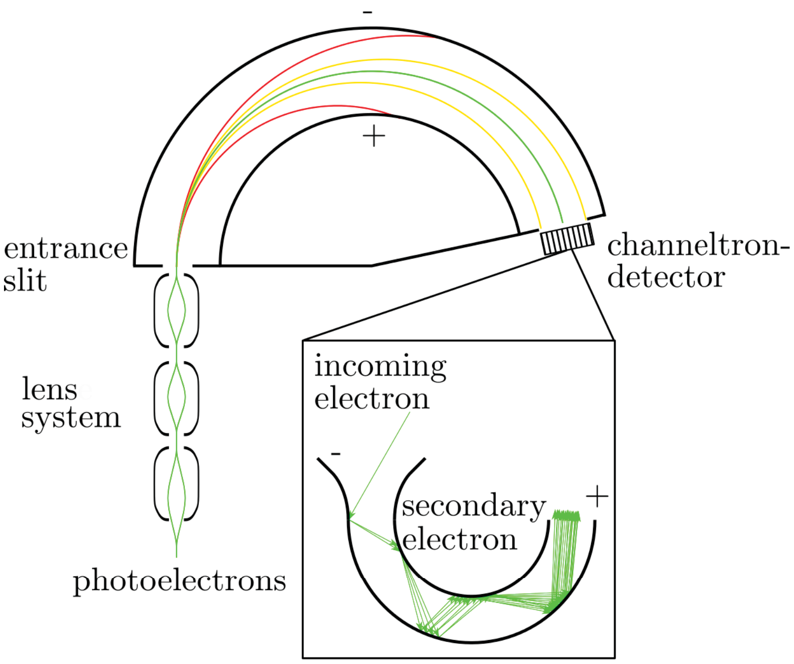

Figure 4.7: Illustration of the CLAM IV electron spectrometer [102].

has focusing properties for electrons entering at angles deviating from the normal direction. The trajectory of electrons with E_{kin} equal to the so-called pass energy E_{p} is circular with the radius $r = R_0$, whereas electrons with $E_{\mathrm{kin}} > E_{\mathrm{p}}$ or $E_{\mathrm{kin}} < E_{\mathrm{p}}$ describe trajectories with $r > R_0$ or $r < R_0$, respectively. Since only electrons with $E_{\mathrm{kin}} \approx E_{\mathrm{p}}$ are able to traverse the exit slit, the analyzer works as a narrow band pass filter. After traversing the analyzer, the number of electrons is counted by the detector, which consists of nine channeltrons that intensify the electron count by orders of magnitude.

The spectrometer is mounted at a UHV apparatus consisting of a main chamber and a load-lock. Figure 4.8 displays a technical drawing of the setup. The main chamber is pumped by a turbomolecular pump backed by a scroll pump and a titanium sublimation pump, providing a base pressure better than 1×10^{-10} mbar. The chamber is equipped with a five-axis manipulator of which the vertical translation as well as the rotation of the azimuthal and polar angles of the sample are controlled by stepper motors. The two horizontal axes can be manually controlled to align the sample in the center of the synchrotron radiation beam. Two distinct vertical levels exist of which the upper level is the analysis level and the lower is the sample transfer level. At the analysis level, the electron spectrometer, the entrance flange for the synchrotron radiation, a LEED system, and a triple evaporator (EFM 3T) reside. The manipulator head is equipped with a built-in screw that is connected with the base of the sample holder that contains a threaded hole. To tighten and loosen this connection within the vacuum chamber a linear/rotary feedthrough at sample transfer level can be used.

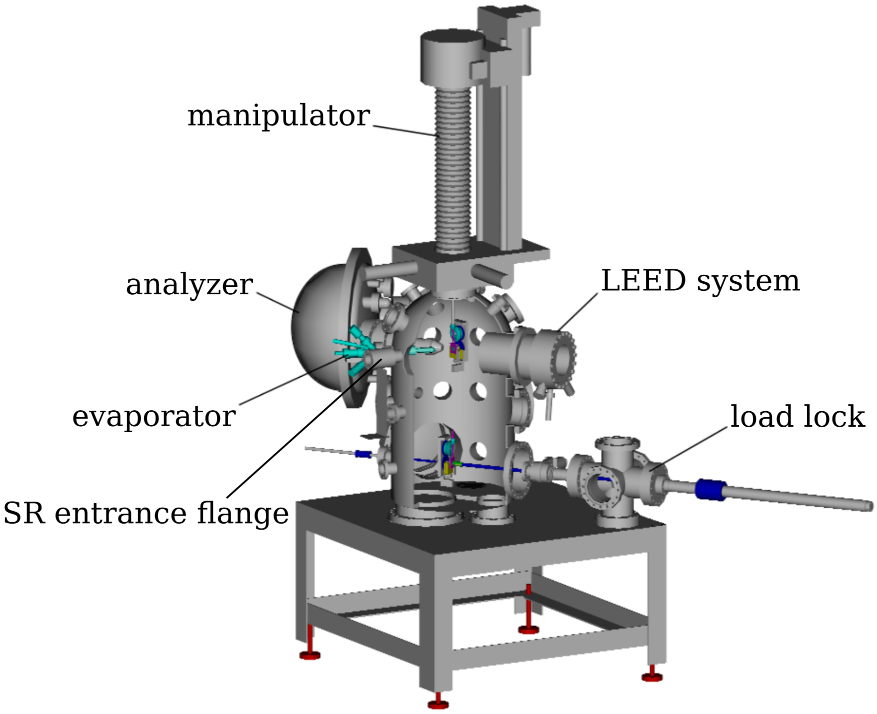

Figure 4.8: Technical drawing of the experimental end-station at BL11, DELTA [103].

The sample holder used for this experiment is displayed in figure 4.9. Due to its cylindrical shape, the sample holder enables a continuous rotation of the sample around its surface normal. The continuous electrical connection throughout the rotation is ensured by three copper rings that are connected with slide contacts installed in the manipulator head. It should be mentioned that the third copper ring is not ultimately required for this particular sample holder. However, it can be used to provide a high voltage for the implementation of an electron bombardment heating inside the sample holder, for instance. The sample is mounted at the sample holder by means of two half-shells, which are connected to one or two copper rings, respectively. The sample can be annealed by means of direct resistive heating. Since solely the sample is directly heated, the thermally-induced desorption from the surrounding surfaces is minimized. Therefore, this method allows for very high sample temperatures with a minimal associated pressure rise. During annealing, the sample temperature is checked by means of an optical pyrometer (IGA 6/23, Lumasense). All XPS measurements were carried out at room temperature.

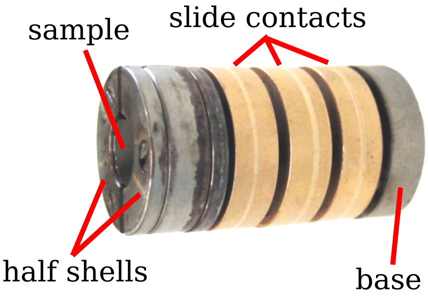

Figure 4.9: The sample holder used for the XPS experiment. The photograph was taken from reference [103].

Finally, it should be noted that the contact potentials inside the electrical circuit connecting the electron spectrometer with the sample holder, lead to an additional potential difference between the sample surface and first lens. Therefore, the actually detected kinetic energy of the electrons amounts to

$$\begin{aligned} E_{\text{kin}} &= h\nu - E_{\text{bin}} - \phi_{\text{S}} + (\phi_{\text{S}} - \phi_{\text{A}}) \\ &= h\nu - E_{\text{bin}} - \phi_{\text{A}} \end{aligned} \tag{4.2}$$

with the work functions of the sample ϕ_{S} and and the so-called work function of the spectrometer ϕ_{A}. The detected E_{kin} thus does not depend on ϕ_{S} and in order to determine E_{bin}, solely ϕ_{A} must be known. This quantity can be determined by the energetic position of the Fermi edge in the spectrum of a metallic sample, since the Fermi levels of the metallic sample and the spectrometer will equalize once the contact between both is established.

4.4.3 SPELEEM at SPring-8

For the X-PEEM and LEED experiments, the spectroscopic photoemission and low-energy electron microscope (SPELEEM) located at beamline BL17SU, SPring-8 was employed. The achieved lateral resolution in PEEM mode is 22 µm. The apparatus is based on a low-energy electron microscope (LEEM III, Elmitec GmbH) that was extended by means of an energy analyzer in order to provide spectroscopic imaging capabilities [104]. This instrument provides imaging, diffraction, and dispersive operation modes, of which only the former two were used in this work. At beamline BL17SU the conventional horizontal SPELEEM setup was modified and installed in an upright position [96, 105, 106].

The electron optical system displayed in figure 4.10 consists of several magnetic lenses, apertures, and slits. In this setup, the sample floats at a high voltage up to 20 kV. The illumination and area selection apertures residing in the beam separator are used for the determination of the area of interest in LEED mode, whereas the contrast aperture improves the image quality in imaging mode. Four straight optical columns are linked by two 60° deflections inside the beam separator and one 180° deflection inside the energy analyzer. The beam separator enables electron illumination and detection at normal incidence angle with respect to the sample surface, which is required for the LEED experiment, as well as for LEEM imaging [107].

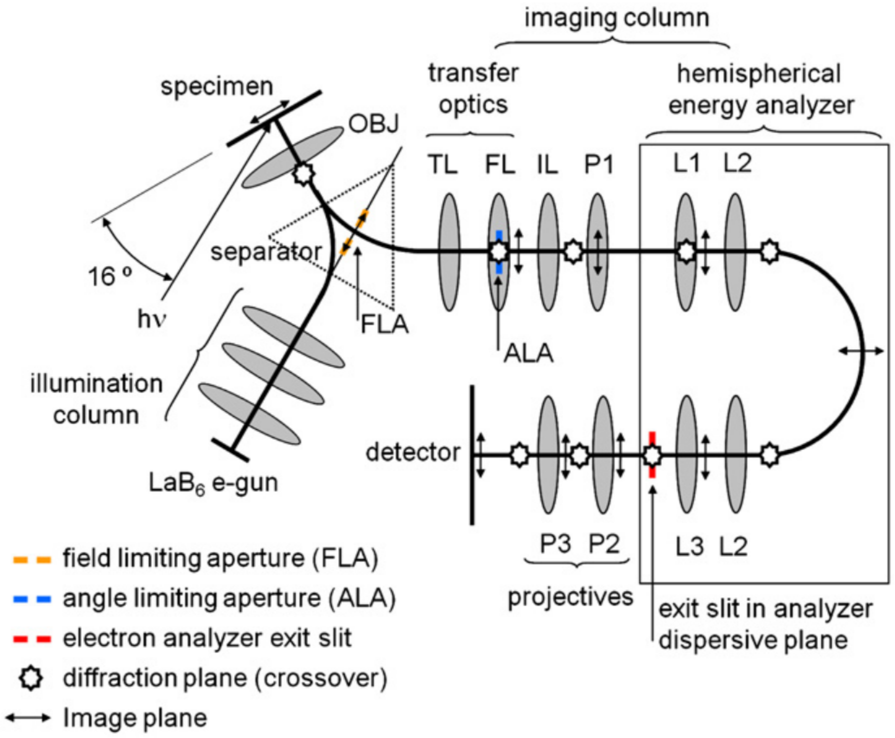

Figure 4.10: Illustration of the lens system of the SPELEEM [108].

The illumination column consists of an electron gun, condenser lenses, and an illumination aperture that allows limiting of the electron beam diameter. In PEEM mode, the illumination column is omitted and the sample is irradiated by soft x-rays from BL17SU at a grazing incidence angle of 16°. In order to capture UV-PEEM images, a complementary mercury short-arc lamp (LOT-QuantumDesign GmbH) can be attached at a vacuum view-port. The remaining optical path starting at the objective lens is used in any operating mode. In the imaging column, the main magnification occurs and a contrast aperture in the field lens is used to reduce aberrations. Switching between the imaging and diffraction operating modes is achieved by means of adjusting the current of the intermediate lens. The energy analyzer, and the projection column complete the electron optics. The projection column contains the micro-channel plates that intensify the electron signal and is terminated by the phosphorous screen for the conversion of the electron image into a light optical image. Finally, the image is digitized by means of a CCD camera.

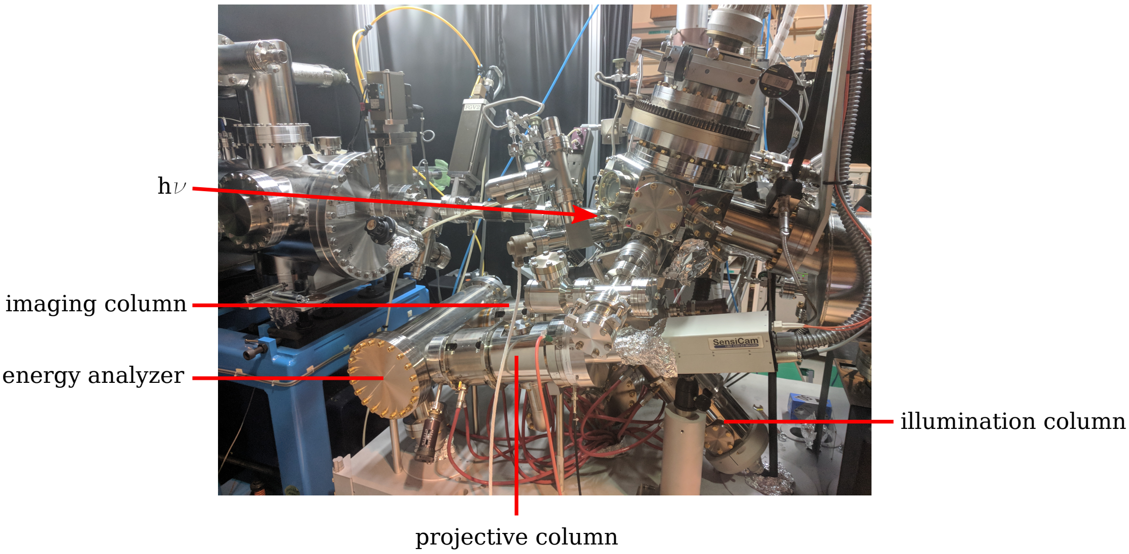

Figure 4.11: Photograph of the main chamber of the SPELEEM setup. The preparation chamber and the load-lock are concealed in this photograph.

The vacuum system consists of a load-lock, a preparation chamber, and the main chamber. The base pressures in the main and preparation chambers are 2×10^{-9} mbar and 2×10^{-8} mbar, respectively. To minimize pumping time and enable fast entry of new samples, venting of the load-lock is always carried out using dry nitrogen. Since up to three samples can be stored inside the load-lock, new samples can be prepared in the preparation chamber during ongoing experiments in the main chamber. Sample annealing is possible in both the main and preparation chambers by means of filament radiation or electron bombardment. The filament is installed inside in the sample holder (ELMITEC standard sample cartridge), whose electrical connections to the manipulator head are carried out with flat springs. All measurements were carried out at a temperature of about 200 °C in order to prevent carbon contamination of the sample surface. Figure 4.12 displays a sample holder identical to that was used for this experiment. The sample holder consists of a base plate on top of which the sample is positioned and covered by a plate with circular window. Below the base plate, two of the flat spring electrical connections are visible. The temperature was checked by means of a thermocouple installed in the sample holder as well as by means of a pyrometer (IGA 6/23 Lumasense) attached to a vacuum view port. In the preparation chamber, the electron beam evaporator

(EFM 3) that was described in section 4.2.2 and a quartz crystal microbalance are installed. The manipulator in the main chamber enables translation in all three spatial directions as well as tilting the sample surface and rotation around the surface normal of the sample.

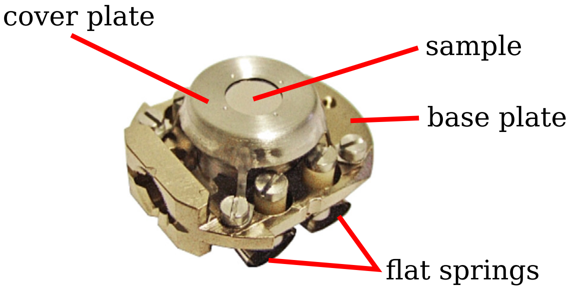

Figure 4.12: Standard ELMITEC sample holder, identical to that used in the SPELEEM experiment. The annotations were added after the photograph was taken from reference [109].

5 The reconstructed silicon carbide surface

As stated in section 2.1.4, the $6\sqrt{3}$ reconstructed SiC(0001) surface is an ideal substrate for the preparation of intercalated monolayer graphene on silicon carbide. Consequently, this surface was chosen as a substrate for the production for cobalt-intercalated graphene. The preparation procedure for the SiC(0001) surface was optimized to achieve large-area and homogenous growth of the $6\sqrt{3}$ reconstruction. In this chapter, the preparation of the silicon carbide samples is described and their structural and chemical properties are investigated. Using UV-PEEM and LEED, the surface structure is determined in real and reciprocal space, respectively. By means of XPS the chemical state of the samples is analyzed.

5.1 Sample preparation

Silicon carbide of the polytype 6H was obtained from NovaSiC, France in form of n-doped two-inch wafers. The silicon-terminated (0001) surface was chemical-mechanical polished by the supplier. The wafer was cut into samples with the dimensions of $8.2 \times 5.8\,\mathrm{mm}^2$. Samples that were originally located closer to the center of the wafer were preferred since they provide a higher homogeneity of the surface after preparation. Potential contamination of the samples due to organic substances was eliminated by starting the preparation process with a wet-chemical cleaning consisting of rinsing for 10 min in an ultra-sonic bath with acetone and isopropanol, respectively. In some cases, the evaporation of the residual solvent was accelerated by a nitrogen flow. Then, the sample was inserted into the graphite crucible with an end-cap bore diameter of 1 mm described in detail in section 4.2.1. After the crucible was installed in the vacuum furnace, the system was allowed to pump out for 16 h leading to a base pressure of 2×10^{-8} mbar. Subsequently, the annealing protocol described below that has previously produced large and ordered terrace structures [110] was applied.

The optimized parameters that led to the results presented in this chapter are declared below, with the temperature values given in relation to the external surface of the crucible. First, the crucible was heated at 750 °C for 3 h in order to remove adsorbates from both the sample and the crucible. Then, 900 mbar of argon gas (purity 5.0) was let in the chamber and the system was allowed to equilibrate for

10 min. Subsequently, the temperature was linearly increased to 1500 °C during 5 min. This temperature was maintained for 30 min, before it was linearly decreased during 15 min to 700 °C, which was the lowest possible temperature due to the minimum output power of the power supply. Afterwards, the power supply was turned off and the system cooled down to room temperature, so that after about 1 h the crucible could safely be removed from the furnace. After this preparation procedure the samples were transferred in air to the respective analysis chamber. Prior to the further experiments, the samples were annealed at about 300 °C for a few minutes to remove adsorbates. The above-mentioned procedure was identical for all samples investigated in this work.

5.2 Ultraviolet photoemission electron microscopy

Figure 5.1 displays a typical UV-PEEM image with a field of view of 15 µm of a sample that was prepared with the parameters given in section 5.1. Contrary to all further UV-PEEM images that will be shown in this thesis, the image in figure 5.1 was acquired with the SPELEEM setup described in section 4.4.3, due to its better lateral resolution. As for all UV-PEEM images shown in this work, the light source was a mercury discharge lamp with a maximum photon energy of $h\nu = 4.9\,\mathrm{eV}$. The image shows a periodic structure of nearly parallel stripes separated by narrow lines. Three different gray values can be distinguished; the wide stripes appear in light and medium gray, whereas the narrow lines appear in dark gray. The stripes possess widths exceeding 2 µm and they are separated by lines with a width of about 150 nm.

This periodic structure results from the steps that separate the terraces of the SiC(0001) surface. The step formation is a result of an inclination of the actual surface normal towards the [0001]-direction of the SiC crystal, due to the so-called miscut of the wafer. The sample surface thus breaks up into terraces exposing the (0001) surface, separated by steps whose height is at least that of an individual SiC-bilayer. The actual step height in the as-polished state depends on the polishing procedure; typical values are 2.5 Å, 7.5 Å, and 15 Å, respectively, which correspond to one bilayer, half a 6H unit cell, and a full 6H unit cell height. At a given step height c the terrace width is $d = c/\tan\alpha$ with the miscut angle α. In principle, the miscut is unavoidable but miscut angles smaller than 0.5° are routinely achieved. The terrace width, that is of the order of 100 nm in the as-cut and polished surface state [110, 111], is strongly enhanced in figure 5.1. This effect is called step bunching [112] and results from the merging of adjacent terraces promoted by the high temperature during the preparation process.

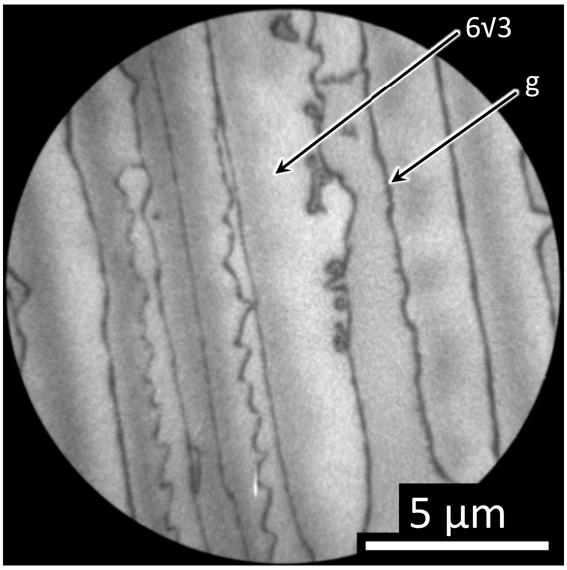

Figure 5.1: UV-PEEM image acquired with the SPELEEM apparatus of a reference sample prepared with the parameters given in section 5.1.

The step height of samples stemming from the same batch of wafers and that were prepared with similar parameters to those stated in section 5.1 is of the order of 10 nm [110]. For this height, significant topographic contrast is not expected [113]. Therefore, it is assumed that figure 5.1 solely exposes work function contrast and that the relative intensity of the areas within the field of view is inversely proportional to their work function. For the further interpretation of figure 5.1, an understanding of the expectable work function values is necessary. References [114–116] report work function values for several surfaces phases of 6H-SiC(0001), from unprepared up to heavily graphitized. They are plotted in figure 5.2 as a function of the carbon/silicon ratio at the surface that is proportional to the temperature and duration of the graphitization process.

Figure 5.2 shows that the work function is minimal for the $\left(6\sqrt{3}\times 6\sqrt{3}\right)$-R30° reconstruction, thus the brightest areas in figure 5.1 are $6\sqrt{3}$ reconstructed terraces. Since the work function increases for both the $\left(\sqrt{3}\times\sqrt{3}\right)$-R30° reconstruction and a graphene monolayer, the dark lines could in principle be linked either to the $\sqrt{3}$ reconstruction or to a monolayer of graphene. However, the work function of the $\sqrt{3}$ reconstruction is almost as high as the photon energy, thus no significant intensity is expected to be emitted from the respective areas, contrary to what is observed in figure 5.1. Therefore, it is assumed that the $\sqrt{3}$ reconstruction is not the cause for the dark lines, but rather that they are corresponding to monolayer graphene that starts to grow in proximity of the step edges.

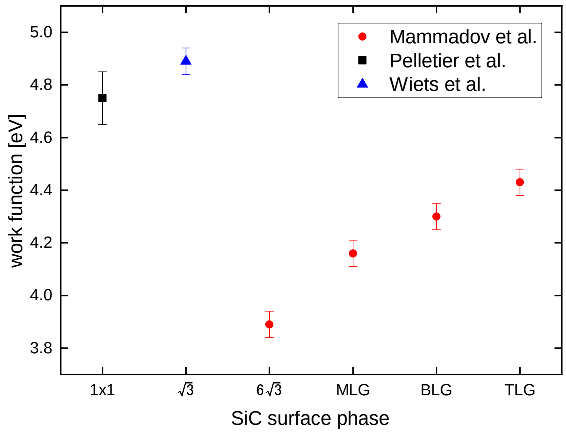

Figure 5.2: Experimental work function values for several 6H-SiC(0001) surface phases: unreconstructed (1×1), $\sqrt{3}$ reconstruction, $6\sqrt{3}$ reconstruction, monolayer graphene (MLG), bilayer graphene (BLG), and trilayer graphene (TLG). The values were extracted from references [114–116].

As already mentioned above, the detailed inspection of the bright terraces in figure 5.1 reveals light and medium gray values, indicating variations of the work function of the terraces. Since the growth of graphene layers starts at the step edges, as indicated here and observed previously [16, 117], it is not expected that the areas at the terraces exposing intermediate gray values correspond to graphene layers. Rather, it is assumed that the step bunching effect due to the high annealing temperature may result in differing sub-surface stacking orders. These can be considered as local variance of the polytype since the polytypism of SiC also results from different 60°-rotated bilayer stacking sequences. Indeed, reference [115] reports different work function values of the $\left(\sqrt{3} \times \sqrt{3}\right)$-R30° reconstructed (0001)-surface for the 4H-SiC and 6H-SiC polytypes. Though comparable values for both polytypes are only available for the $\sqrt{3}$ reconstruction, it is expected that a dependence of the work function on the polytype exists also for the $6\sqrt{3}$ reconstruction. Reference [118] also reports two distinct gray values at the same $6\sqrt{3}$ reconstructed terrace using low-energy electron microscopy, attributing it to two different 60°-rotated orientations.

Finally, the growth parameters applied to yield the results discussed above should be compared to some reported previously. Upon annealing at 1450 °C for 15 min in argon atmosphere, a $6\sqrt{3}$ reconstructed surface without the growth of a graphene monolayer has been reported in references [119, 120]. Further, the onset of graphene monolayer growth at 1500 °C for 15 min has been reported in reference [120]. These reported preparation temperatures are similar to those used in this work, though the annealing time was twice as long in the present work. However, the necessary annealing time depends on the heat capacity of the furnace that should have been different in all three cases. Further, the silicon sublimation rate depends linearly on the annealing time but an exponential dependence on the temperature exists. Thus, an experimental uncertainty of the temperature measurements due to potentially different emissivity settings of the pyrometers used in each study might additionally be accountable for the slightly different results.

To sum up, the UV-PEEM investigation shows that the preparation parameters given in section 5.1 lead to a large-area growth of the $6\sqrt{3}$ reconstruction with small inclusion of monolayer graphene.

5.3 Low-energy electron diffraction

In this section, the structure of the surface is investigated in reciprocal space using LEED. In order to obtain a diffraction pattern that does only contain information about the terraces that were revealed by the UV-PEEM analysis in the previous section, the size of the probing area was limited by the diameter of the electron beam that was set to 1.4 µm by means of an illumination aperture. Figure 5.3 shows the resulting LEED pattern ($E_{\text{kin}} = 50\,\text{eV}$) acquired with the SPELEEM apparatus of a sample prepared with the parameters discussed in section 5.1. The pattern is slightly distorted due to a minor misalignment of the complex electron optics of the SPELEEM apparatus.

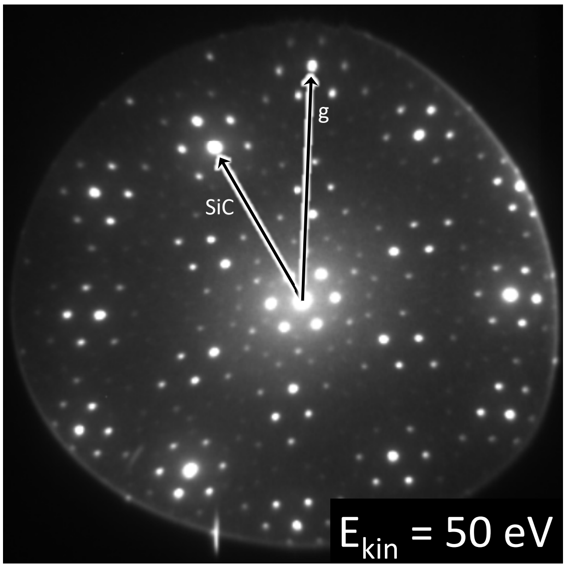

Figure 5.3: LEED pattern taken at a terrace with $E_{\text{kin}} = 50\,\text{eV}$. The arrows indicate positions on the (1×1) grids of SiC and graphene.

The pattern reveals the two hexagons of the SiC and graphene lattices, respectively, and a wealth of superstructure spots. Arrows in figure 5.3 indicate spots on positions of the (1×1) grids of the SiC and graphene lattices. At first sight, the presence of the strong spots on the (1×1) graphene grid may seem puzzling, since a bare $6\sqrt{3}$ reconstruction without an additional graphene layer on top is expected. Yet, the strong spots on the (1×1) graphene grid result from the $6\sqrt{3}$ reconstruction, which is in fact a hexagonal carbon layer with the same lattice constant as graphene, though it has a different chemical environment [46, 121]. Except for the spots on the (1×1) SiC grid, all other spots in the pattern also result from the $6\sqrt{3}$ reconstruction. Especially in the center of the pattern, several spots with distances of $1/6\sqrt{3}$ of the SiC reciprocal unit mesh vector are present, revealing the $6\sqrt{3}$ periodicity of the pattern.

However, it can be argued that many of the superstructure spots reside on a (6×6) grid with respect to the reciprocal SiC unit mesh vector, as for instance those in the vicinity of the (1×1) spots of the SiC and graphene grids. Still, the (6×6) grid is a subset of the $6\sqrt{3}$ grid, therefore the fundamental periodicity of the pattern is defined by the $6\sqrt{3}$ grid. The complexity of this pattern was the source of a long-lasting debate about the atomic structure in real space, supported by the fact that an apparent (6×6) superstructure is frequently observed in scanning tunneling microscopy (STM) [122]. Eventually, the successful imaging of the $6\sqrt{3}$ periodicity with STM [46, 121] led to an agreement with the results obtained by LEED. The absence of many spots on the $6\sqrt{3}$ grid was attributed to kinetic suppression [123].

Further inspection of the pattern in figure 5.3 reveals a threefold symmetry of the SiC spots, despite a sixfold symmetry is usually observed with a conventional LEED setup. It can be concluded that only one of the sub-surface crystal termination [118, 124] is probed within the individual LEED pattern due to the small size of the electron beam. With a conventional LEED setup, an average over several differently terminated areas is obtained, thus a sixfold symmetry will be the result. This finding is consistent with the UV-PEEM experiment, which also revealed different terminations.

It has been shown in this section that the bright areas in figure 5.1 are $6\sqrt{3}$ reconstructed. In the next section, the chemical properties of this surface will be investigated using XPS.

5.4 Photoelectron spectroscopy

The results presented in the previous sections revealed a large-area growth of the $6\sqrt{3}$ reconstruction along with small inclusions of monolayer graphene. To complete the characterization of the samples, in this section, the chemical properties of a sample that was prepared with the parameters described in section 5.1 are investigated by XPS. The experiment was carried out at the DELTA synchrotron radiation source with the XPS apparatus described in section 4.4.2. In this experiment, the analysis area is determined by the size of the synchrotron radiation spot, which covers several terraces and step edges of the sample. Thus, the spectra represent an average of these areas.

In the following, survey spectra provide information about the elemental composition of the surface and high-resolution spectra of the C 1s and the Si 2p orbitals give an insight into the chemical states of the carbon and silicon atoms. In order to reveal the chemically shifted components of the high-resolution spectra, a peak fitting procedure using the software UNIFIT 2017 [73] was carried out. In this process, a Shirley background was fitted simultaneously with the chemically shifted components and subtracted from the spectra after the fit converged. The fit parameters kinetic energy E_{kin}, relative kinetic energy with respect to the bulk component $\mathit{\Delta} E_{\text{kin}}$, relative intensity I, and full width at half maximum w are shown in table 5.1. All spectra were recorded for the polar electron emission angles $\theta = 0°$ and $\theta = 60°$. As described in section 3.2, the surface sensitivity is increased for higher polar angles. First, the spectra for $\theta = 0°$ were fitted. Then, the resulting fit parameters, except for the relative intensity, were kept constant for the fit of the $\theta = 60°$ spectrum.

Figures 5.4 (a) and (b) display the surface and bulk sensitive survey spectra taken at a photon energy of $h\nu = 650\,\text{eV}$. This photon energy was chosen as it is sufficient to excite the O 1s core-level electrons, since oxygen is the main contamination that is to be expected after transport of the sample through the atmosphere. The spectra reveal the C 1s, Si 2s, and Si 2p photoelectron signals along with the C KVV and Si L_{23}VV Auger signals. The photoelectron lines are associated with characteristic electron energy-loss peaks occurring at 23 eV lower kinetic energy, which result from plasmon excitations in the bulk of the SiC crystal [125]. No other elements can be found within the detection limit, as expected for a clean sample. In particular, oxygen contamination can be ruled out due to the absence of an O 1s peak that would be observable at $E_{\text{kin}} = 118.5\,\text{eV}$. The surface sensitive spectrum displayed in figure 5.4 (b) reveals a significantly increased relative intensity of the C 1s peak with respect to the Si 2p peak. This finding confirms a carbon-rich surface, as expected for the $6\sqrt{3}$ reconstruction.

The surface and bulk-sensitive high-resolution C 1s spectra taken at $h\nu = 600\,\text{eV}$ are displayed in figures 5.4 (c) and (d), respectively. Four chemically shifted components S2, S1, G, and SiC with Voigt lineshape were necessary for a satisfying fit to the spectrum, whose fit parameters are shown in the upper part of table 5.1. According to references [20, 126], the components S1 and S2 result from two different chemical environments inside the $6\sqrt{3}$ reconstructed layer, the component G results from the graphene monolayer areas, and the component SiC is the bulk component.

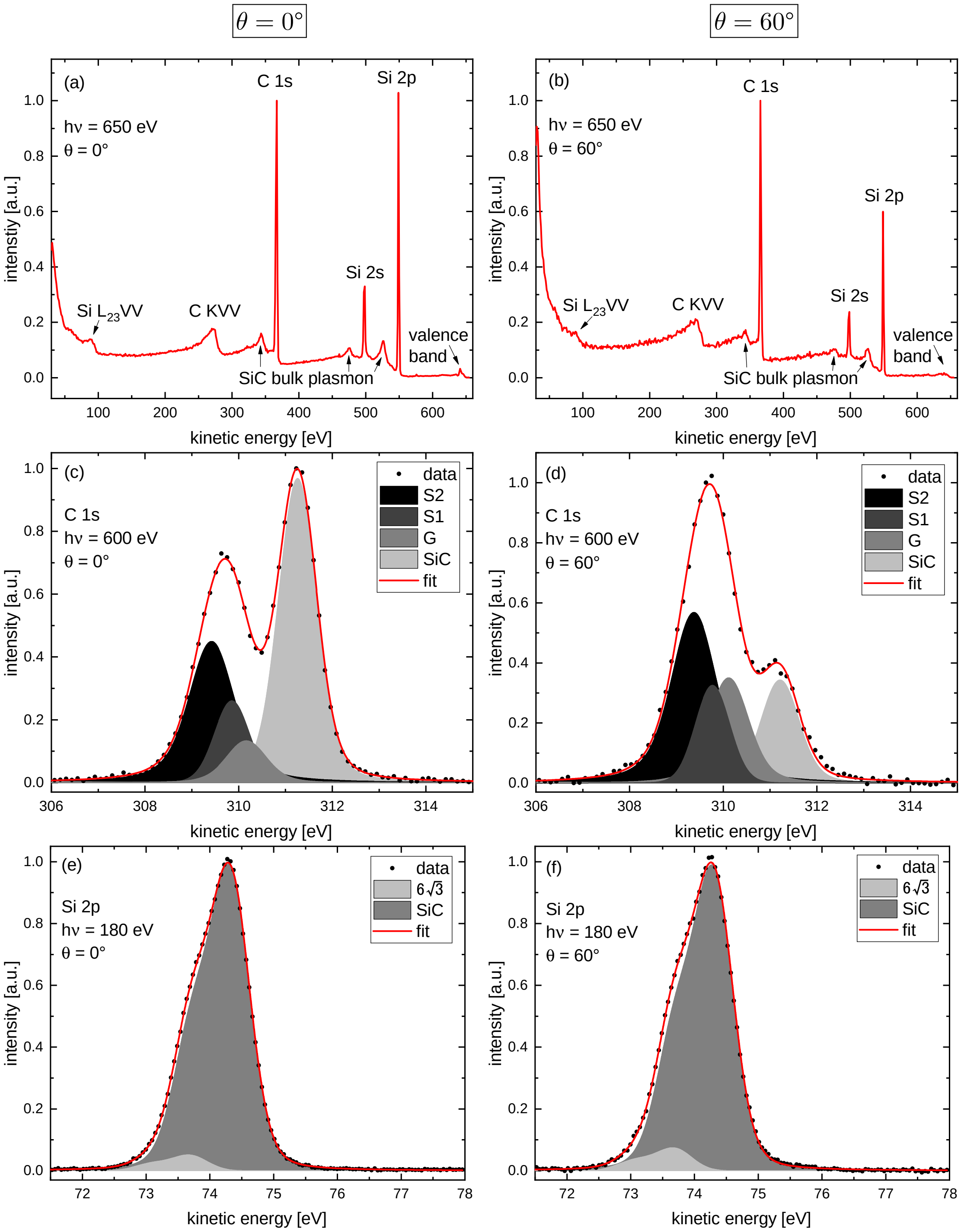

Figure 5.4: Bulk (left column) and surface sensitive (right column) photoelectron spectra taken at polar electron emission angles of $\theta = 0°$ and $\theta = 60°$, respectively: survey spectra (a) and (b), high-resolution spectra of the C 1s orbital (c) and (d), and high-resolution spectra of the Si 2p orbital (e) and (f).

Here, an additional fit parameter accounting for the asymmetry of the component G due to the metallic character of the graphene layer was not introduced, due to the difficulty of separating the components S1 and G within the given experimental resolution. The chemical shift of the component S2 with respect to the component SiC agrees excellent within 0.01 eV with the value published in reference [121], while the deviations for the components S1 and G are less than 0.15 eV.

Comparing the surface and bulk sensitive spectra, the relative intensity of the component SiC shows the strongest decrease in the surface sensitive spectrum with respect to the bulk sensitive spectrum. This confirms that this component originates from the bulk Si-C bonds. Conversely, the other three components result from surface phases. Moreover, the relative intensity of the component G with respect to the components S2 and S1 increases. Note that, as explained in section 2.1.3, the graphene monolayer is always associated with a $6\sqrt{3}$ reconstructed layer underneath. Therefore, the component G results from the top-most carbon atoms and the components S2 and S1 result from a carbon layer in between. The higher relative intensity of the sum of the components S1 and S2 with respect to the component G, as observed in both spectra, confirms that the $6\sqrt{3}$ reconstruction is the predominant surface phase. This finding is consistent with the large $6\sqrt{3}$ reconstructed terraces found in the UV-PEEM image in section 5.2. Consequently, the component G is attributed to graphene monolayer regions near the step edges. Due to its small intensity fraction in figure 5.4, an incomplete graphene coverage far below one monolayer is deducible from the XPS spectra [20]. These findings are in complete accordance with the interpretation of the UV-PEEM image in section 5.2.

The occurrence of two separate components for the $6\sqrt{3}$ reconstructed carbon layer is discussed in the following. As explained in section 2.1.3, the $6\sqrt{3}$ reconstruction is a partially covalently bonded graphene-like carbon layer. Therein, the atoms that are solely bonded to other carbon atoms give rise to the component S2, whereas the component S1 results from those carbon atoms that are additionally bonded to silicon atoms underneath. The comparison of the surface and bulk-sensitive spectra shows that the intensity ratio of the components S1 and S2 is almost independent of the polar angle, which emphasizes that both components result from atoms residing in the same plane. Their intensity ratio reflects the fact that the density of carbon atoms in the $6\sqrt{3}$ reconstruction is three times higher than that of the silicon atoms in an SiC-bilayer [126]. Therefore it is expected that one-third of the carbon atoms in the $6\sqrt{3}$ layer is bonded to silicon atoms whereas two-thirds are only bonded to carbon atoms, which leads to an intensity ratio of $I\,(\mathrm{S1})\,/I\,(\mathrm{S2}) \approx 0.5$. Here a value of $I\,(\mathrm{S1})\,/I\,(\mathrm{S2}) \approx 0.4$ is obtained. The deviation from the expected value is attributed to uncertainties of the separation of the components S1 and G arising from their close kinetic energies.

The chemical state of the silicon atoms is investigated by means of high-resolution spectra of the Si 2p orbital taken at $h\nu = 180\,\mathrm{eV}$. In figures 5.4 (e) and (f) the bulk and surface sensitive spectra are displayed, respectively. Resulting from an orbital with non-vanishing spin-orbit coupling, the spectra consist of doublet components, as discussed in section 3.2. Here, two doublet components were necessary for a sufficient fit to the spectra, whose fit parameters are shown in the lower part of table 5.1.

The spin-orbit splitting of the doublet components was resolved to $\mathit{\Delta} E_{\mathrm{SOC}} = 0.60\,\mathrm{eV}$, which is in good accordance with the reported values that are in the range of 0.60–0.63 eV [127]. For clarity, table 5.1 shows only the parameters of the $2\mathrm{p}_{3/2}$ components. Comparing the surface- and bulk-sensitive spectra, the component SiC can be attributed to the bulk. The other component is chemically shifted by $-0.64\,\mathrm{eV}$ and results from the $6\sqrt{3}$ reconstruction [20, 126]. In the surface sensitive spectrum it exposes an increased intensity, as expected for the $6\sqrt{3}$ reconstruction. No other chemically shifted component was observed, as expected, since the silicon atoms are either in the bulk configuration or bonded to the $6\sqrt{3}$ reconstructed carbon layer, therefore no other chemical environment exist. In some previous studies the presence of a third chemically-shifted component was recognized in the Si 2p spectrum and accounted to surface defects [119, 121]. However, this component was not required here to achieve a good fit.

After all, these results are consistent with those obtained by the UV-PEEM experiment. Further, a good agreement with the spectra and those reported for a predominant $6\sqrt{3}$ reconstruction with small monolayer graphene inclusion [20, 126] was observed.

Table 5.1: Fitting parameters of the individual components of the C 1s and Si 2p core-level peaks displayed in figures 5.4 (c) – (f): kinetic energy E_{kin}, relative kinetic energy with respect to the bulk component $\mathit{\Delta} E_{\mathrm{kin}}$, relative intensity I, and full width at half maximum w.

		$\theta = 0°$				$\theta = 60°$			
peak	comp.	E_{kin}/eV	$\mathit{\Delta} E_{\mathrm{kin}}$/eV	I/%	w/eV	E_{kin}/eV	$\mathit{\Delta} E_{\mathrm{kin}}$/eV	I/%	w/eV
C 1s	SiC	311.26	0.00	51	0.96	311.21	0.00	20	0.96
	G	310.16	-1.10	8	1.01	310.12	-1.09	22	1.00
	S1	309.84	-1.42	12	0.87	309.79	-1.42	16	0.86
	S2	309.42	-1.84	30	1.14	309.37	-1.84	42	1.14
Si 2p	SiC	74.33	0.00	65	0.71	74.31	0.00	64	0.71
	$6\sqrt{3}$	73.70	-0.64	3	0.64	73.68	-0.64	4	0.64

5.5 Summary

Silicon carbide samples were prepared according to the procedure described in section 5.1 and characterized with UV-PEEM, LEED, and XPS. The UV-PEEM analysis revealed the presence of large $6\sqrt{3}$ reconstructed terraces and small monolayer graphene stripes at the step edges. Using LEED, it was confirmed that the terraces that were observed in the UV-PEEM image are indeed $6\sqrt{3}$ reconstructed. Further, the XPS survey spectra confirmed that the as-prepared surface is carbon-rich and free of contamination. An analysis of the C 1s core-level spectra revealed a mixing of a majority of the $6\sqrt{3}$ reconstruction and minor monolayer graphene contributions, consistent with the UV-PEEM results. The decomposition of the Si 2p XPS spectra revealed the presence of the bulk and $6\sqrt{3}$ components, as expected for $6\sqrt{3}$ reconstructed SiC.

Hence, large-area growth of the $6\sqrt{3}$ reconstruction has been proven by the combination of three independent methods. These results show that samples prepared with the parameters given in section 5.1 provide an excellent basis for the investigation of cobalt adsorption and intercalation underneath $6\sqrt{3}$ reconstructed SiC.

6 As-deposited cobalt films

The characterization of the SiC samples in the previous chapter showed a homogenous large-area growth of the $6\sqrt{3}$ reconstruction throughout the terraces of the surface. Near the step edges, stripes of graphene monolayers have formed. In this chapter, the structural properties of cobalt films deposited on this surface are investigated. Further, it will be revealed whether any chemical changes with respect to the pristine $6\sqrt{3}$ samples occur at the cobalt-SiC interface at room temperature. Finally, the magnetic domain structure of the as-deposited cobalt films will be analyzed by means of X-PEEM images with magnetic contrast.

6.1 Sample preparation

Due to the high chemical reactivity of cobalt, the preparation of the cobalt films must be carried out in-situ. Since the UV-PEEM, XPS, and SPELEEM experiments are situated in separate UHV chambers, it was necessary to repeat the cobalt preparation process for each particular experiment. For all experiments, samples of comparable thicknesses were prepared in order to relate their results. The cobalt film thicknesses t_{Co} that were investigated in this work span the range of 0.4–12 nm. A fresh $6\sqrt{3}$ reconstructed SiC sample equivalent to those discussed in chapter 5 was used for each cobalt film thickness condition. All results for a particular combination of experimental setup and film thickness were obtained from the identical specimen.

The cobalt films were prepared using electron beam evaporators equipped with high purity cobalt rods with diameters of 2 mm. At the UV-PEEM and SPELEEM experiments, identically constructed evaporators were used (EFM 3, Focus GmbH), whereas a similar type was used at the XPS experiment (EFM 3T, Focus GmbH). The operating principle of the EFM 3 evaporator is described in more detail in section 4.2.2. Typically, the heating power, which is defined as the product of the high voltage and the emission current, was set to $P \approx 14\,\mathrm{W}$. During the evaporation, the samples were held at room temperature. The thickness of the deposited films was controlled by adjusting the evaporation time, utilizing the linear relationship between both quantities. For this purpose, the evaporation rate must be known. It was measured by different methods, depending on the experimental chamber.

For the samples prepared during the PEEM experiment at TU Dortmund, the film thickness was measured directly by atomic force microscopy. In particular, the step height at the edge of cobalt films that were evaporated through an aperture onto the sample surface were measured for three reference samples with evaporation times of 8–32 min. The deposition rate was determined to 0.35 nm/min through a linear fit. For the sample prepared in situ in the XPS experiment, the intensity reduction of high-resolution spectra of the Si 2p core level taken before and after cobalt deposition revealed a deposition rate of 0.05 nm/min. During the SPELEEM experiment, a quartz crystal micro-balance was used revealing a deposition rate of 0.16 nm/min. Though approximately the same evaporation power was used in all experiments, the evaporation rates deviate. The deviations are due to the different distances of the evaporator and the sample, depending on the experiment. An influence of the different deposition rates on the film properties was not observed throughout the experiments. The particular film thicknesses of all samples that are discussed in this work are summarized in table 6.1.

Table 6.1: Summary of all prepared film thicknesses that are discussed in this work.

Experiment	Film thickness / nm						
UV-PEEM	0.4	0.7	1.4	2.8	5.6	11	12
XPS	0.4						
SPELEEM	0.4	0.6	1.1	1.5	3.0	6.0	

6.2 Ultraviolet photoemission electron microscopy

Figure 6.1 displays UV-PEEM images acquired with the setup described in section 4.4.1 after deposition of cobalt films with thicknesses of 0.4–12 nm on $6\sqrt{3}$ reconstructed SiC samples. The measurements were made without intentionally heating the samples, however, the heat load of the mercury short arc lamp led to an increase of the sample temperature that was estimated to be well below 200 °C. Apart from the different shapes of the terrace step edges, the images are equivalent for all investigated film thicknesses. The different terrace shapes occur because the individual samples were cut out off different areas of a SiC wafer, the initial surface quality of which might deviate.

In the images, the terraces appear dark and the regions near the step edges appear bright. Thus, the contrast is inverted with respect to the reference image recorded prior to cobalt deposition that was discussed in section 5.2. The contrast inversion can be understood by consideration of the relative work functions of the pristine

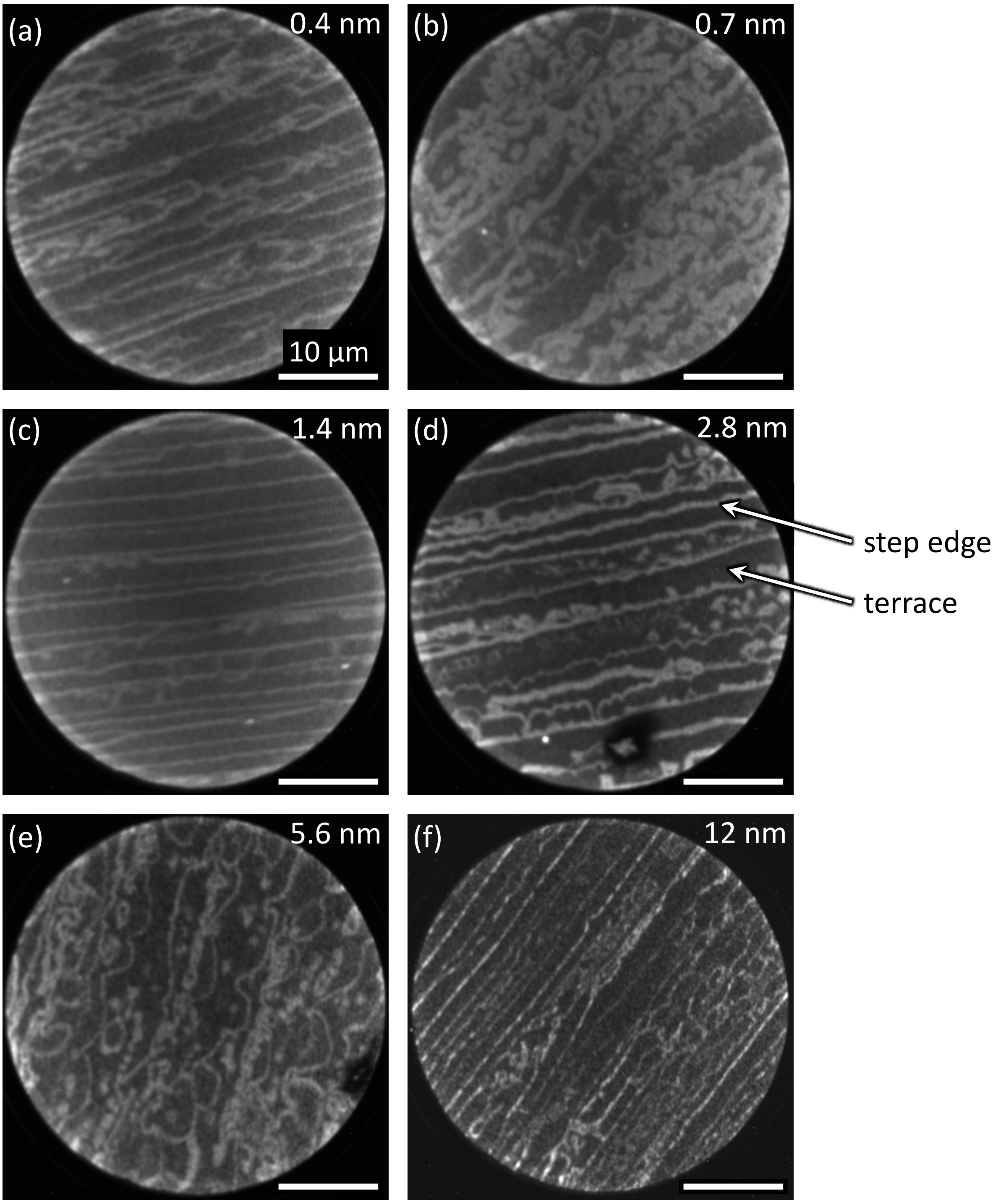

Figure 6.1: UV-PEEM images acquired after the deposition of 0.4–12 nm thick cobalt films on the $6\sqrt{3}$ reconstructed SiC surface. The individual cobalt film thicknesses are indicated in the images. The length of the scale bar is 10 µm for all images.

surface and that of the cobalt film. It is assumed that the work function of the cobalt-covered areas is a weighted average of the work functions of the pristine surface and the work function of bulk cobalt, with areas of higher cobalt coverage having a higher weight.

The reported work functions of polycrystalline cobalt and of the Co(0001) surface are 5.0 eV [128] and 5.55 eV [129], respectively. These values are significantly higher than those for a $6\sqrt{3}$ or graphene-covered surface which are at most 4.6 eV, as displayed in figure 5.1. A homogenous deposition of cobalt would thus explain a reduction of the average intensity but would not account for a contrast inversion. Therefore, the darker regions in figure 6.1 can be identified with regions of higher cobalt coverage. That is, more cobalt atoms are adsorbed on the $6\sqrt{3}$ reconstructed terraces than on the monolayer graphene at the step edges. The reason for the preferential adsorption on the $6\sqrt{3}$ reconstruction is the higher chemical reactivity of the $6\sqrt{3}$ structure compared to graphene.

The preferential adsorption on the $6\sqrt{3}$ surface has been observed earlier by scanning tunneling microscopy (STM) investigation of cobalt deposition on the $6\sqrt{3}$ surface and on monolayer graphene [130]. STM studies for cobalt coverage up to 0.15 nm further showed that the periodicity of the $6\sqrt{3}$ reconstruction promotes a cluster-like growth mode with cluster sizes of about 2 nm [131]. Since these clusters are small in comparison with the lateral resolution of all PEEM images shown in this work, it is not possible to observe the clusters directly. As mentioned earlier, the described appearance of the UV-PEEM image after cobalt deposition is the same for all investigated cobalt film thicknesses. This indicates that the growth mode is the same in each case. For higher film thicknesses, solely a weakening of the contrast between the step edges and the terraces is observed, since the influence of the work function difference between the $6\sqrt{3}$ and the monolayer structures decreases. Additionally, the average intensity reduces monotonically for higher cobalt coverage, as evident from the increased noise level in figure 6.1 (f).

In summary, cobalt films adsorb preferentially at the terraces rather than at the step edges and the films appear homogenous within the PEEM resolution limit. In the next section, the chemical properties of the interface of the cobalt film and the silicon carbide surface are investigated.

6.3 Photoelectron spectroscopy

To reveal whether a chemical reaction occurs after the deposition of cobalt on the $6\sqrt{3}$ reconstructed SiC surface, photoelectron spectra taken at room temperature are discussed in this section. The data presented here were taken with the same specimen that was discussed in section 5.4, without exposing it to the atmosphere. Directly after the measurements presented in section 5.4 were done, a 0.4 nm thick cobalt film was deposited at room temperature as described previously in section 6.1. Survey spectra taken at $h\nu = 650\,\mathrm{eV}$ for $\theta = 0°$ and $\theta = 60°$ are displayed in figures 6.2 (a) and (b), respectively. The Si 2p, the Si 2s, and the C 1s photoelectron peaks are visible in the spectrum, and their relative intensities are similar to the pristine sample prior to cobalt deposition. In addition, a Co 3p peak emerges, confirming the presence of cobalt on the surface. The mainly unchanged C 1s / Si 2p intensity ratios with respect to the state before cobalt deposition are a first indication that no intermixing of the cobalt and the underlying layers occurs at room temperature.

Figures 6.2 (c) and (d) display the high-resolution C 1s photoelectron spectra for $\theta = 0°$ and $\theta = 60°$ taken with $h\nu = 600\,\mathrm{eV}$. The spectrum is slightly shifted towards higher kinetic energy with respect to the reference spectrum shown in section 5.4, due to the Schottky barrier at the metal/semiconductor interface that is introduced by the cobalt adsorption [132]. Four components were fitted to the spectrum, two of which correspond to the $6\sqrt{3}$ reconstruction, while the remaining ones correspond to the monolayer graphene at the step edges and the bulk SiC component. The fitting parameters are displayed in table 6.2. Due to the fixed fit parameters E_{kin} and w for the $\theta = 0°$ and $\theta = 60°$ spectra, a slight imprecision of the fit of the $\theta = 60°$ spectrum is observed. It likely results from the uncertainty of the determination of the peak shapes of the S1 and G components, as discussed in section 5.4. However, the intensity ratios of the individual components are within a few percent identical to those measured before cobalt deposition. Further, the chemical shifts agree also within a few 10 meV with those measured before cobalt deposition. Thus, only minor changes of the spectra before and after cobalt deposition are observed.

Figures 6.2 (e) and (f) show the high-resolution Si 2p photoelectron spectra for $\theta = 0°$ and $\theta = 60°$ taken at $h\nu = 180\,\mathrm{eV}$. A shift due to the Schottky barrier occurred as well as for the C 1s spectrum. Three components were fitted to each spectrum, whose fitting parameters are presented in table 6.2. For clarity, in the table only the parameters of the $2\mathrm{p}_{3/2}$ components are shown. Two of these components correspond to the $6\sqrt{3}$ and the SiC bulk bonds already observed in section 5.4, while a third component was necessary to achieve a good fit. The third component could, in principle, be associated with a chemically shifted component due to cobalt silicide formation, however, it would be expected at a kinetic energy that is about

1 eV higher, as will be discussed in more detail in section 7.2.1. In addition, the best fit was achieved with a singlet component rather than a doublet component that would be expected for a p-orbital. Since the Co 3s photoelectrons possess almost the same binding energy than the Si 2p photoelectrons in the Si-C bulk state [133], it is therefore most likely that this component is due to Co 3s photoelectrons. Their small relative intensity is due to the about one order of magnitude lower cross-section than that of the Si 2p core-level [134]. Thus, no evidence for cobalt silicide formation at room temperature was found and besides the emergence of the Co 3s component, in the Si 2p spectrum no significant changes occur after deposition of cobalt.

As shown above, both the C 1s and the Si 2p core-level spectra remain mostly unchanged upon cobalt deposition at room temperature. Additionally, the survey spectra reveal similar relative intensities for the carbon and silicon-related peaks. These results are consistent with a cobalt overlayer that does not intermix with the underlying $6\sqrt{3}$ structure, since an overlayer does solely lower the average intensity but does not affect the ratios of the signals emerging from the buried layers. Though this argument is only strictly valid for signals possessing the same kinetic energy, for individual components inside a high-resolution spectrum the difference is negligible. The influence of the kinetic energy explains also the slightly increased Si 2p / C 1s intensity ratio in the survey spectrum displayed figure 6.2 (a) with respect to the pristine sample, since the Si 2p photoelectrons here possess a higher kinetic energy than the C 1s photoelectrons, which results in a higher inelastic mean free path. Thus, the Si 2p photoelectrons are less attenuated by the cobalt overlayer.

In summary, no chemical reaction of the as-deposited cobalt film with the underlying substrate can be recognized. In the next section, it will be investigated whether or not the as-deposited films are crystalline.

Table 6.2: Fit parameters for the C 1s and the Si 2p photoelectron spectra displayed in figure 6.2: kinetic energy E_{kin}, relative kinetic energy with respect to the bulk component ΔE_{kin}, relative intensity I, and full width at half maximum w.

		$\theta = 0°$				$\theta = 60°$			
peak	comp.	E_{kin}/eV	ΔE_{kin}/eV	A/%	w/eV	E_{kin}/eV	ΔE_{kin}/eV	A/%	w/eV
C 1s	SiC	311.39	0.00	48	0.96	311.39	0.00	19	0.96
	G	310.25	-1.14	7	1.10	310.25	-1.14	21	1.10
	S1	310.00	-1.38	10	0.82	310.00	-1.38	16	0.82
	S2	309.58	-1.80	34	1.18	309.58	-1.80	44	1.18
Si 2p	SiC	74.54	0.00	58	0.70	74.56	0.00	51	0.70
	$6\sqrt{3}$	73.94	-0.60	5	0.65	73.96	-0.60	6	0.67
	Co 3s	75.27	0.73	8	1.48	75.29	0.73	17	1.49

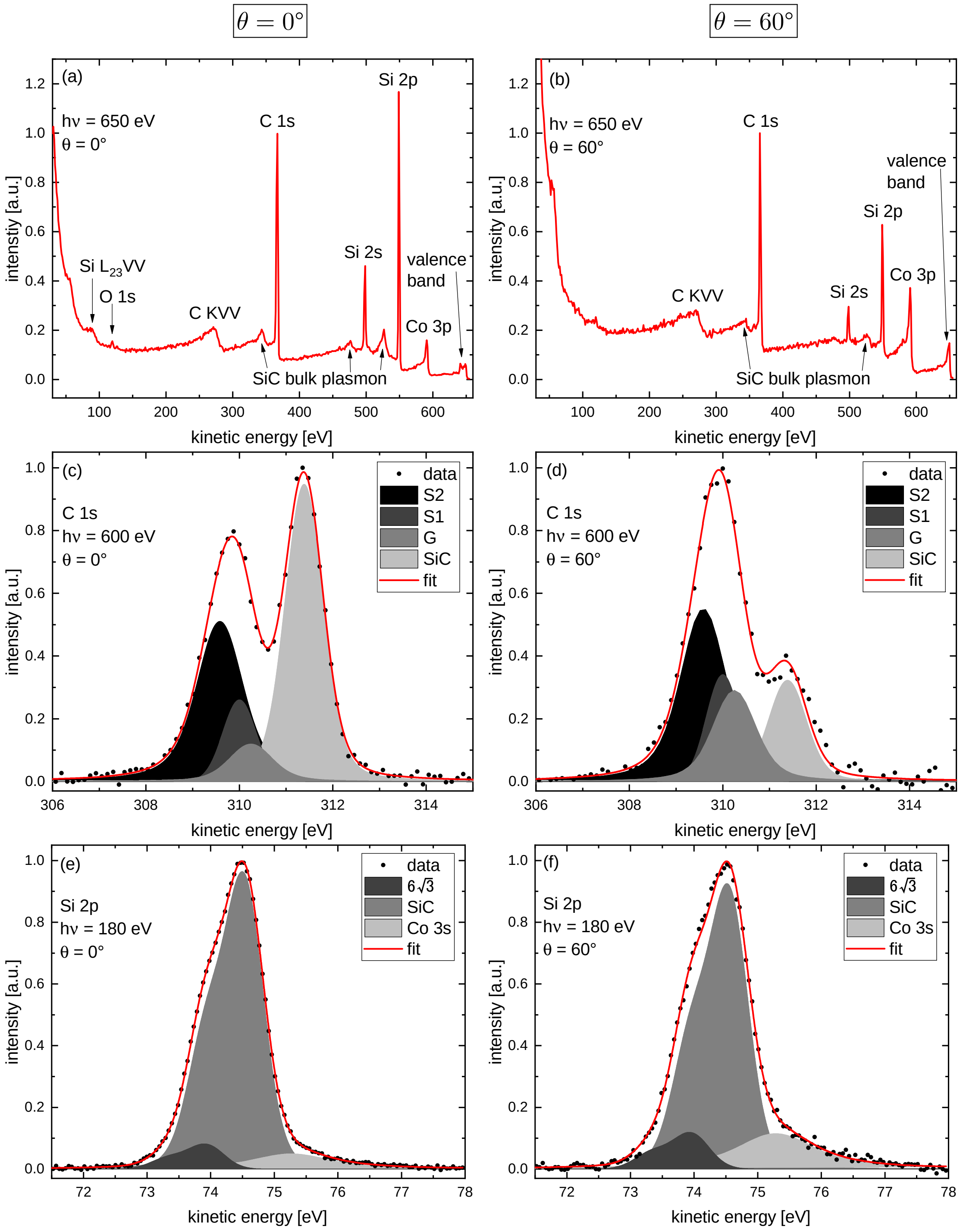

Figure 6.2: Photoelectron spectra taken at room temperature after deposition of 0.4 nm cobalt on the $6\sqrt{3}$ reconstructed SiC surface: survey spectra taken taken at (a) $\theta = 0°$ and (b) $\theta = 60°$, high-resolution XPS spectra of the C 1s orbital taken at (c) $\theta = 0°$ and (d) $\theta = 60°$, and high-resolution XPS spectra of the Si 2p orbital taken at (e) $\theta = 0°$ and (f) $\theta = 60°$.

6.4 Low-energy electron diffraction

In order to investigate the crystallinity of the as-deposited cobalt films, LEED patterns have been recorded using the SPELEEM apparatus. Figure 6.3 displays LEED patterns that were recorded after the deposition of cobalt films with thicknesses in the range of 0.4–6.0 nm. All patterns were recorded with the kinetic energy of the electron beam set to 50 eV. The diameter of the illuminated sample area was set to 1.4 µm by an aperture. For all patterns shown here the electron beam was directed to the center of a terrace. As for all measurements carried out with the SPELEEM apparatus, the sample temperature during the measurement was set to $\approx 200\,^\circ\mathrm{C}$.

A comparison of the patterns presented here with the reference patterns shown in section 5.3 reveals that the $6\sqrt{3}$ superstructure spots are strongly suppressed due to the cobalt overlayer. On the other hand, a new hexagonal pattern appears. It is rotated by 60° with respect to the SiC grid and the associated lattice parameter is approximately the same as that of the (1×1) graphene spots. The additional spots are identified with a crystalline cobalt film exposing the (0001) surface, since its lattice mismatch with respect to the graphene lattice is below 2 % [135, 136]. The distinct spots are only present for cobalt film thicknesses up to 1.5 nm, whereas for 3.0 nm the diffraction pattern is completely absent and for 6.0 nm only very faint diffracted intensity can be recognized. In all, the crystalline quality of the cobalt film is poor, which is evident from the large spot diameters and streaks that are visible in the patterns. While the large spot diameters indicate the growth of cobalt grains with small lateral dimensions, the streaks result from structural distortions along a preferred direction [86]. Further, a diffuse background is observed suggesting the presence of amorphous structures at the surface.

The distorted patterns for thin films and the absence of a significant diffracted intensity for the thick films indicates the presence of high intrinsic stress in the as-deposited cobalt films. The stress results from the low substrate temperature during deposition with respect to the melting point of the adsorbate [137]. If this ratio is too low, intrinsic stress piles up inside the as-deposited film, which increases for higher film thickness. Since this stress can be avoided by deposition at elevated temperature or by subsequent annealing, it is expected that the crystalline quality will improve during the annealing procedure that will be described in chapter 7. It should be noted that the LEED patterns that were discussed here were acquired at a measurement temperature of 200 °C, which suggests that this temperature is still too low to relieve the stress in the film.

In the next and final section of this chapter, x-ray photoemission electron microscopy is utilized in order to reveal the morphology and the magnetic microstructure of the as-deposited cobalt films.

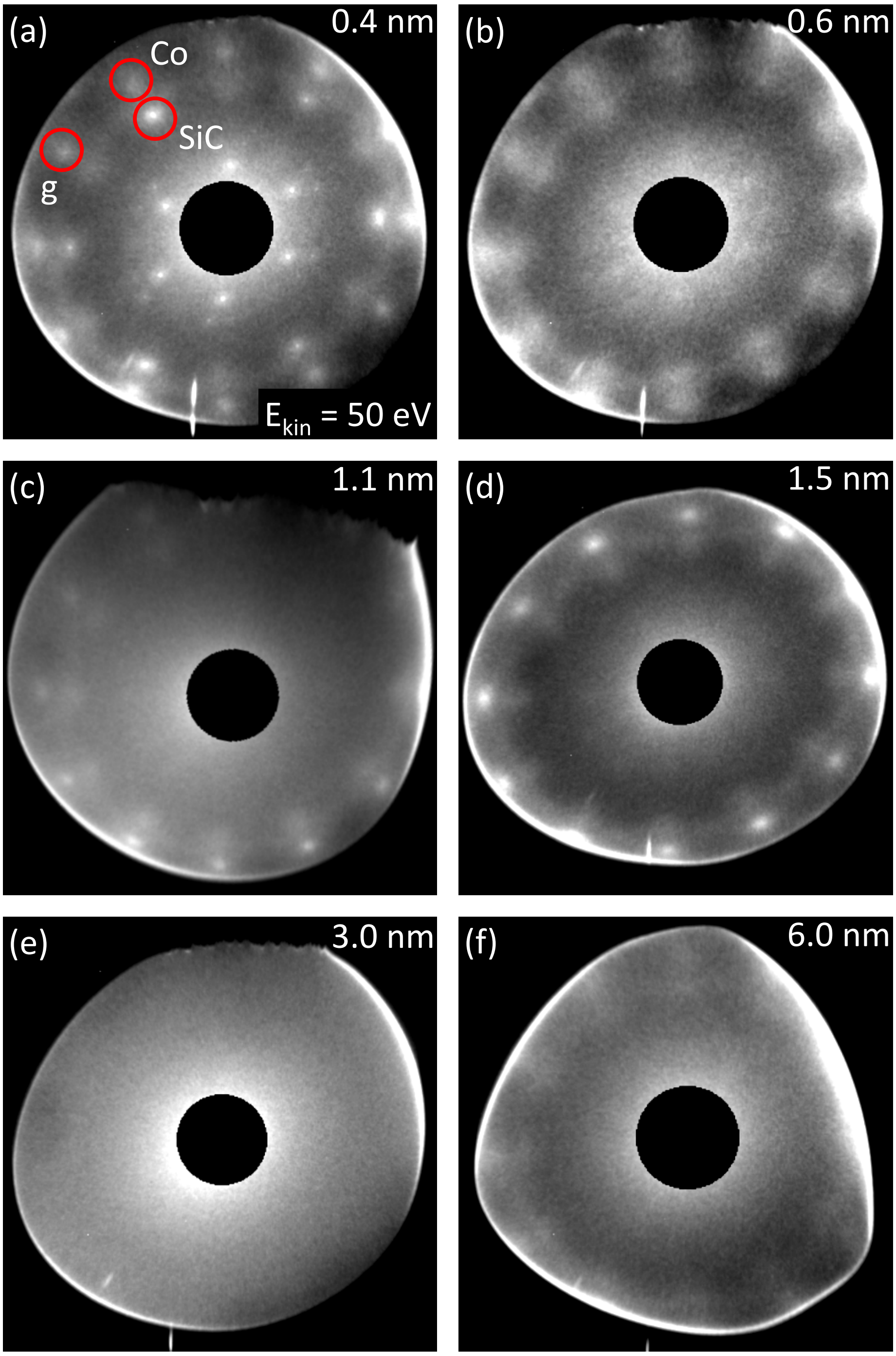

Figure 6.3: LEED patterns taken at $T \approx 200\,^\circ\mathrm{C}$ and $E_{\mathrm{kin}} = 50\,\mathrm{eV}$ after the deposition of 0.4–6.0 nm thick cobalt films on the $6\sqrt{3}$ reconstructed SiC surface. The individual cobalt film thicknesses are indicated in the patterns.

6.5 X-ray photoemission electron microscopy

The combination of PEEM with synchrotron radiation enables the recording of images with chemical and magnetic contrast, as described in section 3.3.2. In the following, these contrast mechanisms are used in order to investigate the chemical and magnetic properties of the as-deposited cobalt films. As for all measurements carried out with the SPELEEM apparatus, the sample temperature during the measurement was set to $\approx 200\,°\mathrm{C}$.

6.5.1 Chemical contrast

To obtain X-PEEM images with chemical contrast, PEEM images at the peak of the Co L_3-edge were recorded for left and right circularly polarized light, respectively. To eliminate potential magnetic contrast, the images corresponding to both polarizations were averaged. In order to enhance the chemical contrast, these average images were divided by images a few eV lower to the absorption edge, which serve as background images. This division enhances the chemical contrast while other contrast mechanisms are suppressed [138, 139], as explained earlier in section 3.3.2. Due to the normalization to the pre-edge background, inhomogeneities of the x-ray beam profile and the detection system of the microscope are also removed from the image. For the sample with $t_{\mathrm{Co}} = 3.0\,\mathrm{nm}$, X-PEEM images in the as-deposited state are not available, because it was annealed before synchrotron radiation was available during the beamtime.

Figure 6.4 displays X-PEEM images with chemical contrast for cobalt film thicknesses of 0.4–6.0 nm. All images display broad white stripes corresponding to the substrate terraces and black narrow lines corresponding to the regions near the step edges. Since the image intensity reflects the spatially-resolved x-ray absorption, the brighter areas correspond to an increased x-ray absorption due to a higher amount of adsorbed cobalt. Therefore, the cobalt coverage on the terraces is higher than at the step edges, for all investigated film thicknesses. The image contrast is homogenous throughout the field of view, therefore the films are homogenous within the 22 nm resolution limit of the SPELEEM. For 1.5 nm and 6.0 nm cobalt coverage, the contrast between the terraces and the step edges is becoming weaker, as evident from the inspection of figures 6.4 (d) and (e), respectively. This indicates that the imbalance of the cobalt coverage in the terrace and step-edge regions decreases for higher film thickness. Since all images qualitatively show the same contrast features, it can be assumed that the growth mode of the cobalt films is similar throughout the investigated film thickness regime. These findings are consistent with the results from the complementary UV-PEEM investigation that were discussed in section 6.2.

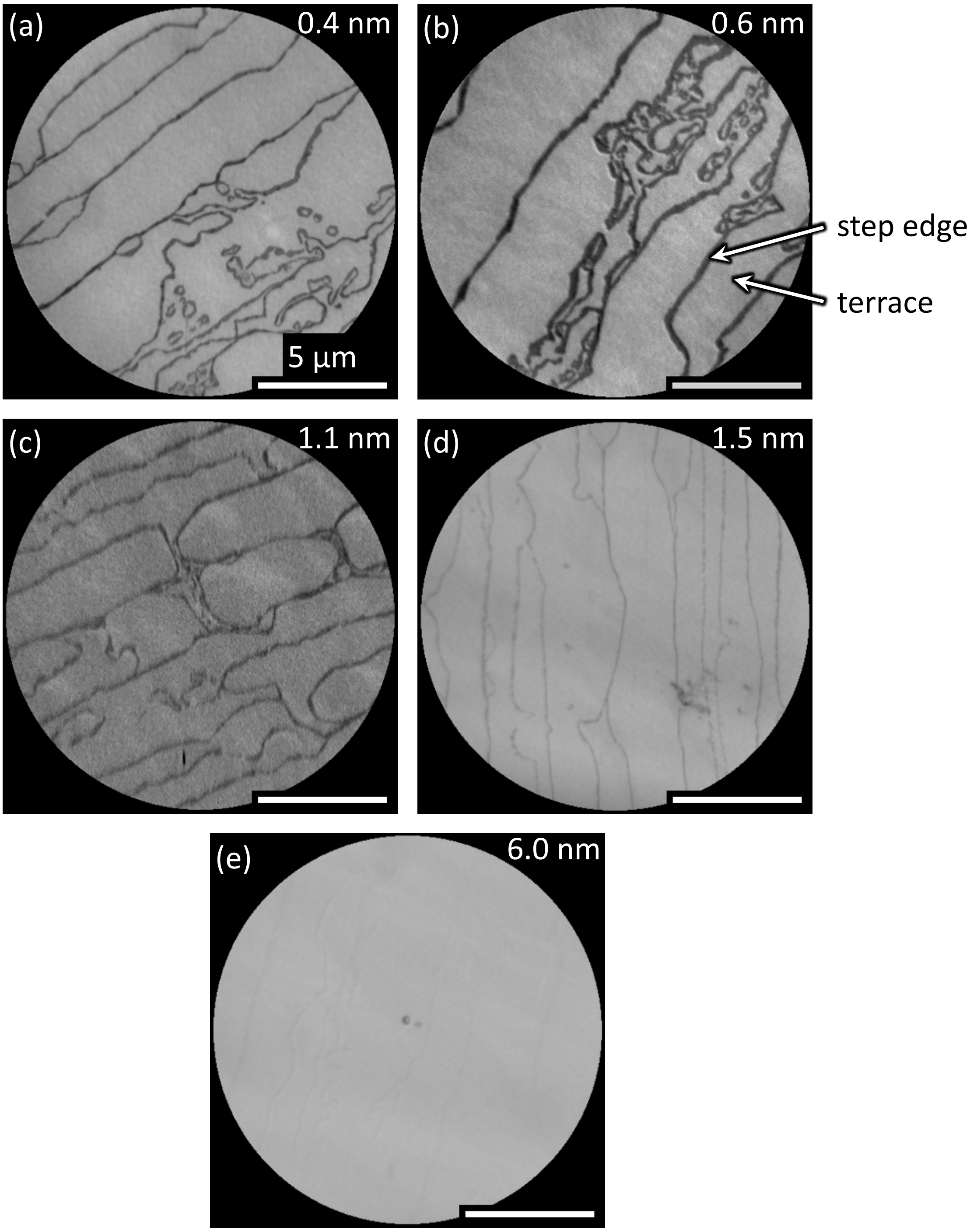

Figure 6.4: X-PEEM images with chemical contrast recorded at the Co L_3-edge of the as-deposited cobalt films with thicknesses of 0.4–6.0 nm. The images were taken at $T \approx 200\,^{\circ}\mathrm{C}$. Bright areas correspond to a relatively high cobalt coverage, whereas dark areas resemble areas with relatively low coverage. The individual cobalt film thicknesses are indicated in the images and the length of the scale bar is 5 µm for all images.

6.5.2 Magnetic contrast

In this section, the magnetic domain structure of the as-deposited cobalt films will be investigated as a function of the cobalt film thickness in the range of 0.4–6.0 nm. The magnetic contrast images were obtained at the peak of the Co L_3-edge, by division of pairs of images acquired with opposite helicity. All measurements were carried out in remanence and without intentionally magnetizing the samples. As for all measurements with the SPELEEM setup, the photon incidence direction was fixed at a grazing angle of 16°. In order to distinguish whether the magnetic easy axis is orientated inside or outside the plane defined by the sample surface, images of the same field of view were recorded before and after an azimuthal rotation of the sample by 90°. Due to the rotation, the relative orientation of the projection of the photon polarization vector and the sample magnetization does only change in the case the sample is magnetized in-plane. For an out-of-plane magnetization, it remains unchanged. Therefore, a contrast change upon sample rotation is solely expected if the magnetization vector is orientated inside the sample plane; if the magnetization would be out-of-plane then no contrast change would be expected [82]. During the image processing, the rotation of the corresponding images was reversed in order to facilitate the comparison of the images corresponding to the same field of view.

In figure 6.5, X-PEEM images with magnetic contrast of samples with cobalt film thicknesses of 0.4–1.1 nm are shown. The bright areas correspond to magnetic domains in that the projection of the magnetization on the axis the photon beam is parallel, whereas an anti-parallel projection leads to the dark areas. Besides these extreme values, all intermediate angles lead to intermediate gray values. For all film thicknesses in figure 6.5 the step structure of the SiC surface is visible, since the strong contrast features introduced by the step edges did not cancel out completely. All images show magnetic contrast throughout the field of view, thus the cobalt film is magnetic in this whole area. By comparing the rotated and not-rotated images for the same field of view, it becomes clear that the magnetization is mostly in-plane since the contrast depends on the incidence direction of the synchrotron radiation.

Figure 6.6 displays the X-PEEM images with magnetic contrast for $t_{\mathrm{Co}} = 1.5$–6.0 nm. Here, solely an image with one photon direction was recorded for each film thickness. The image of the sample with 1.5 nm cobalt film thickness displayed in figure 6.6 (a) shows a diffuse magnetic contrast with only few clearly separated domains. For 3.0 nm cobalt film thickness, no images in the as-deposited state could be recorded, as already mentioned in the previous section. For a film thickness of 6.0 nm, a diffuse magnetization pattern without distinct magnetic domains is observed as shown in figure 6.6 (b). The appearance of the magnetic contrast images thus changes significantly upon further increasing the film thickness. This observation can be

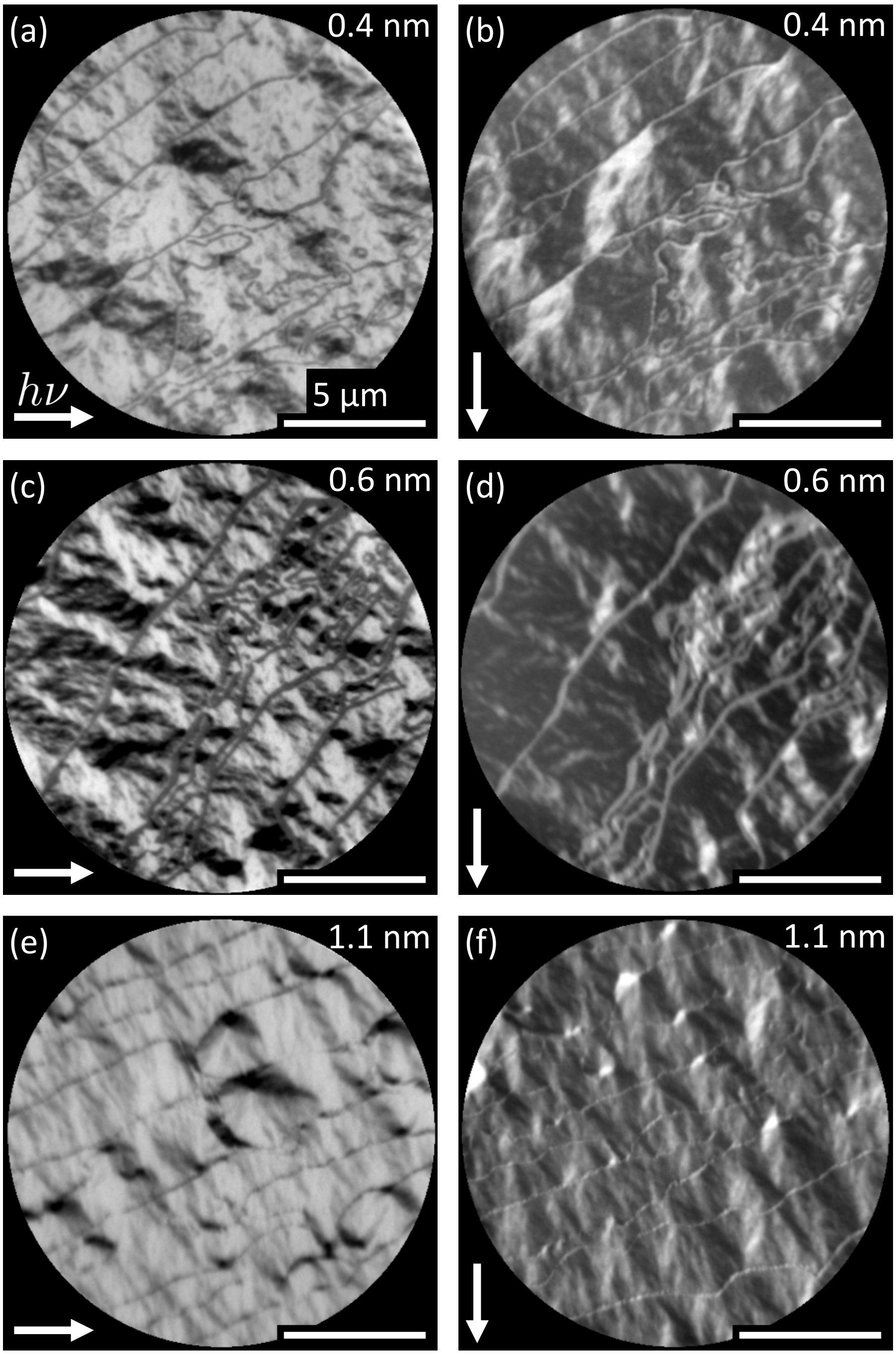

Figure 6.5: X-PEEM images with magnetic contrast recorded at the Co L_3-edge of the as-deposited cobalt films with thicknesses of 0.4–1.1 nm. The images were taken at $T \approx 200\,^{\circ}\mathrm{C}$. The individual film thicknesses are indicated in the images and the arrows denote the incidence direction of the synchrotron radiation. The scale bar is 5 µm for all images.

related to film stress due to the cobalt deposition at room temperature. As already revealed by the LEED results, a higher film thickness is associated with a lower crystalline quality. Thus, the absence of an ordered magnetic domain pattern is consistent with the LEED measurements for high thickness.

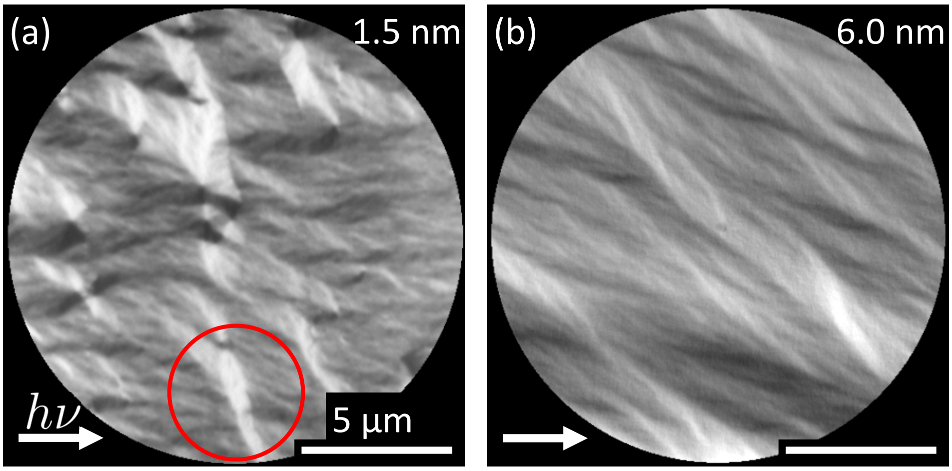

Figure 6.6: X-PEEM images with magnetic contrast recorded at the Co L_3-edge of the as-deposited cobalt films with thicknesses of 1.5 nm and 6.0 nm. The images were taken at $T \approx 200\,°C$. The individual film thicknesses are indicated in the images and the arrows denote the incidence direction of the synchrotron radiation. The circle in figure (a) marks a characteristic domain feature for comparison with the annealed samples that are to be discussed in chapter 7. The scale bar is 5 µm for all images.

6.6 Summary

Using UV-PEEM, XPS, LEED, and X-PEEM, the structural, chemical, and magnetic properties of the $6\sqrt{3}$ reconstructed SiC samples after deposition of different cobalt film thicknesses t_{Co} in the range of 0.4–12 nm were analyzed. The UV-PEEM experiment revealed that the cobalt adsorbs preferentially at the $6\sqrt{3}$ covered terraces instead of the graphene monolayer-covered stripes for all investigated film thicknesses. The XPS spectra showed that the chemical states of the carbon and silicon atoms remain unchanged after the deposition of the cobalt film, indicating that no reaction occurs at room temperature. The LEED patterns for $t_{\mathrm{Co}} \leq 1.5\,\mathrm{nm}$ prove that the cobalt films are crystalline, though the diffraction patterns were distorted by streak-like features. For thicker films barely any diffraction pattern could be observed, which results from the fact that the low substrate temperature during the deposition process led to stress in the deposited film. Finally, X-PEEM data taken at the Co L-edge with chemical and magnetic contrast were discussed. The chemical contrast images confirmed that the cobalt atoms adsorb preferentially at the $6\sqrt{3}$ areas rather than the graphene areas. Magnetic contrast was observed for all investigated film thicknesses, however, for higher film thickness only a distorted magnetization pattern was observed, which is attributed to film stress as already implicated by the LEED measurements. The magnetic contrast images for thin films with $t_{\mathrm{Co}} \leq 1.5\,\mathrm{nm}$ revealed an in-plane magnetic easy-axis, as deduced from angle-dependent measurements.

In conclusion, no evidence for the start of an intercalation process was found in this chapter. This enables a controlled investigation of the chemical reaction of the cobalt film with the underlying substrate at elevated temperature, which will be carried out in the following chapter.

7 Thermally-induced cobalt intercalation

The investigation that was carried out in the previous chapter did not reveal any chemical reaction of the as-deposited cobalt films with the $6\sqrt{3}$ reconstructed silicon carbide surface. The purpose of this chapter is to analyze the changes that occur to the sample system during a controlled annealing procedure. As a first step, UV-PEEM is used in order to reveal at which temperature values relevant changes occur. Using this information XPS, LEED, and X-PEEM measurements will be carried out. These methods will reveal, whether the $6\sqrt{3}$ reconstructed carbon layer converts into an intercalated graphene layer, whether any reaction at the Co/SiC interface occurs, and what the magnetic properties of the cobalt films are after the annealing process.

7.1 Ultraviolet photoemission electron microscopy

7.1.1 Temperature and film thickness dependence

In this section, the reaction of cobalt films with film thicknesses of $t_{\mathrm{Co}} = 0.4$–$12\,\mathrm{nm}$ and the $6\sqrt{3}$ reconstructed SiC surface is investigated using UV-PEEM, whose work function contrast is highly sensitive for any change in structural and chemical properties of the surface. All images were acquired with the PEEM apparatus at TU Dortmund, described in section 4.4.1. The sample temperature was increased stepwise up to 600 °C with an average heating rate of about 5 °C/ min. The sample temperature was measured with an infrared pyrometer with the emissivity set to 83 % [140]. For simplicity, the slight temperature dependence of the emissivity was neglected. Throughout the annealing process, UV-PEEM images were recorded at time intervals of approximately 20 s in order to reveal the temperature points at which significant structural or chemical changes occur.

The key finding is that two successive contrast inversions occur during the annealing procedure, for all investigated film thicknesses. The temperatures at which these inversions occur depend on the cobalt film thickness, as will be discussed below. The UV-PEEM images taken after the first contrast inversion are displayed in figure 7.1. They should be compared with those taken in the as-deposited state that were discussed in section 6.2.

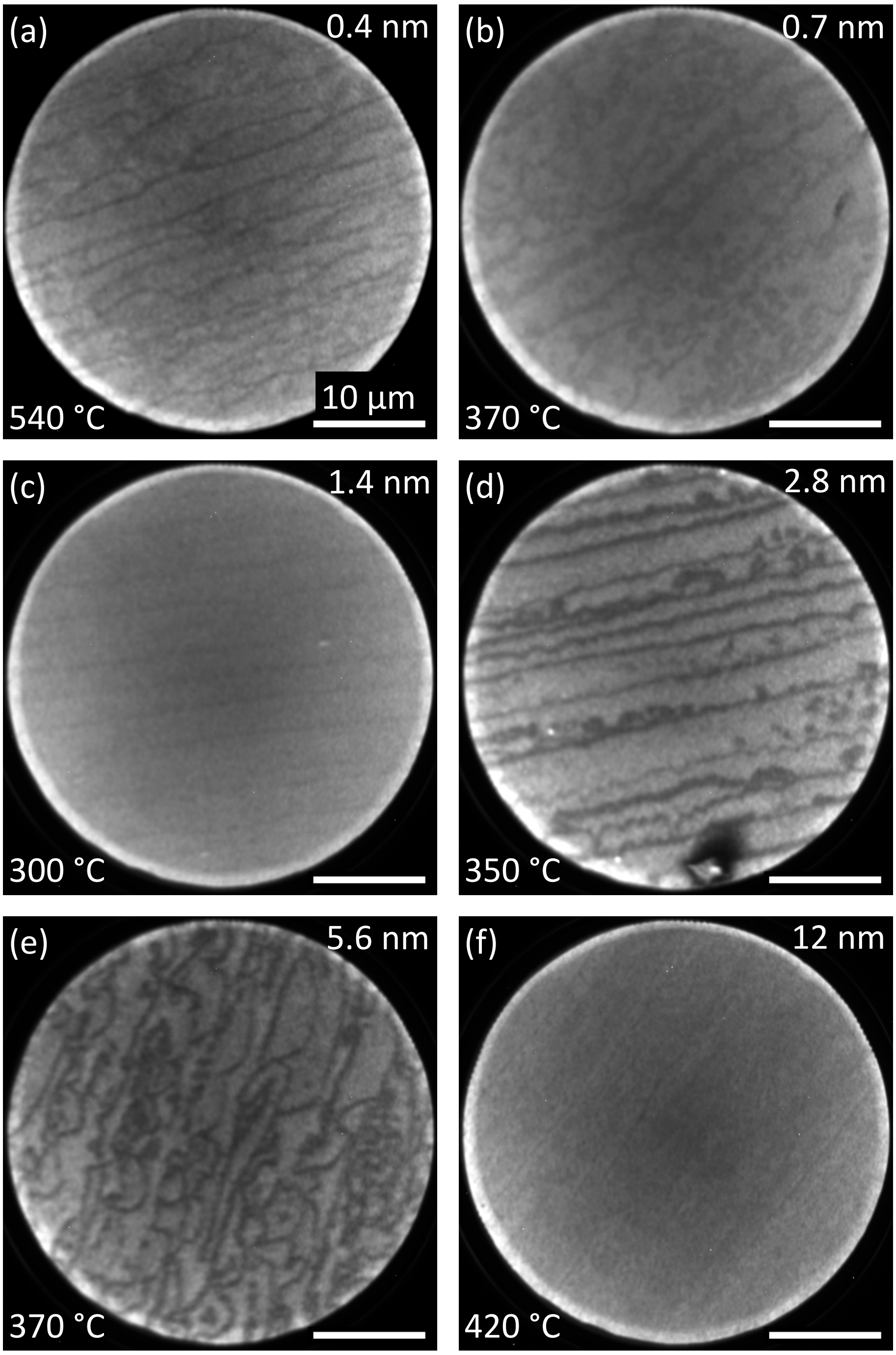

Figure 7.1: UV-PEEM images recorded after the first contrast inversion that occurred during the annealing procedure. The sample temperatures during imaging and the individual cobalt film thicknesses are indicated in the images. UV-PEEM images of the as-deposited state of the same samples were displayed in figure 6.1 and should be regarded for comparison.

The increased intensity of the terraces in figure 7.1 is due to a decrease of the terrace work function. Besides the relative work function of the terraces with respect to the steps, also its absolute value has decreased. This is evident from the need to significantly reduce the image intensifier gain during the acquisition from the beginning to the end of the annealing process, usually by a factor of 8. An explanation for the work function decrease is an increase of the size of the cobalt nanocrystallites, since it has been shown previously that the ionization potential of cobalt clusters decreases with increasing size [141]. Upon further annealing, the intensity emitted from the terraces decreases and eventually the contrast inverts again. The PEEM images acquired after this second contrast inversion are displayed in figure 7.3. For comparison, the images taken in the as-deposited state that were discussed in section 6.2 should be regarded. A high work function of the terraces is consistent with the lifting of the $6\sqrt{3}$ reconstruction and a formation of a free-standing graphene film [116]. These two characteristic contrast inversions were observed for all investigated film thicknesses, therefore it is assumed that they result from a common mechanism.

As already mentioned above, the temperatures T_1 and T_2 at which the first and second contrast inversions occur depend on the cobalt film thickness t_{Co}. Here, the contrast inversion temperatures are defined as the sample temperature at that the intensity emitted from the terraces and the step-rich regions is equal. That is, the contrast inversion temperatures correspond to a PEEM image in that the contrast has completely vanished. In figure 7.2, the temperatures T_1 and T_2 are plotted as a function of the film thickness.

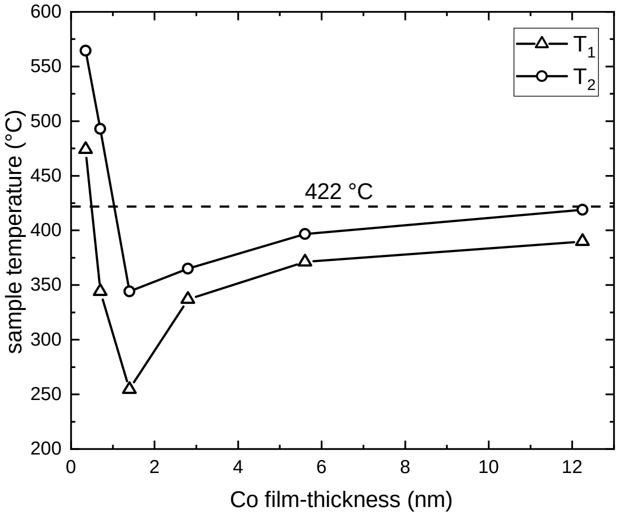

Figure 7.2: The temperatures T_1 and T_2 of the first and second UV-PEEM contrast inversion, respectively, as a function of the cobalt film thickness.

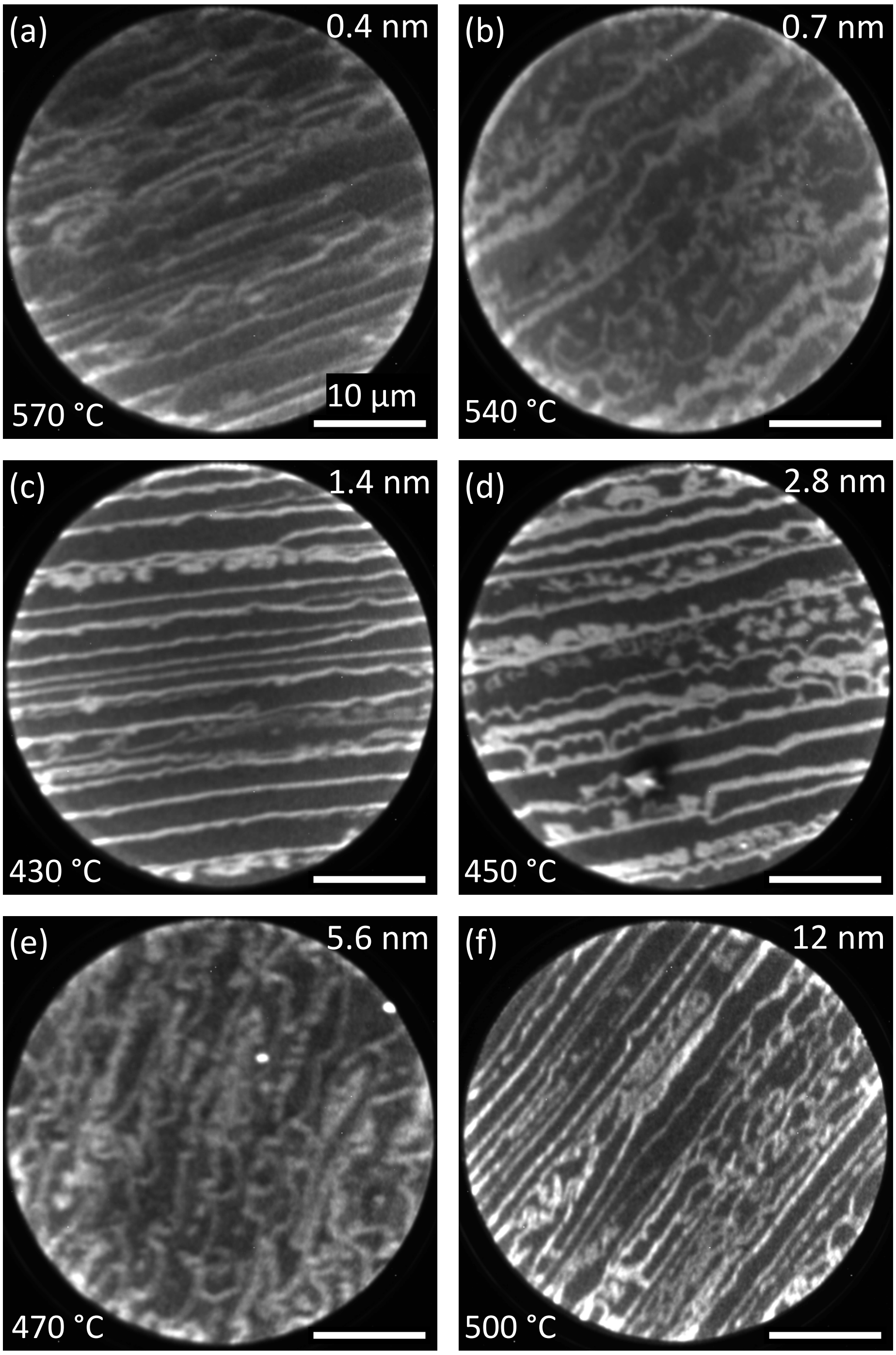

Figure 7.3: UV-PEEM images recorded after the second contrast inversion that occured during the annealing procedure. The sample temperatures during imaging and the individual cobalt film thicknesses are indicated in the figures. These images should be compared with those recorded after the first contrast inversion and in the as-deposited state, that are displayed in figures 7.1 and 6.1, respectively.

Both curves in figure 7.2 show a similar trend with minima for $t_{\mathrm{Co}} = 1.4\,\mathrm{nm}$. For lower film thicknesses, both temperatures increase greatly. The highest measured temperature is $T_2 = 570\,^{\circ}\mathrm{C}$ for $t_{\mathrm{Co}} = 0.4\,\mathrm{nm}$. This film thickness is equal to about two atomic monolayers of cobalt in hcp structure; for sub-monolayer cobalt film thickness, intercalation temperatures of 650–850 °C [35, 36] were previously reported using a single layer graphene on SiC as a substrate. Note that in references [35, 36] a single layer graphene on silicon carbide was used as a substrate, whereas in the present work the bare $6\sqrt{3}$ reconstruction is being investigated. However, the temperature of the second contrast inversion for low film thickness is consistent with the reported cobalt intercalation temperatures. This indicates that the second contrast inversion may be associated with the intercalation of cobalt. The lowest temperature at which the second contrast inversion was observed is $T_2 = 340\,^{\circ}\mathrm{C}$ for $t_{\mathrm{Co}} = 1.4\,\mathrm{nm}$.

For $t_{\mathrm{Co}} \geq 1.4\,\mathrm{nm}$, the slopes of the temperature curves are smaller. Remarkably, T_2 converges to a value close to $T_2 = 422\,^{\circ}\mathrm{C}$ which is the fcc-hcp phase transition temperature of bulk cobalt [136]. Thus, a correlation of the second contrast inversion and the phase transition seems likely for the samples with high film thickness. Interestingly, the solubility of carbon in cobalt increases during the hcp-fcc transition [142], therefore it may be speculated that the phase transition promotes the intercalation process due to an enhanced carbon segregation to the surface.

7.1.2 Real-time imaging

To gain further insight into the contrast inversions, the real time image capability of PEEM was used. Concerning the first contrast inversion, it was found that the emitted intensity always changes uniformly throughout a terrace. Thus, the changes occur on a length scale that is below the resolution of the employed PEEM optics that is about 0.2 µm. More interestingly, the second contrast inversion involves distinct diffusion fronts.

In figure 7.4, images taken during the second contrast inversion are displayed for $t_{\mathrm{Co}} = 5.6\,\mathrm{nm}$. The sample temperature was held constant at 395 °C. The total time elapsed during all images in the figure is about 12 min. Starting with figure 7.4 (a), the terraces are bright and the step edges are dark, as usual before the second contrast inversion. Subsequently, in the next images, the terraces start to convert into dark regions, starting from the step edges. The conversion process can thus be laterally resolved and the step edges are clearly involved in the process.

Figure 7.5 displays images taken during the second contrast inversion for $t_{\mathrm{Co}} = 11\,\mathrm{nm}$. Clearly, the mechanism is similar as for the previous sample. Since the step edge pattern is more parallel as for the 5.6 nm sample, here the visibility of the

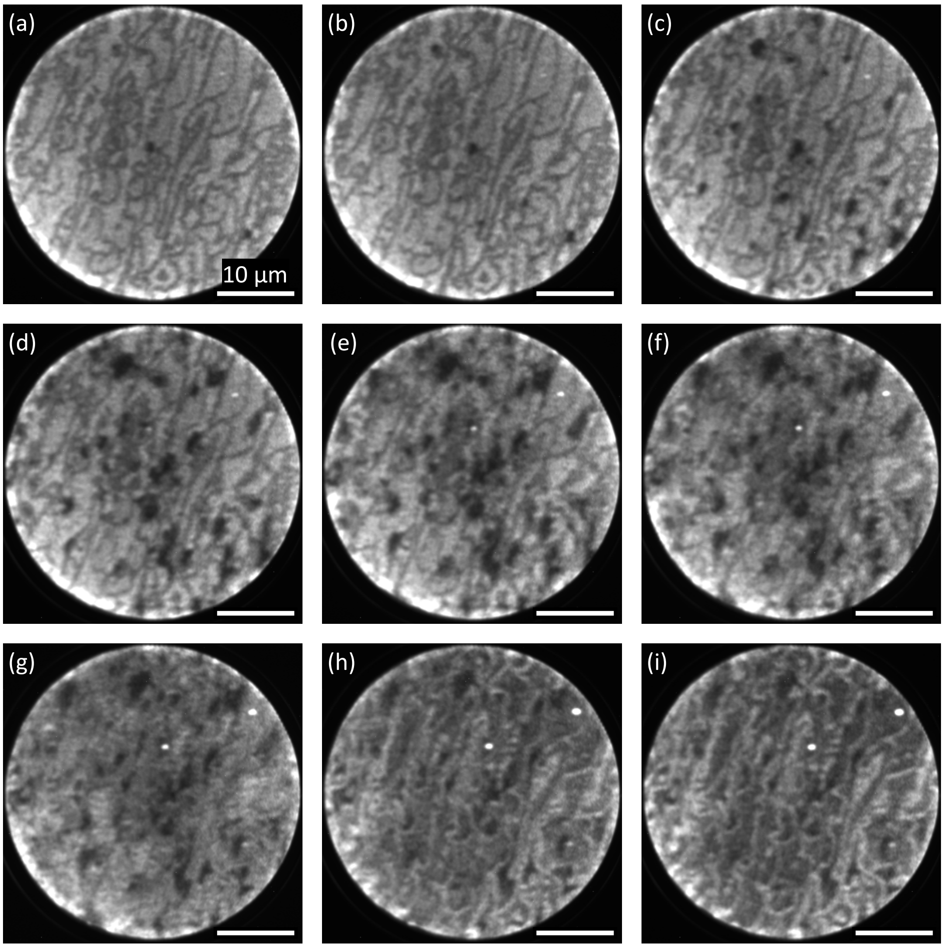

Figure 7.4: Series of PEEM images recorded during the second contrast inversion. The cobalt film thickness is 5.6 nm, the sample temperature is 395 °C, and the total time elapsed is 12 min.

diffusion fronts at the step edges is more pronounced. The temperature was $T = 400\,^\circ\mathrm{C}$, which is about 20 °C lower than expected by comparison with the data in figure 7.2. Possible reasons for the deviation are an experimental uncertainty of the temperature measurement or the base pressure that was only for this particular sample 2×10^{-9} mbar instead of the routinely achieved 1×10^{-10} mbar. This might have caused a minor contamination and thus the different reaction temperature.

It was found that the duration of the second contrast inversion decreases for thinner films. For the thinnest films with $t_{\mathrm{Co}} \leq 2.8\,\mathrm{nm}$, the duration of the second contrast inversion was too short to image the diffusion process. Only for the film thicknesses corresponding to figures 7.4 and 7.5, the intercalation process was sufficiently slow in order to capture it during an acceptable acquisition time.

The PEEM images shown in figures 7.4 and 7.5 resemble those obtained for other intercalants and graphene substrates [48]. More importantly, the PEEM images displayed in figures 7.4 and 7.5 are similar to the low-energy electron microscopy images presented in reference [26] obtained during intercalation of germanium underneath $6\sqrt{3}$ reconstructed SiC. It was found that the intercalation of germanium starts at the step edges of the $6\sqrt{3}$ reconstructed surface and continues over the terraces. This similarities indicate an association of the second contrast inversion with a cobalt intercalation process.

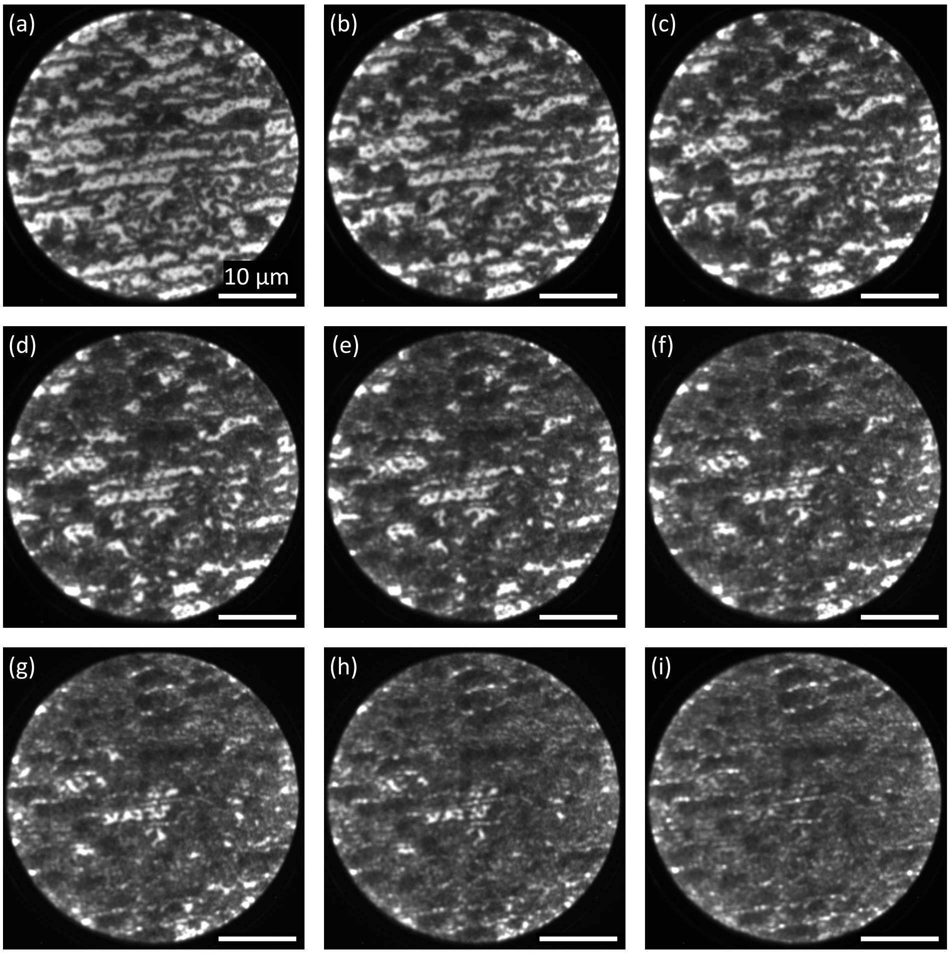

Figure 7.5: Series of PEEM images recorded during the second contrast inversion. The cobalt film thickness is 11 nm, the sample temperature is 400 °C, and the total time elapsed is 10 min.

The starting of the intercalation at the step edges is one out of two frequently observed intercalation mechanisms for $6\sqrt{3}$ reconstructed SiC and for other intercalants and graphene substrates. Reference [48] proposed that the step edge mechanism occurs for elements that have a low reactivity towards graphene and leaves the graphene film intact. The second mechanism involves homogeneous intercalation over the whole terrace and is associated with a high reactivity towards graphene, which leads to defects in the graphene layer through which the intercalant diffuses. Hydrogen is an example for an element that exhibits the second mechanism during intercalation underneath $6\sqrt{3}$ reconstructed SiC [49].

In the next section, XPS measurements for low and high film thicknesses will confirm whether the $6\sqrt{3}$ reconstructed surface is converted into a graphene-covered surface.

7.2 Photoelectron spectroscopy

The chemical states of a $6\sqrt{3}$ reconstructed carbon layer and a graphene layer are clearly distinguishable as the carbon atoms in the $6\sqrt{3}$ structure are partially sp^3-hybridized, whereas the graphene layer is fully sp^2-hybridized. These different hybridizations give rise to two broad, or one sharp component in the C 1s XPS spectrum for the $6\sqrt{3}$ reconstruction and the graphene layer, respectively. Moreover, the binding energy of the graphene component is significantly lower than that of the $6\sqrt{3}$ components. XPS therefore allows to reveal whether the $6\sqrt{3}$ reconstructed surface is converted into a graphene-covered surface. Furthermore, the analysis of the Si 2p spectra will show whether a cobalt silicide compound forms during annealing; note that in the as-deposited state no silicide formation was observed.

In this section, two samples with a cobalt film thickness of 0.4 nm and 2.8 nm will be analyzed. The spectra presented in this section should be compared with those taken in the as-deposited state that were discussed in section 6.3.

7.2.1 Low cobalt film thickness

In this section, the discussion of the sample with a cobalt film thickness $t_{\mathrm{Co}} = 0.4\,\mathrm{nm}$ that was started in section 6.3 is continued. Three annealing steps for 5–10 min at temperatures of 450–650 °C were applied to the sample. The sample temperature was measured with an infrared pyrometer with the emissivity set to 83 %. After each step, the shape of the C 1s core level spectrum was checked, revealing a decrease of the relative intensity of the SiC-related spectral component in favor of the $6\sqrt{3}$ and graphene related components. The difference was largest for the first annealing step and only a small change was observed for the last step, indicating the completion of the annealing process. The annealing procedure was terminated at the 650 °C step, because the results presented here should be compared to the UV-PEEM results for which at no time a higher temperature was used. In particular, this temperature is sufficient to ensure that the second UV-PEEM contrast inversion would have occurred for this film thickness, according to figure 7.2.

Figures 7.6 (a) and (b) display survey spectra taken with $h\nu = 650\,\mathrm{eV}$ for $\theta = 0°$ and $\theta = 60°$. Both spectra are normalized to the maximum of the C 1s core-level. For both spectra, the C 1s to Co 3p intensity ratio is higher than for the as-deposited state. Therefore, a carbon-enrichment of the surface has occurred. However, the Co 3p intensity increased slightly for $\theta = 60°$. Instead, for a fully carbon-terminated surface one would expect that the Co 3p intensity decreases. This leads to the assumption that the intercalation process took place only partial.

Figures 7.6 (c) and (d) display high-resolution C 1s XPS spectra recorded at $h\nu = 600\,\mathrm{eV}$ for $\theta = 0°$ and $\theta = 60°$. Four components are necessary for a sufficient fit the spectrum, like in the as-deposited state. The fit parameters are shown in table 7.1. By comparing the spectra with those recorded in the as-deposited state, it becomes clear that the relative intensity of the graphene-like component is increased. The increased graphene component at the expense of the S2 component is an evidence for transformation of the $6\sqrt{3}$ reconstruction into a graphene layer. However, the S2 and S1 components persist, as well as the SiC component. Therefore, the $6\sqrt{3}$ reconstructed surface is only partially transformed into a graphene-covered surface. Since the amount of deposited cobalt would be sufficient for a full substitution of the $6\sqrt{3}$ bonding to the topmost silicon layer, it is obvious that only a part of the total number of cobalt atoms took part in the intercalation process.

The high-resolution Si 2p photoelectron spectra taken after the annealing of the cobalt film are displayed in figures 7.6 (e) and (f). The fit parameters are shown in table 7.1. The $6\sqrt{3}$ component is no longer needed for a sufficient fit. Consequently, this component was omitted from the fit. A strong new component at the higher kinetic energy side of the SiC component referred to as CoSi evolves in the spectrum. According to a study of the reaction of cobalt with the $\left(\sqrt{3} \times \sqrt{3}\right)$-R30° reconstructed SiC surface, a component at higher kinetic energy results from cobalt silicide [132]. Due to the fixed energy position and width for the $\theta = 0°$ and $\theta = 60°$ spectra, a slight imprecision of the $\theta = 60°$ spectrum is observed. It likely results from a variation of the relative intensity of an unresolved Co 3s component with respect to the $\theta = 0°$ spectrum. The Co 3s photoelectrons are expected to possess about the same kinetic energy as the Si 2p photoelectrons, as already mentioned in section 6.3.

The kinetic energy of the CoSi component amounts to 76.32 eV. In order to translate this into a binding energy, the chemical shift to the SiC bulk component of the pristine SiC sample recorded before cobalt deposition can be used. Note that the Schottky barrier at the Co/SiC interface induces a binding energy shift. For this reason it is not meaningful to compare the binding energy reported in literature for pristine SiC samples to that of the cobalt-deposited sample discussed here. In the Si 2p spectrum of the pristine SiC sample discussed in section 5.4 the bulk component appeared at the kinetic energy of 74.33 eV. Thus, the kinetic energy difference of the CoSi component and the SiC component of the reference sample is 1.99 eV. Further, an average of the reported values for the binding energy of the SiC bulk component is 101.50 eV [119, 121]. As a result, component CoSi yields a binding energy of 99.51 eV.

Reference [143] reports XPS binding energies in the range of 98.94–99.58 eV corresponding to four different cobalt silicide compounds. Of these, that for a stochiometry of cobalt and silicon of 1:1 fits best to the result obtained here. The observation of this particular stochiometry upon reaction of cobalt and SiC surfaces is consistent with previous reports [144, 145].

Another small component called X with a kinetic energy of 75.64 eV is also necessary for a good fit. It is not immediately clear whether this is a Co 3s peak or a Si 2p component resulting from a cobalt silicide compound of a different stoichiometry as the component CoSi. As already mentioned in the discussion of the as-deposited state, the binding energy of the Co 3s peak is almost identical to that of the bulk SiC component. In this spectrum, the component X is slightly shifted to that observed in the as-deposited state which could in principle be attributed to a chemical shift which is expected in the Co 3s spectrum as well as a result of the silicide formation. However, the fact that a doublet component fits better than a singlet component supports the interpretation that this component results from an additional CoSi structure, as for a Co 3s peak a singlet component would fit better.

The structure of the carbon-terminated $\left(6\sqrt{3} \times 6\sqrt{3}\right)$-R30° surface reconstruction discussed in section 2.1.3 suggests that the formation of cobalt silicide must be linked to the penetration of the first carbon layer. It may be concluded that the cobalt atoms substitute the carbon atoms of the $6\sqrt{3}$ reconstruction that were bonded to the topmost silicon atoms leading to a transformation of the $6\sqrt{3}$ reconstructed carbon layer into a graphene layer that subsequently is intercalated by the remainder of the cobalt film. In the literature, this process is commonly called the decoupling of the so-called buffer layer, which is a synonym for the $6\sqrt{3}$ reconstruction. The formation of metal silicides after metal intercalation has been observed previously, for instance in the case of gold intercalation [25]. Consequently, the silicide formation can be used as an indicator for successful intercalation.

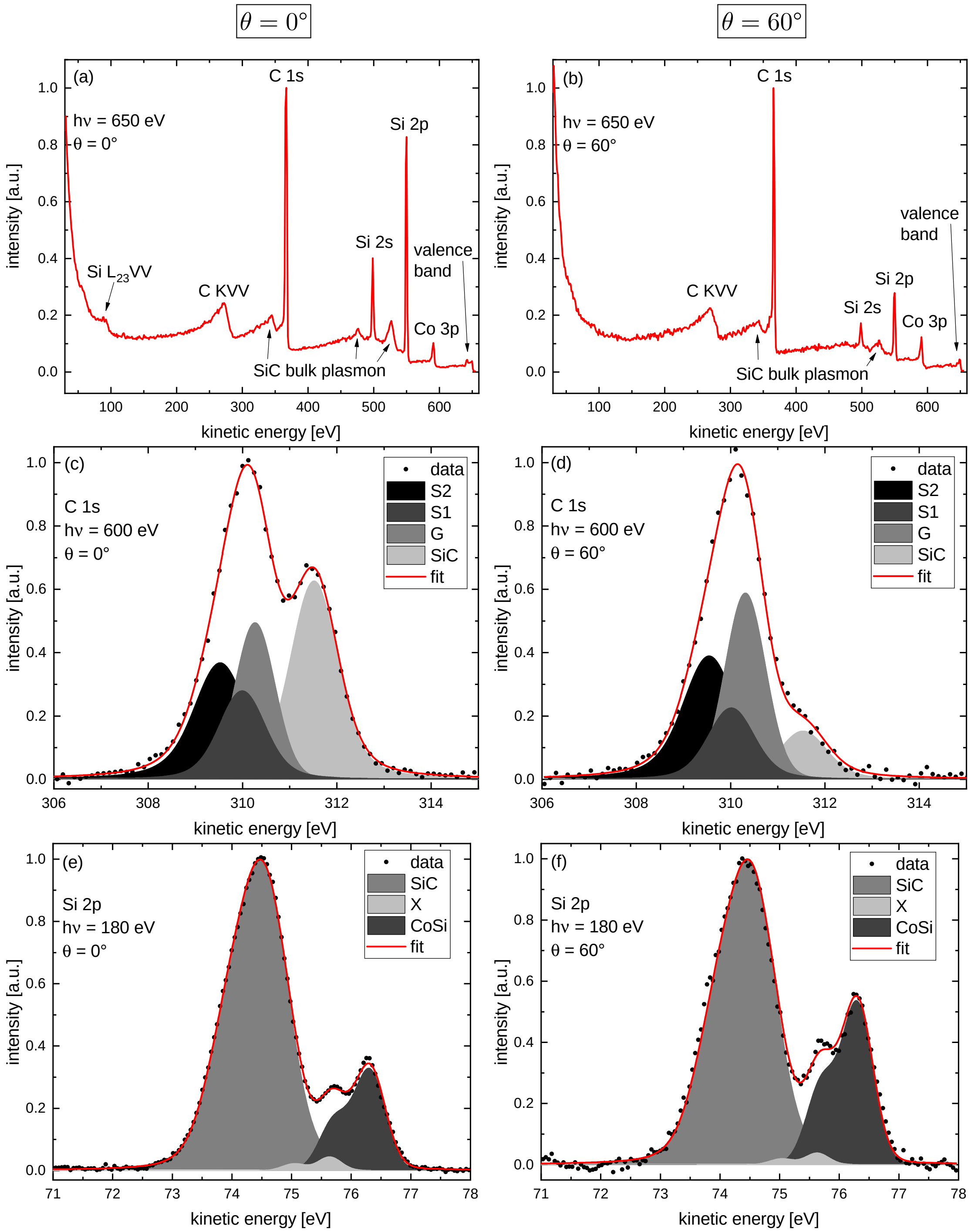

Figure 7.6: XPS spectra for $\theta = 0°$ and $\theta = 60°$ of a sample with $t_{\mathrm{Co}} = 0.4\,\mathrm{nm}$: survey spectra (a), (b); high-resolution C 1s spectra (c), (d); and high-resolution Si 2p spectra (e), (f).

Table 7.1: Parameters of the peak fitting procedure applied to the spectra displayed in figure 7.6: kinetic energy E_{kin}, relative kinetic energy with respect to the bulk component ΔE_{kin}, relative intensity I, and full width at half maximum w.

		$\theta = 0°$				$\theta = 60°$			
peak	comp.	E_{kin}/eV	ΔE_{kin}/eV	A/%	w/eV	E_{kin}/eV	ΔE_{kin}/eV	A/%	w/eV
C 1s	SiC	311.52	0.00	37	1.20	311.54	0.00	12	1.20
	G	310.28	-1.23	22	0.99	310.30	-1.23	36	1.00
	S1	309.99	-1.52	16	1.16	310.01	-1.52	17	1.16
	S2	309.53	-1.99	25	1.33	309.55	-1.99	35	1.33
Si 2p	SiC	74.58	0.00	53	0.93	74.57	0.00	48	0.93
	X	75.64	1.06	1	0.46	75.63	1.06	1	0.47
	CoSi	76.32	1.74	12	0.60	76.31	1.74	18	0.60

Interestingly, until now it has been assumed that the $6\sqrt{3}$ reconstructed SiC(0001) surface prevents the formation of cobalt silicide [131]. The contradiction to reference [131] is most likely due to the different surface sensitivities of both studies resulting from different kinetic energies of the photoelectrons due to different photon energies used in that XPS study. In fact, here, it is clearly revealed that a silicide reaction occurs. Remarkably, also for the intercalation of cobalt underneath monolayer graphene on silicon carbide, two separate studies found that no silicide formation [35, 36] occurs. Note that a monolayer graphene on SiC is defined as a monolayer of graphene on top of $6\sqrt{3}$ reconstructed SiC, as discussed in section 2.1.3. These results indicate that either the cobalt intercalation mechanism on $6\sqrt{3}$ reconstructed silicon carbide is different from the intercalation underneath monolayer graphene on SiC, or that the lower film thickness in the above-mentioned studies than that investigated here led to a different mechanism. In this study, the lowest investigated film thickness is 0.4 nm, which corresponds to approximately two monolayer of cobalt, assuming cobalt in bulk hcp structure. In contrast, only sub-monolayer amounts were used in references [35, 36].

A review of the literature concerning the Co/SiC interface reveals that the reaction of cobalt with amorphous SiC or the unreconstructed silicon-rich SiC(0001)-(1 × 1) surface may lead to the formation of cobalt silicide along with graphite [144, 145]. On the other hand, for the $\left(\sqrt{3} \times \sqrt{3}\right)$-R30° reconstructed SiC(0001) surface, which is more carbon-rich than the (1 × 1) surface, it has been found that the reaction of cobalt and silicon carbide is self-limited [132]. This trend indicates that the amount of reacted cobalt should be even lower in the case of the $\left(6\sqrt{3} \times 6\sqrt{3}\right)$-R30° reconstruction that is even more carbon-rich [42]. The low reacted amount of cobalt accounts for the absence of any detectable silicide formation in reference [131]. Also for other adsorbates, a dependence of the amount of reacted adsorbate on the type of surface reconstruction of SiC(0001) has been observed previously. For instance, reference [146] reports on the reaction of platinum with various SiC(0001) surface reconstructions. Therein, it is shown that the amount of reacted platinum decreases for the more carbon-rich surface reconstructions.

7.2.2 High cobalt film thickness

In order to correlate the second of the previously-discussed UV-PEEM contrast inversions with the chemical state of the carbon atoms, a sample with 2.8 nm cobalt has been prepared in the UV-PEEM apparatus. The second UV-PEEM contrast inversion had occurred and the maximum annealing temperature that was applied to the sample is 540 °C. The UV-PEEM results of this sample have been discussed in section 7.1.1. Then, the sample has been extracted from the PEEM apparatus and immediately transferred to the XPS chamber.

Survey spectra have been taken at a photon energy of $h\nu = 650\,\mathrm{eV}$ for $\theta = 0°$ and $\theta = 60°$ before and after mild degassing at 300 °C for 5 min. The results after degassing are depicted in figures 7.7 (a) and (b). The C 1s, Si 2s, Si 2p, and Co 3p peaks can be clearly resolved and despite the sample transport in air, barely any O 1s signal can be recognized. The dominance of the C 1s peak proves a carbon-rich surface, indicating the segregation of carbon through the cobalt overlayer. The heights of silicon signals relative to the carbon signal are suppressed compared to the reference sample, due to the carbon-enrichment of the surface.

High-resolution spectra of the C 1s orbital have been recorded at $h\nu = 600\,\mathrm{eV}$ and displayed in figures 7.7 (c) and (d), in order to resolve the chemical state of the carbon atoms. The peak fitting procedure revealed that the components S2, S1, and SiC that were necessary to fit the C 1s spectrum in the as-deposited were not required for this spectrum. Solely one component with $w = 1.06\,\mathrm{eV}$, consisting of Doniach-Sunjic profile with an asymmetry parameter of $\alpha = 0.08$ convoluted with a Gaussian, is sufficient for an excellent fit to the spectrum. The kinetic energies of the fit component are 310.83 eV and 310.77 eV for $\theta = 0°$ and $\theta = 60°$, respectively. The usage of the Doniach-Sunjic profile is motivated by the metallic character of the graphene film [24, 147].

Since only one asymmetric fit component remains, it can be stated that all carbon atoms at the sample surface are in the sp^2-hybridized state. This is characteristic for a graphene-covered surface. Hence, the former $6\sqrt{3}$ reconstructed surface has been converted into a graphene-covered surface after annealing of the cobalt film at a temperature that is sufficient to trigger the second UV-PEEM contrast inversion. This complete transformation of the $6\sqrt{3}$ related XPS components into one single asymmetric component has been observed previously in the case of germanium intercalation [26].

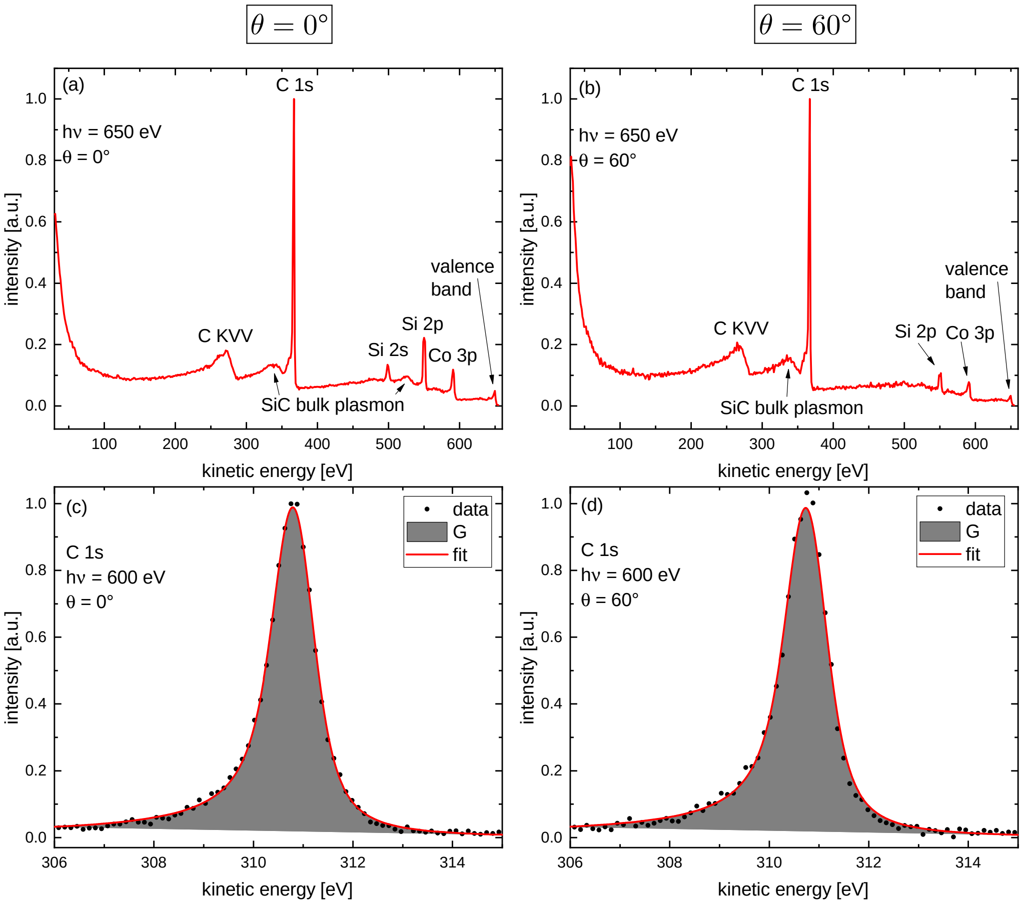

Figure 7.7: Survey spectra for (a) $\theta = 0°$ and (b) $\theta = 60°$ taken with $h\nu = 650\,\mathrm{eV}$ of a sample with 2.8 nm cobalt after annealing in the UV-PEEM apparatus. High-resolution C 1s spectra for (c) $\theta = 0°$ and (d) $\theta = 60°$ taken with $h\nu = 600\,\mathrm{eV}$.

In summary, a complete transformation of the $6\sqrt{3}$ covered surface into a graphene covered surface was revealed for $t_{\mathrm{Co}} = 2.8\,\mathrm{nm}$, while the $6\sqrt{3}$ surface transformed only partially for $t_{\mathrm{Co}} = 0.4\,\mathrm{nm}$. A cobalt silicide interface forms upon annealing and, in particular, the $6\sqrt{3}$ reconstruction does not prevent the cobalt from reacting with the silicon, as observed for $t_{\mathrm{Co}} = 0.4\,\mathrm{nm}$.

The following sections present LEED and X-PEEM measurements that were carried out with the SPELEEM experiment at SPring-8.

7.3 Sample preparation at the SPELEEM experiment

In section 7.1, two characteristic UV-PEEM contrast inversions have been observed for all investigated cobalt film thicknesses. The findings shown so far indicate that the second of these is likely related to the transformation of the $6\sqrt{3}$ reconstructed surface into an intercalated graphene film. In the following sections, the sample properties after the second contrast inversion will be further investigated in order to verify whether the second contrast inversion is associated with the intercalation. The data in the following sections were acquired with the SPELEEM apparatus at SPring-8. As described in section 6.1, samples with cobalt film thicknesses comparable to those used for the PEEM experiment at TU Dortmund were prepared for the SPELEEM experiment.

At the SPELEEM experiment a similar annealing procedure as that described in section 7.1 was carried out. In particular, the annealing procedure was monitored by UV-PEEM to ensure that the second contrast inversion has occurred before the subsequent measurements were carried out. However, since the purpose of the measurements at SPring-8 was the use of synchrotron radiation for X-PEEM, and the synchrotron beam time was limited, the duration of the UV-PEEM investigation had to be restricted. Therefore, in particular for the thinner film thicknesses, for that high annealing temperatures are required, the annealing was carried out with coarse temperature steps without simultaneously UV-PEEM observation. As a consequence, for some samples the applied annealing temperature was higher than that necessary for the second contrast inversion that is displayed in figure 7.2. Still, it was confirmed in any case that the UV-PEEM image is equivalent to those displayed in figure 7.3 after the final annealing step. Table 7.2 summarizes the prepared film thicknesses t_{Co} for the SPELEEM experiment together with the maximum annealing temperature T_{max}. The sample temperature was measured with a thermocouple built in the sample holder.

Table 7.2: Cobalt film thicknesses t_{Co} and maximum annealing temperatures T_{max} for the samples prepared in the SPELEEM apparatus.

t_{Co} / nm	0.4	0.6	1.1	1.5	3.0	6.0
T_{max}/°C	540	540	540	530	410	460

Note that the temperature values depicted in figure 7.2 correspond to the onset of the second contrast inversion, whereas those in table 7.2 correspond to a sample state after the completion of the inversion. Thus, no direct comparability of the values should be expected. Further, uncertainties due to the different means of temperature measurement at the PEEM apparatus at TU Dortmund and the

SPELEEM experiment can not be excluded completely. However, the trend of lower necessary temperature for high film thicknesses, was reproduced.

7.4 Low-energy electron diffraction

In this section, the structural properties of the samples after the second UV-PEEM contrast inversion, which was introduced in section 7.1, are revealed by means of LEED patterns. For their acquisition, the SPELEEM experiment was used with the beam diameter and the electron kinetic energy set to 1.4 µm and 50 eV, respectively. For all patterns shown here, the electron beam was set to irradiate a terrace region in order to exclude information from the step-rich regions.

The patterns taken of samples with $t_{\mathrm{Co}} = 0.4$–$6.0\,\mathrm{nm}$ are displayed in figure 7.8. All patterns correspond to the same azimuthal sample orientation. Characteristic spots on the (1×1) grids of graphene, SiC, and cobalt are labeled in the figure. Note that a presence of the graphene spots does not necessarily result from the presence of a freestanding monolayer of graphene, since the $6\sqrt{3}$ reconstruction also exhibits these spots, as discussed in section 5.3. The film distortion-related streaks that were visible in the patterns taken in the as-deposited state have vanished in all patterns. Thus, the film quality has increased due to the annealing procedure. A ring-like structure with the same lattice constant than the (1×1)-graphene spots is visible in some patterns in figure 7.8. It is due to rotationally disordered graphitic carbon contamination resulting from hydrocarbon adsorbates cracked due to the impact of synchrotron radiation during previous X-PEEM measurements and the electron beam used in the LEED experiment [86, 148].

For $t_{\mathrm{Co}} = 0.4\,\mathrm{nm}$, all SiC and graphene spots are visible whereas only some of the $6\sqrt{3}$ spots can be noticed, as displayed in figure 7.8 (a). The partial presence of the $6\sqrt{3}$ structure might arise from coexisting intercalated and non-intercalated regions inside the irradiated area of 1.4 µm radius. Cobalt spots are not visible, in contrast to the corresponding pattern taken in the as-deposited state that was discussed in section 6.4. This absence may result from the formation of an amorphous cobalt silicide interface compound leaving behind a residual amount of metallic cobalt that is too low for the exhibition of a crystalline film.

For all patterns in figure 7.8 with $t_{\mathrm{Co}} \geq 0.6\,\mathrm{nm}$, the cobalt spots are present, therefore crystalline cobalt exists at the surface in these cases. It can be excluded that these correspond to cobalt silicide compounds since they have largely deviating lattice constants [149]. The cobalt spots show a sixfold symmetry revealing an hcp structure, since the fcc structure would lead to a threefold symmetry of the LEED pattern [150]. It should be mentioned that for $t_{\mathrm{Co}} = 1.1\,\mathrm{nm}$, a LEED pattern could

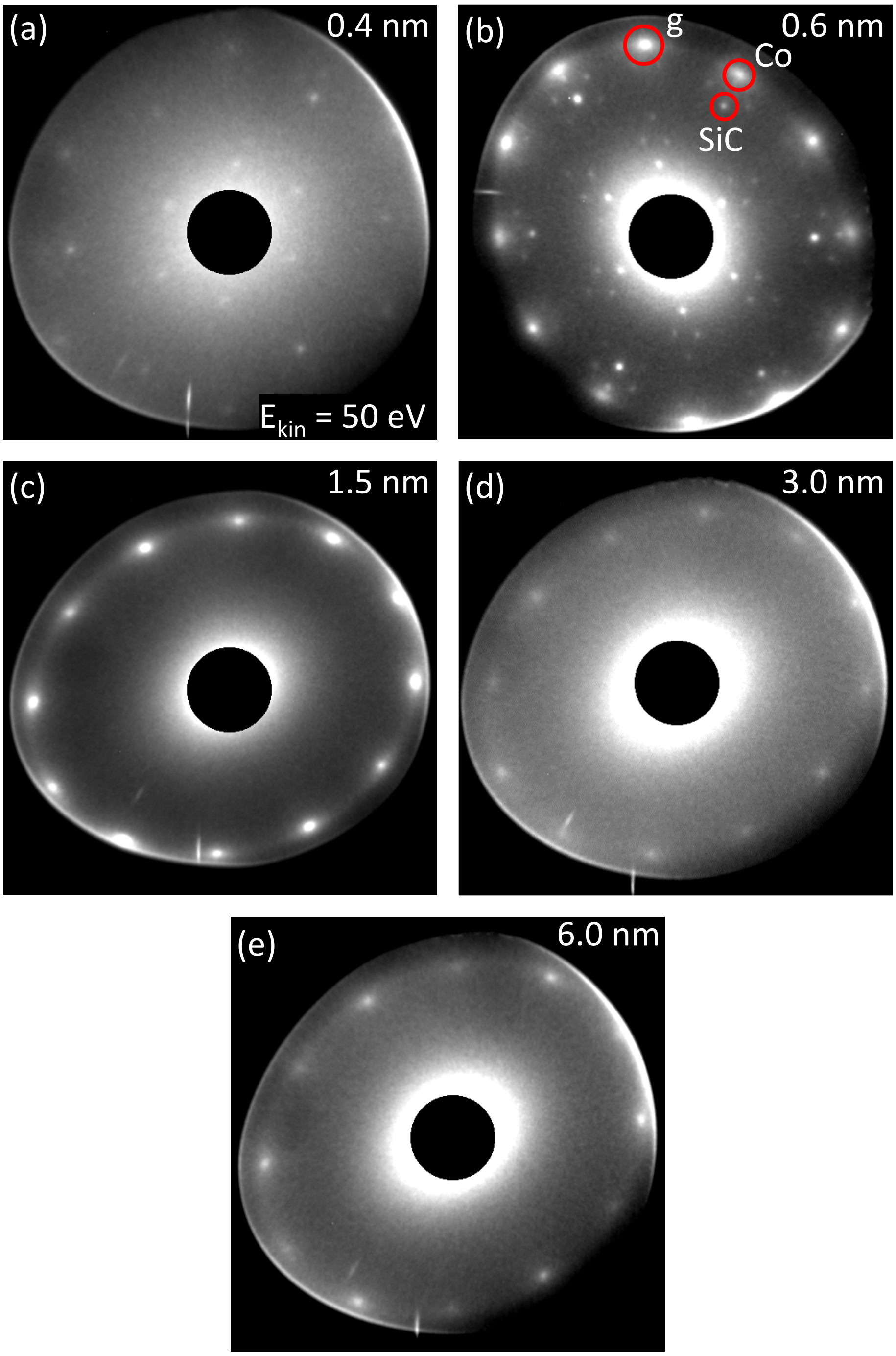

Figure 7.8: LEED patterns for $t_{\mathrm{Co}} = 0.4$–$6.0\,\mathrm{nm}$ acquired with an electron energy of 50 eV after the second UV-PEEM contrast inversion. The individual film thicknesses are indicated in the patterns. These patterns should be compared with those taken in the as-deposited state that are shown in figure 6.3.

not be recorded. Probably, this is due to a higher carbon contamination than for the other samples, because for this particular sample the total measurement time was significantly longer as for all other samples due to an unintentional interruption of the experiment.

For $t_{\mathrm{Co}} \geq 1.5\,\mathrm{nm}$, the SiC and $6\sqrt{3}$ spots vanish, as visible in figures 7.8 (c) – (e). Only the spots on the (1×1) grids of cobalt and graphene remain. The spots on the (1×1) graphene grid must result from a real graphene layer rather than the $6\sqrt{3}$ reconstruction since none of the other $6\sqrt{3}$-related spots are visible. This indicates that the $6\sqrt{3}$ reconstructed carbon layer is transformed into a graphene layer. The high surface sensitivity of the LEED patterns to only a few atomic layers can also be used to estimate whether the whole amount of cobalt intercalated or if a part stayed on top of the graphene layer. Hence, the graphene layer of which these spots results must reside in the topmost layers, therefore for instance in the case of $t_{\mathrm{Co}} = 6.0\,\mathrm{nm}$ at most a small portion of cobalt remains on top of the graphene film. The presence of the graphene spots for the highest film thickness therefore excludes the possibility that a large amount of cobalt remains on top of the intercalated graphene layer.

The results presented in this section indicate that the second UV-PEEM contrast inversion is associated with the lifting of the $6\sqrt{3}$ reconstruction and the subsequent intercalation of the graphene layer. While already the lowest deposit of $t_{\mathrm{Co}} = 0.4\,\mathrm{nm}$ would in principle be sufficient to intercalate one graphene layer, evidence for an intercalated graphene layer can only be found for $t_{\mathrm{Co}} \geq 1.5\,\mathrm{nm}$.

7.5 X-ray photoemission electron microscopy

Further insight into the structural and chemical transformations occurring to the cobalt film during the second UV-PEEM contrast inversion that was introduced in section 7.1.1 is provided by X-PEEM. Images with chemical contrast recorded at the Co L_3-edge provide information about the morphology of the cobalt films. X-ray absorption spectra (XAS) of the Co L-edge that were extracted from X-PEEM images allow a direct correlation of the UV-PEEM contrast inversions and the associated changes of the chemical state of the cobalt atoms. Finally, the magnetic properties of the intercalated samples will be investigated by means of X-PEEM images with magnetic contrast recorded at the Co L_3-edge. All images and spectra were recorded with the SPELEEM apparatus described in section 4.4.3. As for all measurements carried out with the SPELEEM apparatus, the sample temperature during the measurement was set to $\approx 200\,^{\circ}\mathrm{C}$.

7.5.1 Chemical contrast

In the following, the morphology of the cobalt films is investigated by means of X-PEEM images with chemical contrast taken at the Co L_3-edge. All images have been recorded after the samples were annealed to a temperature that was sufficient to complete the second UV-PEEM contrast inversion. The images shown in this section should be compared with those recorded in the as-deposited state that were discussed in section 6.5.1.

The X-PEEM image for $t_{\mathrm{Co}} = 0.4\,\mathrm{nm}$ in figure 7.9 (a) shows a speckled pattern. Since the image intensity is proportional to the x-ray absorption at the Co L_3-edge, the brighter areas in the image correspond to areas with a higher amount of cobalt. Thus, this image indicates inhomogeneities in the cobalt film, which could be explained by the formation of cobalt islands driven by the annealing of the film. The image in figure 7.9 (b) shows a similarly speckled pattern but the island size is larger compared to that in figure 7.9 (a). This island formation is also known as solid state dewetting, which is a common phenomenon that occurs due to the reduction of surface free energy upon annealing of thin films [151].

For the interpretation of these images, it is important to consider whether the contrast in the X-PEEM image could be explained due to an inhomogeneous coverage by graphene instead of an inhomogeneity in the cobalt film. However, the escape depth of secondary electrons in graphene amounts to 10 nm [152, 153]. A single graphene overlayer would therefore attenuate the electron yield from underlying layers only by 3 % according to equation 3.1. Therefore, it is highly unlikely that the observed contrast is due to an inhomogeneous coverage by graphene. Consequently, these regions can most likely be attributed to inhomogeneities in the cobalt film.

As visible in figure 7.9 (c), no more cobalt islands are present for $t_{\mathrm{Co}} = 1.1\,\mathrm{nm}$. However, some dark appearing features at the terraces indicate the onset of hole formation, which could be interpreted as the beginning of a dewetting process. Probably, no further dewetting did occur since the dewetting temperature increases for higher film thickness [151]. Figure 7.9 (c) moreover clearly shows that the step edge regions emit a greater cobalt signal than the terrace regions. Therefore, excess cobalt seems to agglomerate near the step edges. To a lesser extent, this can also be observed in figure 7.9 (a) and (b).

The observed island formation for $t_{\mathrm{Co}} < 1.1\,\mathrm{nm}$ could explain the incomplete conversion of the $6\sqrt{3}$ structure into a graphene layer that was detected by means of the XPS measurements $t_{\mathrm{Co}} = 0.4\,\mathrm{nm}$ in section 7.2.1. This follows from the assumption that the inhomogeneous cobalt coverage leads to an inhomogeneous intercalation. The spatially-averaged XPS spectra thus correspond to the average of cobalt-intercalated areas and those which are not intercalated. This becomes clear

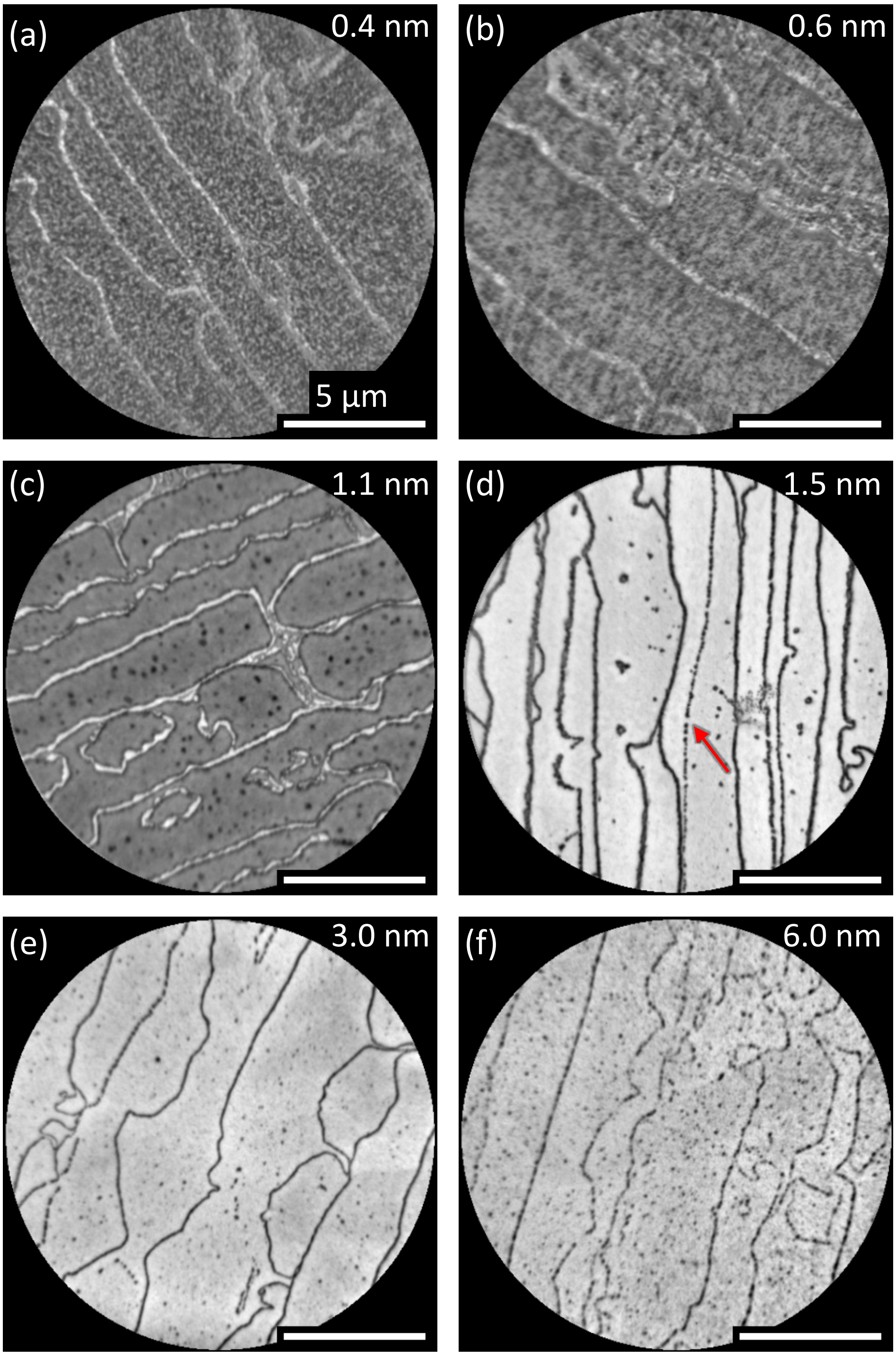

Figure 7.9: X-PEEM images with chemical contrast recorded at the Co L_3-edge for $t_{Co} = 0.4$–$6.0\,nm$. The individual thicknesses are indicated in the images. These images should be compared with those taken in the as-deposited state that are presented in figure 6.4. The arrow in image (d) points at an area in that the cobalt film seems to extend continuously over a step edge. The scale bar is 5 µm for all images.

by the following argument. Assume that the dewetting starts before the intercalation process. As consequence of the dewetting, the film thickness is locally increased in the case of the island-covered areas, whereas other areas expose an even thinner cobalt coverage. Consequently, the intercalation is favored in the high film thickness areas since the intercalation temperature decreases for higher film thickness, as indicated by the results in section 7.1.1. This might lead to a locally inhomogeneous cobalt intercalation. Since the XPS measurements are spatially averaging, several of these regions with high and low local cobalt coverage are within the measurement area that is defined by the size of the synchrotron radiation spot. As stated in section 4.3.2, the spot size is $70\,\mu\mathrm{m} \times 30\,\mu\mathrm{m}$, which is considerable larger than the field of view of the X-PEEM images presented in this section.

Figures 7.9 (d) – (e) show the images for $t_{\mathrm{Co}} = 1.5$–$6.0\,\mathrm{nm}$. They resemble those taken in the as-deposited state and show a mostly homogenous cobalt film. However, all of these images show small dark spots throughout the field of view. These are assigned to holes in the cobalt film. The hole density seems to increase with higher film thickness, which is probably due to higher stress in the thicker films. Remarkably, the contrast between the terraces and the step edges became stronger after annealing, while it was nearly vanishing for the highest film thickness in the as-deposited state. Therefore, the step covering seems to be better in the as-deposited state and after annealing the cobalt concentrates on the individual terraces. In this context, an interesting finding is that for $t_{\mathrm{Co}} \geq 1.5\,\mathrm{nm}$, in some cases, the cobalt film is flowing continuous over a step edge. In figure 7.9 (d) one representative of these step-covering features is marked by an arrow.

In the next section, x-ray absorption spectra extracted from the X-PEEM images will be used in order to gain information about the chemical state of the cobalt atoms.

7.5.2 X-ray absorption spectroscopy

In order to analyze the chemical state of the cobalt atoms, x-ray absorption spectra (XAS) were extracted from the X-PEEM data. For this purpose, for each of the about 200 points in the Co L-edge spectrum an individual X-PEEM image was acquired. Subsequently, either the whole field of view or certain regions of interest of the X-PEEM images were integrated. All spectra were recorded for both circular polarizations. Then, the spectra of both polarizations were averaged in order to cancel out the x-ray magnetic circular dichroism. Finally, the spectra were normalized to the maximum peak intensity.

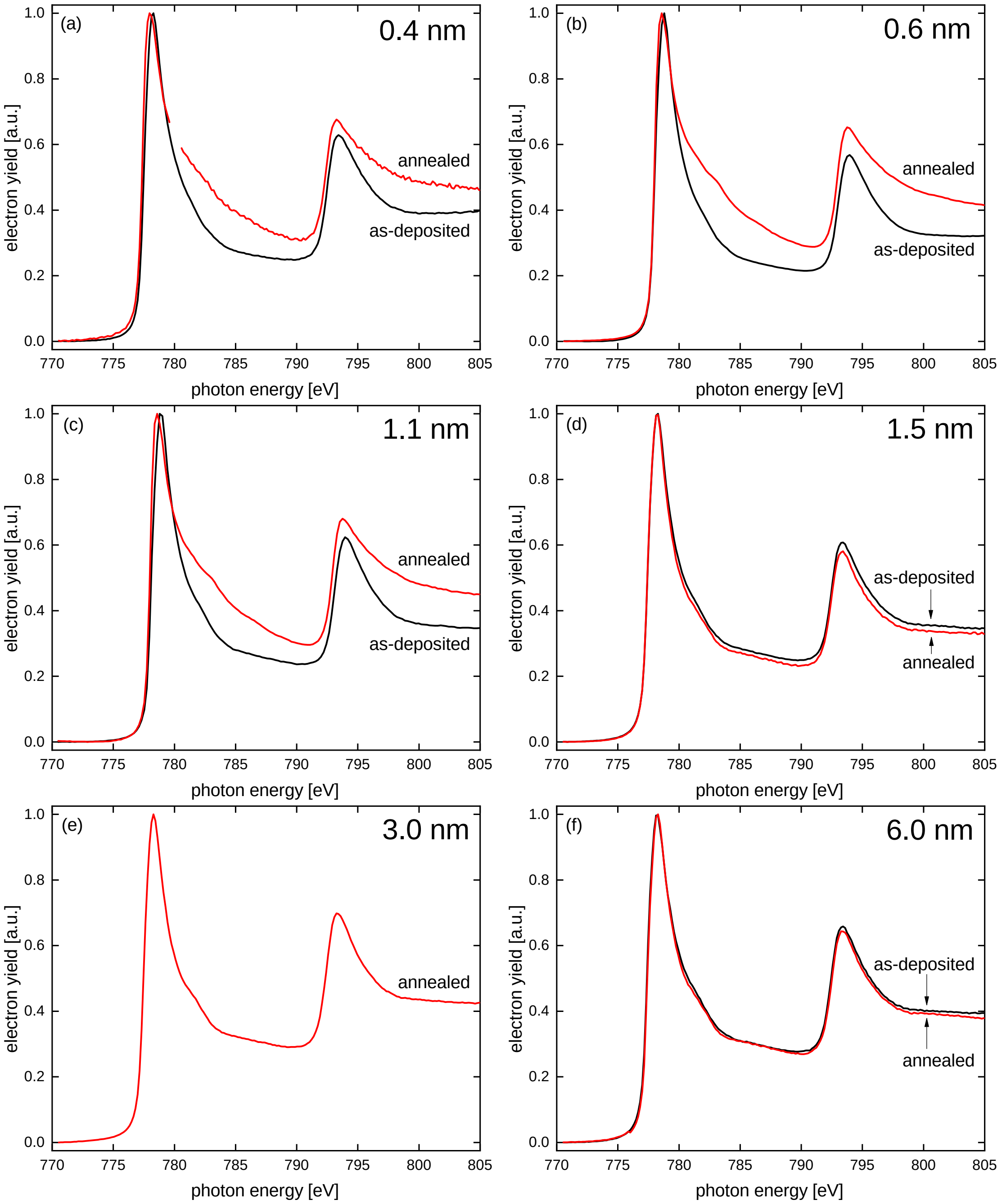

Figure 7.10: Spatially integrated XAS spectra recorded at the Co L-edge for $t_{\mathrm{Co}} = 0.4$–$6.0\,\mathrm{nm}$. The individual curves correspond to the as-deposited and the annealed state. For the 3.0 nm sample only the annealed state was analyzed. The missing data points in (a) were omitted since a distortion of the CCD camera signal occurred that was probably caused by a high voltage breakdown.

Spatially integrated XAS spectra

Figure 7.10 displays the spatial-integrated XAS spectra taken after the second UV-PEEM contrast inversion of samples with $t_{\mathrm{Co}} = 0.4$–$6.0\,\mathrm{nm}$. The spectra recorded in the as-deposited state are also shown in the plots for all film thicknesses except of 3.0 nm. Comparing the spectra taken in the as-deposited and the annealed states for $t_{\mathrm{Co}} = 0.4$–$1.1\,\mathrm{nm}$ reveals an almost identical shape for $h\nu = 770.0$–$779.8\,\mathrm{eV}$.

For $h\nu > 779.8\,\mathrm{eV}$, the x-ray absorption is clearly increased for the spectrum taken in the annealed state. This new absorption feature is consistent with the chemical state of cobalt atoms in silicide compounds [154, 155]. Therefore, during the second contrast inversion a chemical reaction of the cobalt and the silicon atoms occurs. This finding indicates that the cobalt penetrated the $6\sqrt{3}$ layer, released the carbon atoms of the $6\sqrt{3}$ layer, and substituted their bonds to the topmost silicon layer. Due to the relatively small intensity fraction associated with the new component, it is concluded that the majority of the cobalt atoms remains in the metallic state. This confirms the assumption that the cobalt silicide formation is self-limited, as already indicated by the XPS measurements in section 7.2.1.

For $t_{\mathrm{Co}} = 1.5$–$6.0\,\mathrm{nm}$ no silicide component was observed. Two possibilities exists to explain this finding. First, it could be assumed that no silicide forms at all. Yet, the LEED results in section 7.4 that were obtained for the same samples in the identical annealing state prove that graphene is present at the surface. It is not clear how a graphene formation could be explained without a silicide formation since for the graphene formation, the $6\sqrt{3}$ bonds to the substrate must be broken and substituted by bonds to cobalt atoms. Further, the silicide layer is presumably very thin as deduced from the limited intensity fraction of the respective component in the spectra presented in figures 7.10 (a) – (c). Therefore, it may be assumed that this small component is completely attenuated by the additional cobalt overlayers for $t_{\mathrm{Co}} = 1.5$–$6.0\,\mathrm{nm}$. Hence, it might be more likely to assume that the silicide formation occurs as well for the high film thicknesses.

The relative intensities of the metallic and the silicide components in principle allow for a quantification of the amount of reacted cobalt. However, due to the agglomeration of part of the cobalt, the effective cobalt film thickness after the annealing is not known. Hence, with the data at hand it can not be stated what the amount of reacted cobalt is in terms of a fraction of the initially deposited amount. In a future study, the local film thickness could be measured by means of spatially resolved XPS. For this purpose, the attenuation of the Si 2p photoelectrons resulting from the bulk SiC could compared before cobalt deposition and after annealing. This measurement of the local film thickness would then allow for the calculation of number of reacted cobalt atoms.

Spatially resolved XAS spectra

Spatial resolved XAS spectra provide a distinction between the chemical state of individual regions of interest in an X-PEEM image. In order to reveal any differences of the intercalation mechanisms at the terraces and the step edges, in figure 7.11 a comparison of spectra taken from a terrace and a step-rich region acquired after the second UV-PEEM contrast inversion are shown. The spectra in figure 7.11 correspond to $t_{\mathrm{Co}} = 0.4$–$1.1\,\mathrm{nm}$, which are those values for that a silicide formation was observed in the spatially integrated XAS spectra. As a result, the silicide signal at the terraces is found to be increased compared to the step edges. This indicates that the silicide formation favorably occurs at the terraces.

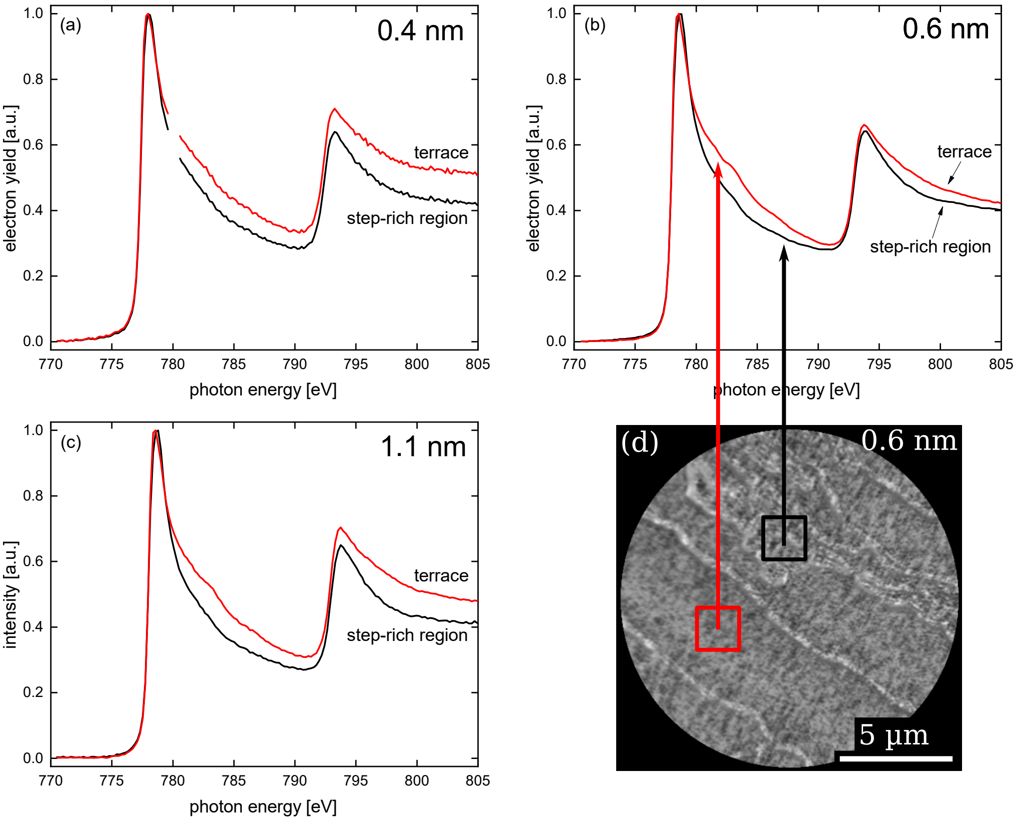

Figure 7.11: Co L-edge XAS spectra extracted from terrace and step-rich regions (a) – (c). The missing data points in (a) were omitted since a distortion of the CCD camera signal occurred that was probably caused by a high voltage breakdown. As an example, the terrace and step-rich regions are marked in the X-PEEM image with chemical contrast in (d).

A preferential silicide formation at the terraces would be consistent with references [35, 36], which investigated the intercalation of cobalt underneath monolayer graphene, instead of the bare $6\sqrt{3}$ reconstruction that is the main objective in this work. Those studies revealed that the cobalt atoms intercalate underneath the graphene monolayer but do not penetrate the underlying $6\sqrt{3}$ reconstruction. Since this is the seemingly preferred intercalation mechanism for monolayer graphene, it is straight-forward that no silicide is formed at the step edges, because the step edges of the samples investigated in this work are always covered by graphene monolayer stripes, as was discussed in section 5.2.

Taking into account the chemical contrast images shown in the previous section, it is clear that an increased amount of cobalt is present at the step edges. Therefore, it should be considered that the increased silicide-related signal at the terraces might also arise due to a suppression of the silicide signal of the step edges since the unreacted cobalt overlayer is thicker at the step edges. Note that the secondary electron escape depth in cobalt is 2.5 nm [77], which is significantly lower than in carbon. Therefore, an attenuation due to inhomogeneous cobalt coverage is more likely than the potential attenuation due to inhomogeneous carbon coverage discussed previously in section 7.5.1.

Summarizing, the findings presented in this and the previous section show that a self-limited silicide formation occurs after the second UV-PEEM contrast inversion. In the next and final section, the magnetic properties of the samples after the second contrast inversion will be investigated.

7.5.3 Magnetic contrast

In this section, the magnetic properties of the cobalt films after the second UV-PEEM contrast inversion will be investigated by means of X-PEEM images with magnetic contrast recorded at the Co L-edge. In order to determine the magnetic easy-axes, images with two perpendicular incidence directions of the synchrotron radiation were recorded for some samples. All measurements were carried out in remanence and without intentionally magnetizing the samples.

Figure 7.12 shows the X-PEEM images with magnetic contrast for $t_{\mathrm{Co}} = 0.4$–$1.1\,\mathrm{nm}$. Contrary to the images recorded in the as-deposited state, the terraces exhibit no magnetic contrast. The absence of a detectable magnetization at the terraces is most likely due to the silicide formation that was discussed in sections 7.2.1 and 7.5.2. Since cobalt silicide compounds are generally not ferromagnetic [156–158], a part of the cobalt on the terrace is in a silicide state that is non-ferromagnetic and the residual amount of metallic cobalt is too low to establish ferromagnetic ordering. The amount of cobalt at the terraces is further reduced since a part of it agglomerates near the step edges, as has been shown by the X-PEEM images with chemical contrast in section 7.5.1. This might represent an additional reason for the absence of magnetic order at the terraces.

Surprisingly, the step edges emit a dichroic signal. Therefore, the amount of agglomerated metallic cobalt at the step edges is sufficient to establish ferromagnetic order. For $t_{\mathrm{Co}} = 0.4\,\mathrm{nm}$ and $t_{\mathrm{Co}} = 0.6\,\mathrm{nm}$, as displayed in figures 7.12 (a) and (b), the magnetic contrast at the step edges is weak, possibly due to the small amount of cobalt in those cases. However, for $t_{\mathrm{Co}} = 1.1\,\mathrm{nm}$ the magnetic contrast at the step edges is clearly visible, as shown in figures 7.12 (c) and (d). Further, the magnetic contrast inverts upon rotation of the sample by 90°, which is indicated by the circles in figures 7.12 (c) and (d). Due to the angle dependence of the dichroic signal, this contrast inversion confirms that the contrast is of magnetic origin. Furthermore, it shows that the magnetization direction is in-plane, since for an out-of-plane orientation no contrast change would be expected.

The lateral extension of the magnetic areas perpendicular to the step edges is of the order of 100 nm. Therefore, this magnetic structure can be considered as self-assembled magnetic nanowires [159, 160]. It was shown in chapter 5 that the step edges are always associated with the formation of small stripes of monolayer graphene. Therefore, it may be presumed that the nanowire formation is associated with the monolayer graphene layers. Consequently, it would in principle be possible to tune the width of the nanowires, since the width of the graphene monolayers can be tuned by adjusting the SiC preparation temperature and time. Furthermore, the distance of the individual wires could be tuned by using SiC wafers with different off-axis orientations.

The X-PEEM images for $t_{\mathrm{Co}} = 1.5\,\mathrm{nm}$ are displayed in figures 7.13 (a) and (b). In these cases, magnetic contrast is observable throughout the field of view, contrary to the previously discussed lower film thicknesses. Interestingly, the magnetic domains are confined to individual substrate terraces. Since the incidence direction of the synchrotron radiation is almost parallel to the step edges in figure 7.13 (b), the strong black and white contrast in this image shows that the easy-axis is aligned parallel to the step edges. Hence, a strong uniaxial anisotropy is introduced by the step edges that is greater than the magneto-crystalline anisotropy of cobalt, which would favor multiple easy-axes. Previously, step anisotropies leading to easy-axes parallel or perpendicular to the step edges were observed for thin magnetic films on substrates with stepped surfaces. Furthermore, it was shown that the easy-axis can be switched by 90° by means of adsorption [59]. In this particular case, the step anisotropy of the cobalt intercalated graphene system may be tailored by using SiC wafers with different miscut angles. These so-called off-axis wafers have intentional miscuts of several degrees, which would multiply the number of steps.

In figure 7.13 (a), the incidence direction of the synchrotron radiation was altered by 90° with respect to figure 7.13 (b). The resulting contrast is very weak, which

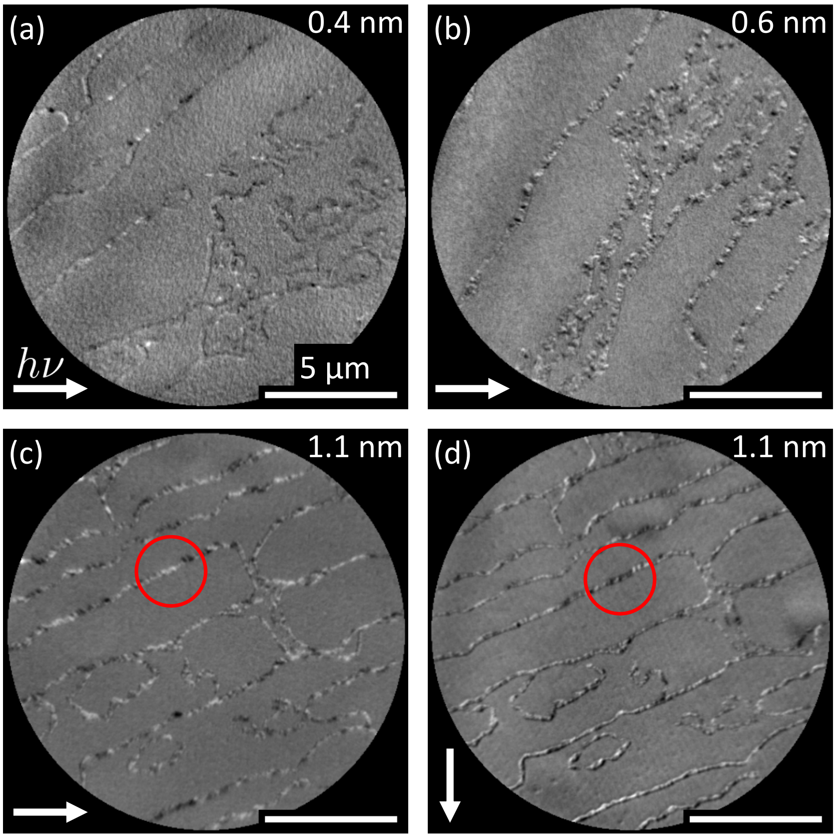

Figure 7.12: X-PEEM images with magnetic contrast recorded at the Co L_3-edge. The cobalt film thicknesses are indicated in the images. The circles in figures (c) and (d) mark an area whose contrast inverts upon sample rotation, which is a prove for the magnetic origin of the contrast. The arrows indicate the incidence angle of the synchrotron radiation. These images should be compared with those displayed in figure 6.5 that were recorded in the as-deposited state.

further proves that only a weak anisotropy is present perpendicular to the step edges. The contrast change upon change of the radiation incidence direction confirms an in-plane magnetization. Figure 7.13 (b) reveals another interesting property. Clearly, most of the image appears dark and only a minor fraction is white. Therefore, one magnetization direction seems to dominate, despite the sample should be macroscopically non-magnetic. This is almost a so-called single domain state. It occurs if a thin magnetic film is heated near to the Curie temperature, at which due to a low coercivity even a small residual magnetic field may align the magnetic moments [161]. Finally, the comparison with the images taken in the as-deposited state shows that some distinct magnetic domains persist even after the annealing process. This is due to the strong step-induced anisotropy that prevents the re-alignment of the magnetic moments even though they gained thermal energy during the annealing process. One of these features is marked by the circle in figure 7.13 (a).

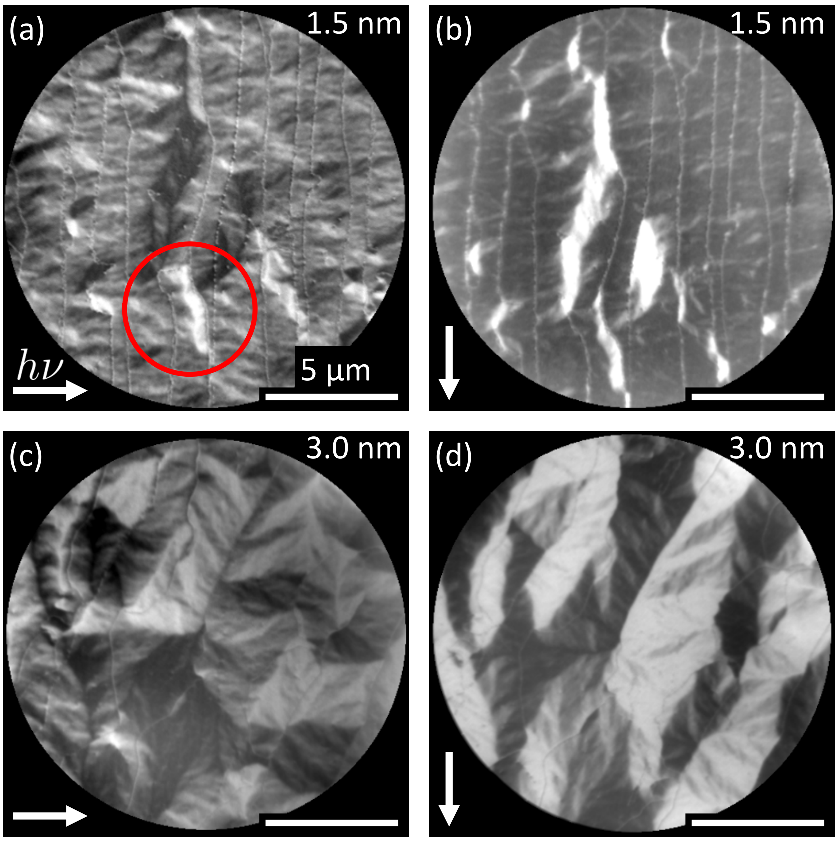

Figure 7.13: X-PEEM images with magnetic contrast recorded at the Co L_3-edge. The cobalt film thickness is indicated in the images. The arrows indicate the incidence direction of the synchrotron radiation. The images in (a) and (b) should be compared with that displayed in figure 6.6 (a) that was recorded in the as-deposited state. The circle in figure (a) marks a characteristic domain feature for comparison with the as-deposited state.

Figures 7.13 (c) and (d) show the magnetic domain structure for $t_{\mathrm{Co}} = 3.0\,\mathrm{nm}$. As for $t_{\mathrm{Co}} = 1.5\,\mathrm{nm}$, the X-PEEM image exhibits strong magnetic contrast. Again, the magnetic domains are confined to the substrate terraces, as evident from figure 7.13 (d) with the synchrotron radiation incidence parallel to the step edges. Some magnetic domains extend over multiple terraces, which was not observed for $t_{\mathrm{Co}} = 1.5\,\mathrm{nm}$. Probably, the larger cobalt film thickness enables this coupling due to the resulting closer proximity of the cobalt films on the adjacent terraces. Similar to the 1.5 nm sample, the comparison of figures 7.13 (c) and (d) reveals an in-plane magnetization and a weak anisotropy perpendicular to the step edges. In figure 7.13 (d), the number of the oppositely magnetized sample areas is approximately equal, as expected for a macroscopically non-magnetized sample. This is in contrast to the 1.5 nm sample, where almost a single domain state was achieved. It is assumed that the higher film thickness and the associated higher Curie temperature lead to a higher coercivity. Therefore, the residual magnetic fields that achieved to partly magnetize the 1.5 nm sample were too weak in the present case.

Figure 7.14 shows an X-PEEM image taken of a sample with $t_{\mathrm{Co}} = 6.0\,\mathrm{nm}$. Therein, distinct magnetic domains are visible, while only diffuse magnetic contrast was observed in the as-deposited state. The improved magnetic order results from reduced stress in the film that was also confirmed by the LEED pattern taken after annealing, as discussed in section 7.4. A comparison of figure 7.14 with the corresponding chemical contrast image of the same field view shown in figure 7.9 shows that the magnetic domains do no longer relate to the step edge pattern. This is contrary to the images shown in figure 7.13. Hence, the influence of the step anisotropy is further reduced and the magnetization pattern is more bulk-like. Since the number of different gray values in figure 7.14 is four, at least two separate magnetic easy-axes exist.

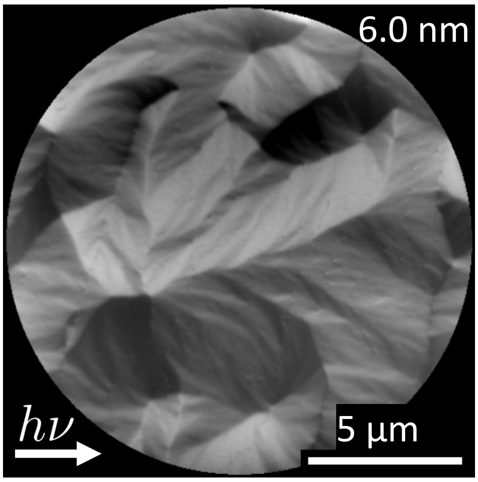

Figure 7.14: X-PEEM image with magnetic contrast recorded at the Co L_3-edge for $t_{\mathrm{Co}} = 6.0\,\mathrm{nm}$. The arrow indicates the direction of the incident synchrotron radiation. This image should be compared with that displayed in figure 6.6 (b) that was recorded in the as-deposited state.

In principle, the magneto-crystalline anisotropy of a Co(0001) single crystal would lead to a sixfold magnetic anisotropy, which has indeed been observed previously [162]. However, also magnetic contrast images with three or four different gray values are consistent with the Co(0001) surface, depending on whether the x-ray incidence direction is along an axis with high or low symmetry.

Finally, some remarks should be made concerning the in-plane magnetization that was observed throughout this work. Whereas for cobalt-intercalated graphene on iridium, the graphene film promotes a strong enhancement of the perpendicular magnetic anisotropy (PMA) of the cobalt films [30], here, for all investigated film thicknesses an in-plane easy-axis was found. Though PMA is usually associated with the interfaces of magnetic materials with high-atomic-mass substrates, it cannot be excluded that it emerges also on an SiC substrate due to the enhancing influence of the graphene layer. Further, it can not be excluded that PMA emerges at a different measurement temperature since the magnetic anisotropy is temperature-depended [38, 163].

7.6 Summary

In this chapter, the thermally-induced reaction of cobalt with the $6\sqrt{3}$ reconstructed SiC(0001) surface has been studied with UV-PEEM, XPS, LEED, and X-PEEM. The UV-PEEM measurements carried out during the annealing process revealed the occurrence of two characteristic work function contrast inversions for all investigated film thicknesses. The onset temperature of these contrast inversions depends on the cobalt film thickness. The combination of all measurements presented in this chapter indicates that the second UV-PEEM contrast inversion is a marker for the intercalation of cobalt underneath a graphene film.

The LEED and XPS measurements revealed a partial conversion of the $6\sqrt{3}$ reconstructed surface into a graphene-covered surface for low film thickness, whereas for high film thickness a full conversion was noticed. The partial decoupling for low film thickness might be linked to an island formation that is indicated by the X-PEEM images with chemical contrast. The Si 2p XPS spectra revealed a cobalt silicide formation, which was confirmed by the XAS spectra extracted from the X-PEEM images. The cobalt silicide formation was found to be self-limited. The X-PEEM investigation with magnetic contrast revealed three characteristic film thickness regimes. For $t_{\mathrm{Co}} = 0.4$–$1.1\,\mathrm{nm}$, the magnetization is only present at the step edge regions, whereas the terraces are non-magnetic. At $t_{\mathrm{Co}} = 1.5\,\mathrm{nm}$ and $t_{\mathrm{Co}} = 3.0\,\mathrm{nm}$, the whole cobalt film is magnetic and the magnetization is confined to the substrate terraces due to a step-induced anisotropy. For $t_{\mathrm{Co}} = 6.0\,\mathrm{nm}$, a bulk-like magnetization texture with multiple easy-axes evolves.

8 Conclusion

In this thesis, the interaction of thin cobalt films with the $\left(6\sqrt{3} \times 6\sqrt{3}\right)$-R30° reconstructed SiC(0001) surface has been investigated by a combination of surface-sensitive techniques. As previous research has shown, the $6\sqrt{3}$ reconstruction of the SiC(0001) surface can be transformed into an intercalated graphene monolayer by deposition and annealing of an adsorbate film. Yet, until now, this has not been demonstrated for adsorbed cobalt films. This thesis therefore thoroughly investigated the structural, chemical, and magnetic properties of annealed cobalt films deposited on $6\sqrt{3}$ reconstructed SiC samples. To reveal if the cobalt film thickness t_{Co} affects the properties of the sample system, it was varied in the range of 0.4–12 nm.

The SiC samples were prepared at high temperature in argon atmosphere, a technique that enables large-area and homogeneous graphene growth. The optimized preparation parameters led to a surface that was mainly covered by the $6\sqrt{3}$ reconstruction along with small stripes of monolayer graphene, as confirmed by UV-PEEM, LEED, and XPS. After cobalt deposition, no change to the chemical states of the silicon and carbon atoms could be observed with respect to the pristine SiC(0001)-$6\sqrt{3}$ sample. Thus, it can be stated that no reaction occurred at room temperature. For all investigated film thicknesses, magnetic X-PEEM contrast was observed at the Co L_3-edge in the as-deposited state. The magnetic easy-axis was determined by angle-dependent measurements and found to be in-plane. While for $t_{\mathrm{Co}} \leq 1.1\,\mathrm{nm}$ ordered domains were revealed, for $t_{\mathrm{Co}} = 1.5$–$6.0\,\mathrm{nm}$ increasingly disordered magnetization patterns were found and attributed to insufficient film quality due to the deposition at room temperature.

The cobalt-deposited SiC samples were subsequently annealed in order to activate the intercalation process. The C 1s XPS spectrum for $t_{\mathrm{Co}} = 2.8\,\mathrm{nm}$ revealed a single sp^2-hybridized state, confirming that the $6\sqrt{3}$ reconstructed carbon layer transformed into a graphene film, as observed previously for other adsorbates such as gold, germanium, or manganese [25, 26, 47]. In the case of $t_{\mathrm{Co}} = 0.4\,\mathrm{nm}$, an incomplete conversion of the $6\sqrt{3}$ reconstructed layer into a graphene layer was observed in the C 1s XPS spectrum. This can be attributed to agglomeration of the cobalt atoms into islands, which was found to occur for all films with $t_{\mathrm{Co}} < 1.5\,\mathrm{nm}$, as revealed by X-PEEM images with chemical contrast recorded at the Co L_3-edge. Further, a previously-neglected [131] silicide formation at the cobalt-SiC interface was revealed by XPS and XAS, which was found to be self-limited.

A comprehensive real-time UV-PEEM investigation has been carried out during the annealing process. As a result, it was found that the lowest necessary temperature to activate the intercalation process depends on t_{Co}. The minimum value was 340 °C for $t_{\mathrm{Co}} = 1.4\,\mathrm{nm}$, whereas 570 °C were measured for $t_{\mathrm{Co}} = 0.4\,\mathrm{nm}$. A high intercalation temperature for a low film thickness is consistent with earlier reports that used monolayer graphene on SiC as a substrate [35, 36]. For $t_{\mathrm{Co}} \rightarrow 12\,\mathrm{nm}$, the intercalation temperature converges to $\approx$ 420 °C. The cobalt intercalation mechanism was analyzed in detail for $t_{\mathrm{Co}} = 5.6\,\mathrm{nm}$ and $t_{\mathrm{Co}} = 11\,\mathrm{nm}$. It was found that the intercalation starts at the step edges, a mechanism that is similar to that of germanium intercalation [26] and distinct from that of hydrogen intercalation [49].

The magnetic properties of the intercalated cobalt films were investigated by the acquisition of X-PEEM images with magnetic contrast acquired at the Co L_3-edge. For all investigated film thicknesses, the magnetization orientation was in-plane. Self-assembled magnetic nanowires formed at the step edges for $t_{\mathrm{Co}} \leq 1.1\,\mathrm{nm}$, whereas the terraces turned non-magnetic. These nanowires allow for the investigation of one-dimensional magnetism on an SiC substrate. For $t_{\mathrm{Co}} \geq 1.5\,\mathrm{nm}$, the terraces are magnetic and the magnetization axis is parallel to the step edges due to a magnetic anisotropy that is induced by the step edges. This t_{Co}-condition might be the most technologically-relevant due to the fully-magnetic surface. Finally, for $t_{\mathrm{Co}} = 6.0\,\mathrm{nm}$ a magnetization pattern with multiple easy-axes without the influence of a step anisotropy was observed.

After the demonstration of the fundamental properties of the sample system within this thesis, future studies can focus on specific aspects, some of which are briefly outlined below. First, as it is expected that the step height influences the magnetic anisotropy and therefore the easy-axes, a modification of the step height possibly leads to new magnetic phases. Recently, a modified SiC preparation procedure has been reported that drastically reduces the step height [164]. Second, as a potential route to introduce a perpendicular magnetic anisotropy, the intercalation of a heavy non-magnetic metal prior to the magnetic film could be attempted. Platinum would be suited for this purpose as it forms an ordered interface with SiC [165].

In conclusion, within this thesis the reaction of adsorbed cobalt films with the $6\sqrt{3}$ reconstructed SiC(0001) surface has been investigated comprehensively. As has been demonstrated, thermal annealing leads to the intercalation of cobalt, converting the $6\sqrt{3}$ reconstructed surface into a graphene-covered surface. The intercalation mechanism depends strongly on the cobalt film thickness and the magnetic anisotropy of the intercalated cobalt films is affected by the step bunching effect. In all, the results provide a well-founded overview of the structural, chemical, and magnetic properties of the graphene-cobalt interface on an SiC substrate. They establish a viable basis for further studies targeting selective modifications of the magnetic properties.

Bibliography

[1] K. S. Novoselov, A. K. Geim, S. V. Morozov, D. Jiang, Y. Zhang, S. V. Dubonos, I. V. Grigorieva, and A. A. Firsov, *Electric Field Effect in Atomically Thin Carbon Films*, Science **306**, 666 (2004).

[2] N. D. Mermin, *Crystalline Order in Two Dimensions*, Phys. Rev. **176**, 250 (1968).

[3] C. Lee, X. Wei, J. W. Kysar, and J. Hone, *Measurement of the Elastic Properties and Intrinsic Strength of Monolayer Graphene*, Science **321**, 385 (2008).

[4] A. A. Balandin, S. Ghosh, W. Bao, I. Calizo, D. Teweldebrhan, F. Miao, and C. N. Lau, *Superior Thermal Conductivity of Single-Layer Graphene*, Nano Lett. **8**, 902 (2008).

[5] S. V. Morozov, K. S. Novoselov, M. I. Katsnelson, F. Schedin, D. C. Elias, J. A. Jaszczak, and A. K. Geim, *Giant Intrinsic Carrier Mobilities in Graphene and Its Bilayer*, Phys. Rev. Lett. **100**, 016602 (2008).

[6] Y.-M. Lin, C. Dimitrakopoulos, K. A. Jenkins, D. B. Farmer, H.-Y. Chiu, A. Grill, and Ph. Avouris, *100-GHz Transistors from Wafer-Scale Epitaxial Graphene*, Science **327**, 662 (2010).

[7] Z. Guo, R. Dong, P. S. Chakraborty, N. Lourenco, J. Palmer, Y. Hu, M. Ruan, J. Hankinson, J. Kunc, J. D. Cressler, C. Berger, and W. A. de Heer, *Record Maximum Oscillation Frequency in C-Face Epitaxial Graphene Transistors*, Nano Lett. **13**, 942 (2013).

[8] W. Han, R. K. Kawakami, M. Gmitra, and J. Fabian, *Graphene spintronics*, Nat. Nanotechnol. **9**, 794 (2014).

[9] V. M. Karpan, G. Giovannetti, P. A. Khomyakov, M. Talanana, A. A. Starikov, M. Zwierzycki, J. van den Brink, G. Brocks, and P. J. Kelly, *Graphite and Graphene as Perfect Spin Filters*, Phys. Rev. Lett. **99**, 176602 (2007).

[10] P. Gargiani, R. Cuadrado, H. B. Vasili, M. Pruneda, and M. Valvidares, *Graphene-based synthetic antiferromagnets and ferrimagnets*, Nat. Commun. **8**, 699 (2017).

[11] A. K. Geim, *Nobel Lecture: Random walk to graphene*, Rev. Mod. Phys. **83**, 851 (2011).

[12] K. S. Novoselov, *Nobel Lecture: Graphene: Materials in the Flatland*, Rev. Mod. Phys. **83**, 837 (2011).

[13] K. S. Novoselov, V. I. Fal'ko, L. Colombo, P. R. Gellert, M. G. Schwab, and K. Kim, *A roadmap for graphene*, Nature **490**, 192 (2012).

[14] A. J. van Bommel, J. E. Crombeen, and A. van Tooren, *LEED and Auger electron observations of the SiC(0001) surface*, Surf. Sci. **48**, 463 (1975).

[15] C. Berger, Z. Song, T. Li, X. Li, A. Y. Ogbazghi, R. Feng, Z. Dai, A. N. Marchenkov, E. H. Conrad, P. N. First, and W. A. de Heer, *Ultrathin Epitaxial Graphite: 2D Electron Gas Properties and a Route toward Graphene-based Nanoelectronics*, J. Phys. Chem. B **108**, 19912 (2004).

[16] K. V. Emtsev, A. Bostwick, K. Horn, J. Jobst, G. L. Kellogg, L. Ley, J. L. McChesney, T. Ohta, S. A. Reshanov, J. Röhrl, E. Rotenberg, A. K. Schmid, D. Waldmann, H. B. Weber, and Th. Seyller, *Towards wafer-size graphene layers by atmospheric pressure graphitization of silicon carbide*, Nat. Mater. **8**, 203 (2009).

[17] M. Ostler, F. Speck, M. Gick, and Th. Seyller, *Automated preparation of high-quality epitaxial graphene on 6H-SiC(0001)*, Phys. Status Solidi B **247**, 2924 (2010).

[18] W. A. de Heer, C. Berger, M. Ruan, M. Sprinkle, X. Li, Y. Hu, B. Zhang, J. Hankinson, and E. Conrad, *Large area and structured epitaxial graphene produced by confinement controlled sublimation of silicon carbide*, Proc. Natl. Acad. Sci. U.S.A. **108**, 16900 (2011).

[19] B. Dlubak, M.-B. Martin, C. Deranlot, B. Servet, S. Xavier, R. Mattana, M. Sprinkle, C. Berger, W. A. de Heer, F. Petroff, A. Anane, P. Seneor, and A. Fert, *Highly efficient spin transport in epitaxial graphene on SiC*, Nat. Phys. **8**, 557 (2012).

[20] C. Riedl, C. Coletti, and U. Starke, *Structural and electronic properties of epitaxial graphene on SiC(0 0 0 1): a review of growth, characterization, transfer doping and hydrogen intercalation*, J. Phys. D: Appl. Phys. **43**, 374009 (2010).

[21] M. S. Whittingham, in *Intercalation Chemistry*, edited by M. S. Whittingham and A. J. Jacobson (Academic Press, New York, 1982).

[22] S. Vlaic, N. Rougemaille, A. Kimouche, B. S. Burgos, A. Locatelli, and J. Coraux, *Intercalating cobalt between graphene and iridium (111): Spatially dependent kinetics from the edges*, Phys. Rev. Mater. **1**, 053406 (2017).

[23] J. S. Bunch, S. S. Verbridge, J. S. Alden, A. M. van der Zande, J. M. Parpia, H. G. Craighead, and P. L. McEuen, *Impermeable Atomic Membranes from Graphene Sheets*, Nano Lett. **8**, 2458 (2008).

[24] C. Riedl, C. Coletti, T. Iwasaki, A. A. Zakharov, and U. Starke, *Quasi-Free-Standing Epitaxial Graphene on SiC Obtained by Hydrogen Intercalation*, Phys. Rev. Lett. **103**, 246804 (2009).

[25] I. Gierz, T. Suzuki, R. T. Weitz, D. S. Lee, B. Krauss, C. Riedl, U. Starke, H. Höchst, J. H. Smet, C. R. Ast, and K. Kern, *Electronic decoupling of an epitaxial graphene monolayer by gold intercalation*, Phys. Rev. B **81**, 235408 (2010).

[26] K. V. Emtsev, A. A. Zakharov, C. Coletti, S. Forti, and U. Starke, *Ambipolar doping in quasifree epitaxial graphene on SiC(0001) controlled by Ge intercalation*, Phys. Rev. B **84**, 125423 (2011).

[27] M. Weser, Y. Rehder, K. Horn, M. Sicot, M. Fonin, A. B. Preobrajenski, E. N. Voloshina, E. Goering, and Yu. S. Dedkov, *Induced magnetism of carbon atoms at the graphene/Ni(111) interface*, Appl. Phys. Lett. **96**, 012504 (2010).

[28] H. Vita, St. Böttcher, P. Leicht, K. Horn, A. B. Shick, and F. Máca, *Electronic structure and magnetic properties of cobalt intercalated in graphene on Ir(111)*, Phys. Rev. B **90**, 165432 (2014).

[29] H.-Ch. Mertins, C. Jansing, M. Gilbert, M. Krivenkov, J. Sanchez-Barriga, A. Varykhalov, O. Rader, H. Wahab, H. Timmers, A. Gaupp, M. Tesch, A. Sokolov, D. Legut, and P. M. Oppeneer, *Magneto-optical reflection spectroscopy on graphene/Co in the soft x-ray range*, J. Phys.: Conf. Ser. **903**, 012025 (2017).

[30] N. Rougemaille, A. T. N'Diaye, J. Coraux, C. Vo-Van, O. Fruchart, and A. K. Schmid, *Perpendicular magnetic anisotropy of cobalt films intercalated under graphene*, Appl. Phys. Lett. **101**, 142403 (2012).

[31] R. Decker, J. Brede, N. Atodiresei, V. Caciuc, S. Blügel, and R. Wiesendanger, *Atomic-scale magnetism of cobalt-intercalated graphene*, Phys. Rev. B **87**, 041403 (2013).

[32] A. D. Vu, J. Coraux, G. Chen, A. T. N'Diaye, A. K. Schmid, and N. Rougemaille, *Unconventional magnetisation texture in graphene/cobalt hybrids*, Sci. Rep. **6**, 24783 (2016).

[33] H. Yang, A. D. Vu, A. Hallal, N. Rougemaille, J. Coraux, G. Chen, A. K. Schmid, and M. Chshiev, *Anatomy and Giant Enhancement of the Perpendicular Magnetic Anisotropy of Cobalt–Graphene Heterostructures*, Nano Lett. **16**, 145 (2016).

[34] H. Yang, G. Chen, A. A. C. Cotta, A. T. N'Diaye, S. A. Nikolaev, E. A. Soares, W. A. A. Macedo, K. Liu, A. K. Schmid, A. Fert, and M. Chshiev, *Significant Dzyaloshinskii-Moriya interaction at graphene-ferromagnet interfaces due to the Rashba effect*, Nat. Mater. **17**, 605 (2018).

[35] L. H. de Lima, R. Landers, and A. de Siervo, *Patterning Quasi-Periodic Co 2D-Clusters underneath Graphene on SiC(0001)*, Chem. Mater. **26**, 4172 (2014).

[36] Y. Zhang, H. Zhang, Y. Cai, J. Song, and P. He, *The investigation of cobalt intercalation underneath epitaxial graphene on 6H-SiC(0001)*, Nanotechnology **28**, 075701 (2017).

[37] F. Bisti, G. Profeta, H. Vita, M. Donarelli, F. Perrozzi, P. M. Sheverdyaeva, P. Moras, K. Horn, and L. Ottaviano, *Electronic and geometric structure of graphene/SiC(0001) decoupled by lithium intercalation*, Phys. Rev. B **91**, 245411 (2015).

[38] C. A. F. Vaz, J. A. C. Bland, and G. Lauhoff, *Magnetism in ultrathin film structures*, Rep. Prog. Phys. **71**, 056501 (2008).

[39] P. R. Wallace, *The Band Theory of Graphite*, Phys. Rev. **71**, 622 (1947).

[40] J. C. Meyer, A. K. Geim, M. I. Katsnelson, K. S. Novoselov, T. J. Booth, and S. Roth, *The structure of suspended graphene sheets*, Nature **446**, 60 (2007).

[41] A. K. Geim, *Graphene: Status and Prospects*, Science **324**, 1530 (2009).

[42] U. Starke, in *Silicon Carbide: Recent Major Advances*, edited by W. J. Choyke, H. Matsunami, and G. Pensl (Springer, Berlin, 2004).

[43] U. Starke, J. Bernhardt, J. Schardt, and K. Heinz, *SiC surface reconstruction: relevancy of atomic structure for growth technology*, Surf. Rev. Lett. **6**, 1129 (1999).

[44] M. Stockmeier, R. Müller, S. A. Sakwe, P. J. Wellmann, and A. Magerl, *On the lattice parameters of silicon carbide*, J. Appl. Phys. **105**, 033511 (2009).

[45] F. Varchon, R. Feng, J. Hass, X. Li, B. N. Nguyen, C. Naud, P. Mallet, J.-Y. Veuillen, C. Berger, E. H. Conrad, and L. Magaud, *Electronic Structure of Epitaxial Graphene Layers on SiC: Effect of the Substrate*, Phys. Rev. Lett. **99**, 126805 (2007).

[46] S. Goler, C. Coletti, V. Piazza, P. Pingue, F. Colangelo, V. Pellegrini, K. V. Emtsev, S. Forti, U. Starke, F. Beltram, and S. Heun, *Revealing the atomic structure of the buffer layer between SiC(0001) and epitaxial graphene*, Carbon **51**, 249 (2013).

[47] T. Gao, Y. Gao, C. Chang, Y. Chen, M. Liu, S. Xie, K. He, X. Ma, Y. Zhang, and Z. Liu, *Atomic-Scale Morphology and Electronic Structure of Manganese Atomic Layers Underneath Epitaxial Graphene on SiC(0001)*, ACS Nano **6**, 6562 (2012).

[48] L. Jin, Q. Fu, Y. Yang, and X. Bao, *A comparative study of intercalation mechanism at graphene/Ru(0001) interface*, Surf. Sci. **617**, 81 (2013).

[49] F. Speck, M. Ostler, S. Besendörfer, J. Krone, M. Wanke, and Th. Seyller, *Growth and Intercalation of Graphene on Silicon Carbide Studied by Low-Energy Electron Microscopy*, Ann. Phys. (Berl.) **529**, 1700046 (2017).

[50] C. M. Hurd, *Varieties of magnetic order in solids*, Contemp. Phys. **23**, 469 (1982).

[51] H. Lüth, *Solid Surfaces, Interfaces and Thin Films* (Springer, Berlin, 2001).

[52] J. Stöhr and H. C. Siegmann, *Magnetism* (Springer, Berlin, 2006).

[53] W. Nolting, *Grundkurs Theoretische Physik 7: Viel-Teilchen-Theorie* (Springer, Berlin, 2015).

[54] C. Keutner, *Der direkte Blick auf die Magnetosomen-Kette: PEEM- und SEM-Untersuchungen am intakten Magnetospirillum magnetotacticum* (Ph.D. thesis, Technische Universität Dortmund, 2015).

[55] H. Ibach and H. Lüth, *Festkörperphysik: Einführung in die Grundlagen* (Springer, Berlin, 2009).

[56] J. F. Janak, *Uniform susceptibilities of metallic elements*, Phys. Rev. B **16**, 255 (1977).

[57] H. Ibach, *Physics of Surfaces and Interfaces* (Springer, Berlin, 2006).

[58] H. P. Oepen, M. Speckmann, Y. Millev, and J. Kirschner, *Unified approach to thickness-driven magnetic reorientation transitions*, Phys. Rev. B **55**, 2752 (1997).

[59] M. T. Johnson, P. J. H. Bloemen, F. J. A. den Broeder, and J. J. de Vries, *Magnetic anisotropy in metallic multilayers*, Rep. Prog. Phys. **59**, 1409 (1996).

[60] A. Hubert and R. Schäfer, *Magnetic Domains: The Analysis of Magnetic Microstructures* (Springer, Berlin, 1998).

[61] H. Ibach, in *Electron Spectroscopy for Surface Analysis*, edited by H. Ibach (Springer, Berlin, 1977).

[62] S. Hüfner, *Photoelectron Spectroscopy* (Springer, Berlin, 1996).

[63] M. P. Seah and W. A. Dench, *Quantitative Electron Spectroscopy of Surfaces: A Standard Data Base for Electron Inelastic Mean Free Paths in Solids*, Surf. Interface Anal. **1**, 2 (1979).

[64] NIST, *Electron Inelastic-Mean-Free-Path Database – Version 1.2* (National Institute of Standards and Technology, Gaithersburg MD, 1999).

[65] A. Einstein, *Über einen die Erzeugung und Verwandlung des Lichtes betreffenden heuristischen Gesichtspunkt*, Ann. Phys. **322**, 132 (1905).

[66] U. Gelius, E. Basilier, S. Svensson, T. Bergmark, and K. Siegbahn, *A high resolution ESCA instrument with X-ray monochromator for gases and solids*, J. Electron Spectros. Relat. Phenom. **2**, 405 (1973).

[67] T. Mayer-Kuckuk, *Atomphysik* (B. G. Teubner, Stuttgart, 1985).

[68] K. Oura, M. Katayama, A. V. Zotov, V. G. Lifshits, and A. A. Saranin, *Surface Science* (Springer, Berlin, 2003).

[69] K. Siegbahn, *Photoelectron spectroscopy: retrospects and prospects*, Phil. Trans. R. Soc. Lond. A **318**, 3 (1986).

[70] S. Doniach and M. Sunjic, *Many-electron singularity in X-ray photoemission and X-ray line spectra from metals*, J. Phys. C: Solid State Phys. **3**, 285 (1970).

[71] M. Cardona and L. Ley, in *Photoemission in Solids I*, edited by M. Cardona and L. Ley (Springer, Berlin, 1978).

[72] J. Végh, *The Shirley background revised*, J. Electron Spectros. Relat. Phenom. **151**, 159 (2006).

[73] R. Hesse, T. Chassé, and R. Szargan, *Peak shape analysis of core level photoelectron spectra using UNIFIT for WINDOWS*, Fresenius J. Anal. Chem. **365**, 48 (1999).

[74] G. Schönhense, *Imaging of magnetic structures by photoemission electron microscopy*, J. Phys.: Condens. Matter **11**, 9517 (1999).

[75] A. Scholl, H. Ohldag, F. Nolting, S. Anders, and J. Stöhr, in *Magnetic Microscopy of Nanostructures*, edited by H. Hopster and H. P. Oepen (Springer, Berlin, 2005).

[76] M. E. Kordesch, in *In Situ Real-Time Characterization of Thin Films*, edited by O. Auciello and A. R. Krauss (John Wiley & Sons, Hoboken NJ, 2001).

[77] J. Stöhr and S. Anders, *X-ray spectro-microscopy of complex materials and surfaces*, IBM J. Res. Dev. **44**, 535 (2000).

[78] W. Gudat and C. Kunz, *Close Similarity between Photoelectric Yield and Photoabsorption Spectra in the Soft-X-Ray Range*, Phys. Rev. Lett. **29**, 169 (1972).

[79] J. Stöhr, *NEXAFS Spectroscopy* (Springer, Berlin, 1992).

[80] J. C. Fuggle and J. E. Inglesfield, in *Unoccupied Electronic States: Fundamentals for XANES, EELS, IPS and BIS*, edited by J. C. Fuggle and J. E. Inglesfield (Springer, Berlin, 1992).

[81] W. Swiech, G. H. Fecher, Ch. Ziethen, O. Schmidt, G. Schönhense, K. Grzelakowski, C. M. Schneider, R. Frömter, H. P. Oepen, and J. Kirschner, *Recent progress in photoemission microscopy with emphasis on chemical and magnetic sensitivity*, J. Electron Spectros. Relat. Phenom. **84**, 171 (1997).

[82] W. Kuch, R. Schäfer, P. Fischer, and F. U. Hillebrecht, *Magnetic Microscopy of Layered Structures* (Springer, Berlin, 2015).

[83] G. Schütz, W. Wagner, W. Wilhelm, P. Kienle, R. Zeller, R. Frahm, and G. Materlik, *Absorption of circularly polarized x rays in iron*, Phys. Rev. Lett. **58**, 737 (1987).

[84] A. Scholl, H. Ohldag, F. Nolting, J. Stöhr, and H. A. Padmore, *X-ray photoemission electron microscopy, a tool for the investigation of complex magnetic structures (invited)*, Rev. Sci. Instrum. **73**, 1362 (2002).

[85] W. Kuch, in *Magnetism: A Synchrotron Radiation Approach*, edited by E. Beaurepaire, H. Bulou, F. Scheurer, and J.-P. Kappler (Springer, Berlin, 2006).

[86] G. Ertl and J. Küppers, *Low Energy Electrons and Surface Chemistry* (VCH, Weinheim, 1985).

[87] M. Gianfelice, *Untersuchung des Rekonstruktionsverhaltens von gestuftem 4H-SiC(0001) mittels Rasterkraftmikroskopie* (Master's thesis, Technische Universität Dortmund, 2017).

[88] C. Hilscher, *Großflächiges Wachstum von Graphen auf SiC(0001)-6H* (Master's thesis, Technische Universität Dortmund, 2015).

[89] E. J. Davies, *Conduction and induction heating* (Peter Peregrinus, London, 1990).

[90] C. J. Rademeyer, H. G. C. Human, and P. K. Faure, *The electrical resistivity of some graphite types as used in electrothermal atomic absorption spectrometry*, Spectrochim. Acta B **38**, 945 (1983).

[91] P. Mehring, *SAMs organischer Halbleiter auf Au-Substraten: Eine STM-Untersuchung* (Ph.D. thesis, Technische Universität Dortmund, 2013).

[92] D. B. Murphy and M. W. Davidson, *Fundamentals of Light Microscopy and Electronic Imaging* (John Wiley & Sons, Hoboken NJ, 2012).

[93] C. Westphal, U. Berges, S. Dreiner, R. Follath, M. Krause, F. Schäfers, D. Schirmer, and M. Schürmann, *The plane-grating monochromator beamline at the U55 undulator for surface and interface studies at DELTA*, J. Electron Spectros. Relat. Phenom. **144-147**, 1117 (2005).

[94] M. Oura, T. Nakamura, T. Takeuchi, Y. Senba, H. Ohashi, K. Shirasawa, T. Tanaka, M. Takeuchi, Y. Furukawa, T. Hirono, T. Ohata, H. Kitamura, and S. Shin, *Degree of circular polarization of soft X-rays emitted from a multi-polarization-mode undulator characterized by means of magnetic circular dichroism measurements*, J. Synchrotron Radiat. **14**, 483 (2007).

[95] H. Ohashi, Y. Senba, H. Kishimoto, T. Miura, E. Ishiguro, T. Takeuchi, M. Oura, K. Shirasawa, T. Tanaka, M. Takeuchi, K. Takeshita, S. Goto, S. Takahashi, H. Aoyagi, M. Sano, Y. Furukawa, T. Ohata, T. Matsushita, Y. Ishizawa, S. Taniguchi, Y. Asano, Y. Harada, T. Tokushima, K. Horiba, H. Kitamura, T. Ishikawa, and S. Shin, *Performance of a Highly Stabilized and High-resolution Beamline BL17SU for Advanced Soft X-ray Spectroscopy at SPring-8*, AIP Conf. Proc. **879**, 523 (2007).

[96] F. Z. Guo, T. Muro, T. Matsushita, T. Wakita, H. Ohashi, Y. Senba, T. Kinoshita, K. Kobayashi, Y. Saitoh, T. Koshikawa, T. Yasue, M. Oura, T. Takeuchi, and S. Shin, *Characterization of spectroscopic photoemission and low energy electron microscope using multipolarized soft x rays at BL17SU/SPring-8*, Rev. Sci. Instrum. **78**, 066107 (2007).

[97] C. Keutner, *Photoemissions-Elektronenmikroskopie an Magnetospirillum magnetotacticum* (Diploma thesis, Technische Universität Dortmund, 2011).

[98] R. Hönig, *Charakterisierung von Graphen auf 6H-SiC(0001) mittels PEEM und XPS* (Master's thesis, Technische Universität Dortmund, 2016).

[99] E. M. Purcell, *The Focusing of Charged Particles by a Spherical Condenser*, Phys. Rev. **54**, 818 (1938).

[100] J. Osterwalder, M. Sagurton, P. J. Orders, C. S. Fadley, B. D. Hermsmeier, and D. J. Friedman, *Electron trajectory analysis of the spherical-sector electrostatic spectrometer: focussing properties and multichannel detection capability*, J. Electron Spectros. Relat. Phenom. **48**, 55 (1989).

[101] M. Henzler and W. Göpel, *Oberflächenphysik des Festkörpers* (B. G. Teubner, Stuttgart, 1994).

[102] P. Espeter, *Structure determination of silicon nano-ribbons by means of photoelectron spectroscopy and photoelectron diffraction* (Ph.D. thesis, Technische Universität Dortmund, 2017).

[103] F. Schönbohm, *Temperaturverhalten und Strukturbestimmung dünner Metalloxidschichten auf Siliziumoberflächen* (Ph.D. thesis, Technische Universität Dortmund, 2013).

[104] T. Schmidt, S. Heun, J. Slezak, J. Diaz, K. C. Prince, G. Lilienkamp, and E. Bauer, *SPELEEM: Combining LEEM and Spectroscopic Imaging*, Surf. Rev. Lett. **5**, 1287 (1998).

[105] F. Guo, T. Wakita, H. Shimizu, T. Matsushita, T. Yasue, T. Koshikawa, E. Bauer, and K. Kobayashi, *Introduction of photoemission electron microscopes at SPring-8 for nanotechnology support*, J. Phys.: Condens. Matter **17**, S1363 (2005).

[106] M. Kotsugi and F. Z. Guo, *Introduction of SPELEEM at BL17SU/SPring-8* (Cheiron School, SPring-8, 2007).

[107] E. Bauer, *LEEM Basics*, Surf. Rev. Lett. **5**, 1275 (1998).

[108] A. Locatelli, T. O. Menteş, M. Á. Niño, and E. Bauer, *Image blur and energy broadening effects in XPEEM*, Ultramicroscopy **111**, 1447 (2011).

[109] A. P. Hitchcock, *Soft X-ray spectromicroscopy and ptychography*, J. Electron Spectros. Relat. Phenom. **200**, 49 (2015).

[110] H. Kromer, *Epitaktisches Wachstum von Graphen mittels der CCS-Methode* (Master's thesis, Technische Universität Dortmund, 2016).

[111] P. Vicente, E. Pernot, D. Chaussende, and J. Camassel, *Atomic-Step Observations on 6H- and 15R-SiC Polished Surfaces*, Mater. Sci. Forum **389**, 729 (2002).

[112] V. Borovikov and A. Zangwill, *Step bunching of vicinal 6H-SiC{0001} surfaces*, Phys. Rev. B **79**, 245413 (2009).

[113] K. Siegrist, E. D. Williams, and V. W. Ballarotto, *Characterizing topography-induced contrast in photoelectron emission microscopy*, J. Vac. Sci. Technol. A **21**, 1098 (2003).

[114] J. Pelletier, D. Gervais, and C. Pomot, *Application of wide-gap semiconductors to surface ionization: Work functions of AlN and SiC single crystals*, J. Appl. Phys. **55**, 994 (1984).

[115] M. Wiets, M. Weinelt, and Th. Fauster, *Electronic structure of SiC(0001) surfaces studied by two-photon photoemission*, Phys. Rev. B **68**, 125321 (2003).

[116] S. Mammadov, J. Ristein, J. Krone, C. Raidel, M. Wanke, V. Wiesmann, F. Speck, and Th. Seyller, *Work function of graphene multilayers on SiC(0001)*, 2D Mater. **4**, 015043 (2017).

[117] M. Hupalo, E. H. Conrad, and M. C. Tringides, *Growth mechanism for epitaxial graphene on vicinal* 6*H-SiC*(0001) *surfaces: A scanning tunneling microscopy study*, Phys. Rev. B **80**, 041401 (2009).

[118] S. Forti, K. V. Emtsev, C. Coletti, A. A. Zakharov, C. Riedl, and U. Starke, *Large-area homogeneous quasifree standing epitaxial graphene on SiC(0001): Electronic and structural characterization*, Phys. Rev. B **84**, 125449 (2011).

[119] K. Emtsev, *Electronic and structural characterizations of unreconstructed SiC{0001} surfaces and the growth of graphene overlayers* (Ph.D. thesis, Friedrich-Alexander-Universität Erlangen-Nürnberg, 2009).

[120] D. O. Campbell, *2-D electronic materials: epitaxial growth of graphene on 6H-silicon carbide (0001)* (Ph.D. thesis, Cornell University, 2015).

[121] C. Riedl, *Epitaxial Graphene on Silicon Carbide Surfaces: Growth, Characterization, Doping and Hydrogen Intercalation* (Ph.D. thesis, Friedrich-Alexander-Universität Erlangen-Nürnberg, 2010).

[122] W. Chen, H. Xu, L. Liu, X. Gao, D. Qi, G. Peng, S. C. Tan, Y. Feng, K. P. Loh, and A. T. S. Wee, *Atomic structure of the 6H–SiC(0001) nanomesh*, Surf. Sci. **596**, 176 (2005).

[123] C. Riedl, U. Starke, J. Bernhardt, M. Franke, and K. Heinz, *Structural properties of the graphene-SiC(0001) interface as a key for the preparation of homogeneous large-terrace graphene surfaces*, Phys. Rev. B **76**, 245406 (2007).

[124] K. Heinz, J. Bernhardt, J. Schardt, and U. Starke, *Functional surface reconstructions of hexagonal SiC*, J. Phys.: Condens. Matter **16**, S1705 (2004).

[125] F. Bozso, L. Muehlhoff, M. Trenary, W. J. Choyke, and J. T. Yates Jr., *Electron spectroscopy study of SiC*, J. Vac. Sci. Technol. A **2**, 1271 (1984).

[126] K. V. Emtsev, F. Speck, Th. Seyller, L. Ley, and J. D. Riley, *Interaction, growth, and ordering of epitaxial graphene on SiC{0001} surfaces: A comparative photoelectron spectroscopy study*, Phys. Rev. B **77**, 155303 (2008).

[127] NIST, *X-ray Photoelectron Spectroscopy Database* (National Institute of Standards and Technology, Gaithersburg MD).

[128] D. E. Eastman, *Photoelectric Work Functions of Transition, Rare-Earth, and Noble Metals*, Phys. Rev. B **2**, 1 (1970).

[129] T. Vaara, J. Vaari, and J. Lahtinen, *Adsorption of Potassium on Co(0001)*, Surf. Sci. **395**, 88 (1998).

[130] S. W. Poon, W. Chen, E. S. Tok, and A. T. S. Wee, *Probing epitaxial growth of graphene on silicon carbide by metal decoration*, Appl. Phys. Lett. **92**, 104102 (2008).

[131] W. Chen, K. P. Loh, H. Xu, and A. T. S. Wee, *Growth of monodispersed cobalt nanoparticles on 6H–SiC(0001) honeycomb template*, Appl. Phys. Lett. **84**, 281 (2004).

[132] W. Platow, D. K. Wood, K. M. Tracy, J. E. Burnette, R. J. Nemanich, and D. E. Sayers, *Formation of cobalt disilicide films on* $(\sqrt{3}\times\sqrt{3})6H-\mathrm{SiC}(0001)$, Phys. Rev. B **63**, 115312 (2001).

[133] C. A. Strydom and H. J. Strydom, *X-ray photoelectron spectroscopy studies of some cobalt(II) nitrate complexes*, Inorg. Chim. Acta **159**, 191 (1989).

[134] J. J. Yeh and I. Lindau, *Atomic subshell photoionization cross sections and asymmetry parameters:* $1 \leqslant Z \leqslant 103$, At. Data Nucl. Data Tables **32**, 1 (1985).

[135] J. C. Slonczewski and P. R. Weiss, *Band Structure of Graphite*, Phys. Rev. **109**, 272 (1958).

[136] T. Nishizawa and K. Ishida, *The Co (Cobalt) system*, Bull. Alloy Phase Diagr. **4**, 387 (1983).

[137] J. A. Thornton and D. W. Hoffman, *Stress-related effects in thin films*, Thin Solid Films **171**, 5 (1989).

[138] M. Kotsugi, T. Wakita, T. Taniuchi, K. Ono, M. Suzuki, N. Kawamura, M. Takagaki, M. Taniguchi, K. Kobayashi, M. Oshima, N. Ishimatsu, and H. Maruyama, *Local electronic structure analysis using a photoelectron emission microscope (PEEM) with hard X-ray*, e-J. Surf. Sci. Nanotechnol. **4**, 490 (2006).

[139] D. Pacilé, J. C. Meyer, A. F. Rodríguez, M. Papagno, C. Gómez-Navarro, R. S. Sundaram, M. Burghard, K. Kern, C. Carbone, and U. Kaiser, *Electronic properties and atomic structure of graphene oxide membranes*, Carbon **49**, 966 (2011).

[140] G. Cao, S. Weber, S. Martin, M. Anderson, K. Sridharan, and T. Allen, *Spectral emissivity measurements of candidate materials for very high temperature reactors*, Nuclear Engineering and Design **251**, 78 (2012), 5th International Topical Meeting on High Temperature Reactor Technology (HTR 2010).

[141] S. Yang and M. B. Knickelbein, *Photoionization studies of transition metal clusters: Ionization potentials for* Fe_n *and* Co_n, J. Chem. Phys. **93**, 1533 (1990).

[142] A. F. Guillermet, *Thermodynamic Analysis of the Co-C System*, Z. Metallkd. **78**, 700 (1987).

[143] M. V. Gomoyunova, G. S. Grebenyuk, and I. I. Pronin, *Binding Energies of Si 2p and Co 3p Electrons in Cobalt Silicides*, Tech. Phys. Lett. **37**, 1124 (2011).

[144] L. M. Porter, R. F. Davis, J. S. Bow, M. J. Kim, and R. W. Carpenter, *Chemistry, microstructure, and electrical properties at interfaces between thin films of cobalt and alpha (6H) silicon carbide (0001)*, J. Mater. Res. **10**, 26 (1995).

[145] S. W. Park, Y. I. Kim, J. S. Kwak, and H. K. Baik, *Investigation of Co/SiC interface reaction*, J. Electron. Mater. **26**, 172 (1997).

[146] Z. Wang, Q. Fu, and X. Bao, *Effect of Substrate Surface Reconstruction on Interaction with Adsorbates: Pt on 6H-SiC(0001)*, Langmuir **26**, 7227 (2010).

[147] F. Sette, G. K. Wertheim, Y. Ma, G. Meigs, S. Modesti, and C. T. Chen, *Lifetime and screening of the C 1s photoemission in graphite*, Phys. Rev. B **41**, 9766 (1990).

[148] K. Boller, R.-P. Haelbich, H. Hogrefe, W. Jark, and C. Kunz, *Investigation of carbon contamination of mirror surfaces exposed to synchrotron radiation*, Nucl. Instr. Meth. Phys. Res. **208**, 273 (1983).

[149] G. J. van Gurp and C. Langereis, *Cobalt silicide layers on Si. I. Structure and growth*, J. Appl. Phys. **46**, 4301 (1975).

[150] B. W. Lee, R. Alsenz, A. Ignatiev, and M. A. Van Hove, *Surface structures of the two allotropic phases of cobalt*, Phys. Rev. B **17**, 1510 (1978).

[151] C. V. Thompson, *Solid-State Dewetting of Thin Films*, Annu. Rev. Mater. Res. **42**, 399 (2012).

[152] M. G. Samant, J. Stöhr, H. R. Brown, T. P. Russell, J. M. Sands, and S. K. Kumar, *NEXAFS Studies on the Surface Orientation of Buffed Polyimides*, Macromolecules **29**, 8334 (1996).

[153] S. Anders, Th. Stammler, W. Fong, D. B. Bogy, C. S. Bhatia, and J. Stöhr, *Investigation of slider surfaces after wear using photoemission electron microscopy*, J. Vac. Sci. Technol. A **17**, 2731 (1999).

[154] S. Eisebitt, T. Böske, J.-E. Rubensson, J. Kojnok, W. Eberhardt, R. Jebasinski, S. Mantl, P. Skytt, J.-H. Guo, N. Wassdahl, J. Nordgren, and K. Holldack, *Electronic-structure determination of ion-beam-synthesized* $\mathrm{CoSi_2}$ *using photon-in–photon-out spectroscopies*, Phys. Rev. B **48**, 5042 (1993).

[155] S. J. Naftel and T. K. Sham, *Co $L_{3,2}$-edge and multi-detection channel XAFS studies of Co–Si interactions*, J. Synchrotron Radiat. **6**, 526 (1999).

[156] R. Madar, C. d'Anterroches, F. A. d'Avitaya, D. Boursier, O. Thomas, and J. P. Senateur, *Magnetic and transmission electron microscopy studies of the formation of cobalt silicide thin films*, J. Appl. Phys. **64**, 3014 (1988).

[157] K. Ishida, T. Nishizawa, and M. E. Schlesinger, *The Co-Si (Cobalt-Silicon) system*, J. Phase Equilib. **12**, 578 (1991).

[158] G. F. Zhou and H. Bakker, *Atomically disordered nanocrystalline Co_2Si by high-energy ball milling*, J. Phys.: Condens. Matter **6**, 4043 (1994).

[159] F. J. Himpsel, T. Jung, A. Kirakosian, J.-L. Lin, D. Y. Petrovykh, H. Rauscher, and J. Viernow, *Nanowires by Step Decoration*, MRS Bull. **24**, 20 (1999).

[160] L. Sun, Y. Hao, C.-L. Chien, and P. C. Searson, *Tuning the properties of magnetic nanowires*, IBM J. Res. Dev. **49**, 79 (2005).

[161] H. P. Oepen, M. Benning, H. Ibach, C. M. Schneider, and J. Kirschner, *Magnetic domain structure in ultrathin cobalt films*, J. Magn. Magn. Mater. **86**, L137 (1990).

[162] J. Unguris, M. R. Scheinfein, R. J. Celotta, and D. T. Pierce, *Magnetic microstructure of the (0001) surface of hcp cobalt*, Appl. Phys. Lett. **55**, 2553 (1989).

[163] D. M. Paige, B. Szpunar, and B. K. Tanner, *The magnetocrystalline anisotropy of cobalt*, J. Magn. Magn. Mater. **44**, 239 (1984).

[164] M. Kruskopf, D. M. Pakdehi, K. Pierz, S. Wundrack, R. Stosch, Th. Dziomba, M. Götz, J. Baringhaus, J. Aprojanz, Ch. Tegenkamp, J. Lidzba, Th. Seyller, F. Hohls, F. J. Ahlers, and H. W. Schumacher, *Comeback of epitaxial graphene for electronics: large-area growth of bilayer-free graphene on SiC*, 2D Mater. **3**, 041002 (2016).

[165] C. Xia, L. I. Johansson, Y. Niu, A. A. Zakharov, E. Janzén, and C. Virojanadara, *High thermal stability quasi-free-standing bilayer graphene formed on 4H–SiC(0 0 0 1) via platinum intercalation*, Carbon **79**, 631 (2014).

Publications

Articles

K. Shamout, P. Espeter, P. Roese, R. Hönig, U. Berges, and C. Westphal, *Revealing the interfaces of the hybrid system MgO/Co/GaAs(001): a structural and chemical investigation with XPS and XPD*, J. Phys.: Condens. Matter **30**, 075003 (2018).

P. Roese, K. Shamout, P. Espeter, R. Hönig, U. Berges, and C. Westphal, *Structure determination of substrate influenced silicon nano-ribbon growth*, Appl. Surf. Sci. **467–468**, 580 (2019).

R. Hönig, P. Roese, K. Shamout, T. Ohkochi, U. Berges, and C. Westphal, *Structural, chemical, and magnetic properties of cobalt intercalated graphene on silicon carbide*, Nanotechnology **30**, 025702 (2019).

Conference contributions

R. Hönig, C. Keutner, P. Espeter, P. Roese, C. Hilscher, U. Berges, and C. Westphal, *PEEM of epitaxial graphene on silicon carbide* (DPG Spring Meeting, Regensburg, 2016).

R. Hönig, P. Espeter, P. Roese, K. Shamout, H. Kromer, U. Berges, and C. Westphal, *Substrate topography and annealing of Co/Gr/SiC(0001) investigated by means of photoemission electron microscopy* (DPG Spring Meeting, Dresden, 2017).

R. Hönig, P. Espeter, P. Roese, K. Shamout, U. Berges, and C. Westphal, *Photoemission study of the intercalation of transition metals underneath graphene on silicon carbide* (DPG + EPS Spring Meeting, Berlin, 2018).

R. Hönig, P. Roese, K. Shamout, T. Ohkochi, U. Berges, and C. Westphal, *Imaging the Magnetic Domain Structure of Cobalt Intercalated underneath Graphene on Silicon Carbide* (Joint MMM-Intermag Conference, Washington DC, 2019).

Acknowledgments

I dedicate this last page to those people without whom this work would not have been possible.

First of all, I would like to express my gratitude to my doctoral adviser Prof. Dr. Carsten Westphal who gave me the opportunity to work in the fascinating field of surface physics. While he was always open for my questions, he granted great freedom in how to organize my project, which I highly appreciate. I would also like to thank Prof. Dr. Markus Betz for dedicating his time to be a second referee of my doctoral thesis.

I would like to thank Dr. Peter Roese and Dr. Karim Shamout for their support during the beamtimes at SPring-8 and DELTA. It is thanks to them that the beamtime also had a humorous side. Also, thanks go to Dr. Philipp Espeter for his support during the first measurements at DELTA. I thank Dr. Ulf Berges for providing his expertise in vacuum physics, which was invaluable for the numerous experimental construction works, and for his support during beamtime. Thanks also go to the DELTA staff for their continuous effort to ensure the operation of the DELTA storage ring.

A large part of this work would not have been possible without the help of Dr. Takuo Ohkochi during the PEEM measurements at SPring-8. His tireless dedication around the clock enabled the efficient use of the limited available beamtime. Also, I would like to thank Dr. Masaki Oura, for his support before and during the beamtime at SPring-8.

Many thanks go to all members of the group Experimentelle Physik Ib for the pleasant working atmosphere in the office and the laboratory. Especially, I want to mention Christopher Kohlmann and Robert Appel, with whom I shared an office in the past years and whose company I really appreciate. Special thanks go to Malte Schulte and Philipp Weinert for proofreading this thesis.

I would also like to thank my family and friends for enduring my moods in the past years and their continuous support, showing me that there is a world outside the university. Last but not least, I would like to thank Isabel for the wonderful time we have together and for her encouraging words in difficult times. Without her, I most probably would not have made it this far.